Ambient noise levels off the coast of Northern Labrador

by

Josiane Ostiguy

A thesis submitted to the School of Graduate Studies in partial fulfillment
of the requirements for the degree of

Master of Science

Department of Physics and Physical Oceanography

Memorial University of Newfoundland and Labrador

March 2022

Abstract

Ambient sound data was recorded over a 6 month period from October 2017 to March 2018 and a 15 month period from July 2019 to September 2020. This data was recorded from a mooring at the northeastern edge of Saglek Bank off Northern Labrador, where the water depth is 500 meters. High biodiversity and limited shipping activity make this an area of interest. At the mooring location, tidally driven currents are driven to speeds of up to 50 cm/s. The high current speeds result in a significant tilting of the mooring, with the instrument often indicating tilts in excess of 20 degrees. Further, the high speeds lead to mooring noise which corrupts the ambient sound data. We use current meter data to identify periods of reduced current speeds where sound data is not corrupted, thereby recovering a record of naturally occurring sounds. Tidal predictions are used to sort the acoustic data for periods where current speeds are unavailable. The reduced data set is used to explore noise levels in this area and obtain surface wind speed and rainfall rate estimates. A bottom interaction model is described and evaluated to asses the impact of bottom reflections on noise levels and to determine the effect on weather estimates. Within the quiet periods of the sound recordings, whale calls are heard. This thesis also reports on an application of the Phase and Amplitude Gradient Estimation (PAGE) method in an oceanographic context to estimate acoustic intensity. The PAGE method employs phase unwrapping such that the vector intensity is estimated past the Nyquist limit, and the direction of the acoustic source is determined with increased accuracy.

Acknowledgements

I would like to thank my supervisor, Dr. Len Zedel for his continuous support and guidance throughout the completion of this thesis. Dr. Len Zedel's knowledge and enthusiasm has been very beneficial to this work. I would also like to thank Dr. Bruce Martin and Jasco Applied Sciences for providing an internship opportunity as well as support during the completion of my project. Further, I am grateful to have had the opportunity to participate in leg 2 of the 2021 Amunsden expedition and for the work done by Amundsen Science regarding the deployment and retrieval of the moorings used for data collection. Lastly, I would like to thank Dr. James Munroe for assistance in obtaining model weather data for comparison with my results.

Contents

List of Figures

List of Tables

Chapter 1

Introduction

The study of ambient noise in the ocean has important applications. The ambient noise spectra are used to evaluate marine mammal presence, assess the impact of anthropogenic noise on marine life, and estimate surface wind speed and rainfall rate. Noise levels may be useful in situations where measurements are challenging. Due to spatial variability and surface wind waves, wind speed measurements from conventional weather buoys present some challenges. Similarly, as rainfall varies greatly in time and space, accurate measurements may be difficult to obtain. Thus, wind speed and rainfall rate estimates from underwater noise levels provide an effective alternative.

Ambient noise was studied on the Northeastern edge of Saglek bank in the Labrador Sea. Saglek bank is an area of high biodiversity and with limited shipping activity, making this an area of interest. Shipping noise is a frequent issue in the study of natural ambient noise though this is avoided at the Saglek bank location. However, high current speeds linked to the tidal cycle lead to complications with instrument mooring design as well as noise contamination. A sorting method based on current speeds is employed to reduce noise contamination such that naturally occurring noise levels are recovered. This sorting method is applied to current measurements and current predictions obtained through tidal harmonic analysis.

Additionally, a method for acoustic intensity estimation is applied and evaluated. Traditional finite difference techniques for acoustic intensity calculation are limited by the spatial Nyquist limit. Past the Nyquist limit, finite difference methods break down as the phase wraps and intensity estimates are not reliable. However, the Phase and Amplitude Gradient Estimation (PAGE) method allows this issue to be resolved. The PAGE method provides accurate vector intensity estimates past the Nyquist limit by focusing on the phase and pressure amplitude gradients as functions of frequency.

Chapter 2 presents background information relevant to the thesis work. Instrumentation details and techniques involved in data collection are discussed. In addition, a thorough literature review presents the various sources of ocean noise as well as sound transmission in the ocean.

Next, signal processing methods are described in chapter 3. Welch's method for power spectral density calculation is defined and tidal harmonic analysis is presented. Weather classification, wind speed and rainfall rate algorithms as well as a bottom interaction model are also introduced as they are applied in a later chapter.

Data acquisition is the topic of chapter 4. The area of interest is discussed and some instrumentation details are presented. Challenges with current measurements resulting from high current speeds are discussed and a solution to the issue is proposed.

In chapter 5, data analysis is performed. The methods presented in previous chapters are applied to the Saglek bank data sets for October 2017 to March 2018 and July 2019 to September 2020. Tidal harmonic analysis is used to estimate current speed when measurements are unavailable. Ambient noise recordings are then sorted according to current speed, such that noise contamination is eliminated and naturally occurring noise levels are recovered. Surface wind speed and rainfall rates are calculated for both time periods.

Chapter 6 discusses the results of this thesis work and provides some conclusions.

Lastly, appendix A presents the phase and amplitude gradient estimation (PAGE) method to estimate acoustic intensity. The PAGE method is introduced and the details of the method application in an oceanographic context are presented. The principal advantage of this method is phase unwrapping which allows for accurate acoustic intensity and direction estimates past the Nyquist limit.

Chapter 2

Background

2.1 Ambient noise sources

Ambient noise in the ocean is generated by a variety of sources such as wind and waves, rain, hail and other types of precipitation, sea ice, seismic events and biological sources. Shipping activity and other anthropogenic sources such as industrial activity and scientific data collection namely seismic surveys or sonar systems also contribute to ocean noise. The spectra of the various sources are shown in figure 2.1, as initially presented in [31]. The following sections will briefly discuss the main sources of ambient noise in the ocean.

2.1.1 Wind

In the absence of shipping activity or biological noise sources, ambient noise levels in the frequency band from 100 Hz to 25 kHz are dependent on the surface wind speed and sea state. Breaking waves, bubbles and spray resulting from surface agitation are dependent on wind [31]. Further, wind generated breaking waves are a dominant natural noise source from 1 to 50 kHz [4]. The presence of wind leads to surface agitation, which is also a significant noise source. Surface agitation is dependent on many factors, including wind duration and consistency, fetch, swell and current [31].

Wind dependent noise levels are highly dependent on bottom depth, where noise levels in shallow water tend to be greater than noise levels in deep water [31]. In addition, locally wind driven acoustic energy propagates at close to vertical angles [3].

Ocean ambient noise contains a wind-dependent high frequency component with a broad peak between
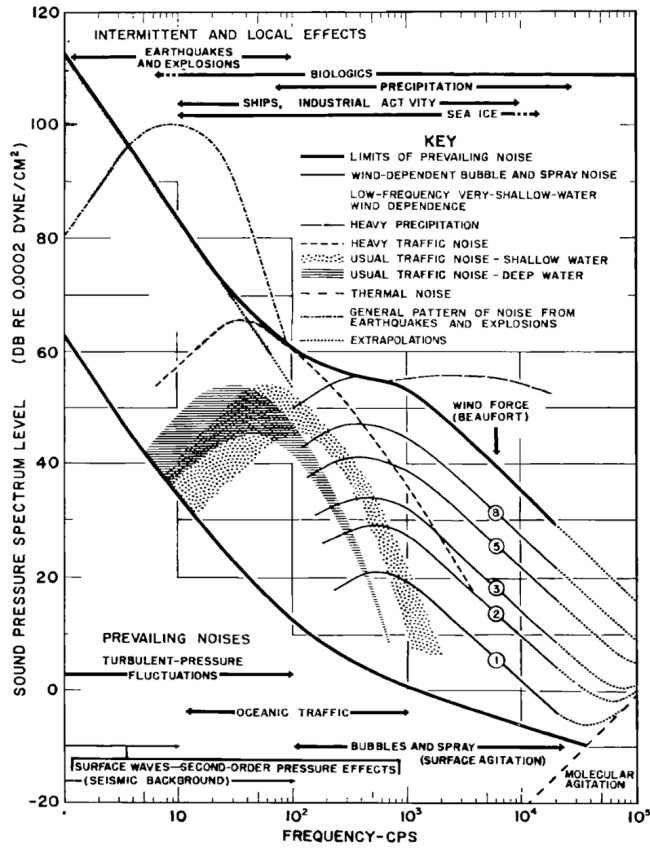
Figure 2.1: Ambient noise spectra for different sources. Horizontal lines indicate frequency bands [31].

100 Hz and 1 kHz, shown in figure 2.1. Past the peak, at frequencies between 1 and 100 kHz, a slope of approximately -6 dB per octave is observed and is independent of wind speed. Below 100 Hz, little to no wind dependence is observed, except in the case of very shallow water [31].

2.1.2 Rain

Sound is produced underwater by rain falling to the ocean's surface and by the splashes and bubbles generated by the rain drops. Rain is commonly categorized by rain drop diameter, D, measured in mm. The noise produced by both the impact and any resulting radiating bubbles, formed at the impact site, is highly dependent on the rain drop size. Five acoustically distinctive groups correspond to diameters of D < 0.8 mm, 0.8 < D < 1.1 mm, 1.1 < D < 2.2 mm and D > 2.2 mm also referred to as minuscule, small, mid-size and large, respectively. Small and large drops are the dominant sources of noise generated from rain, producing noise from impact and bubble formation [17]. Additionally, minuscule drops do not produce a significant

4

impact noise. They also find that mid-sized drops produce an impact noise but do not lead to bubble formation and conclude that this may be due to insufficient kinetic energy. Bubble formation is dependent on drop diameter as well as wind and surface slope. The presence of wind will affect the angle of incidence of the raindrops, significantly reducing the probability of bubble formation. A small root-mean-square surface slope has the same effect [17].

In addition to rain drop diameter, rain generated sound depends on the total rainfall rate (TRR). Total rainfall rate in units of mm/h is defined as,

$$TRR(mm/h) = 6 \times 10^{-4} \int_0^{5mm} \pi D^3 V_T n(D) dD \qquad (2.1)$$

where $n(D)dD$ is the number of drops per unit volume, V_T is the terminal speed and $\pi D^3/6$ is the water volume per drop. It is then possible to define thresholds for light rain, TRR < 2.5 mm/h, moderate rain, 2.5 < TRR < 7.6 mm/h and heavy rain, TRR > 7.6 mm/h [22].

In drizzle conditions where TRR ≈ 1.1 mm/hr where only light winds are present, the sea state is calm and small drops are dominant, the spectral peak is attributed to exponentially decaying oscillating bubbles. Bubbles will oscillate as a result of the pressure difference between the air inside the bubble and the surrounding water. The frequency of oscillation is defined in the following section. As wind increases, the spectral peak broadens and shifts to higher a frequency [16].

In light rain (small drop) conditions, a peak at 15 kHz is observed. This peak is broad, wind sensitive, poorly correlated with TRR [22] and dependent on raindrop impact velocity. As seen for drizzle conditions, the spectral peak will shift to a higher frequency and broaden in the presence of wind and surface waves [21].

The noise generated by heavy rain, associated with large drops, differs significantly from that generated by light rain. Although small drops may be present during heavy rain, the 15 kHz peak is absent in these conditions. Sound levels produced by heavy rainfall increase with rainfall rate for frequencies and wind speeds up to 10 kHz and 15 m/s, respectively [22]. The high correlation between rainfall rate and sound level allows for an algorithm to estimate rainfall rate from underwater sound to be developed [22].

2.1.3 Bubbles

Bubbles are mainly generated by breaking waves, surface agitation and rain drops impacting the ocean surface. However, even when there is little wind-generated surface agitation, bubble noise may still be an important contribution to overall ocean noise [31]. The bubbles will oscillate and produce noise. For the

zeroth or "breathing mode", bubble oscillation occurs at frequency,

$$f_0 = \frac{1}{2\pi R_0} \sqrt{\frac{3\gamma p}{\rho}} \tag{2.2}$$

where the ratio of specific heats for the gas in the bubble is γ, the ambient pressure is p, the density of the surrounding liquid is ρ and the average radius of the bubble is R_0. The sound pressure amplitude of the oscillating bubble is directly proportional to the oscillation amplitude.

As well as acting as sources of sound, bubbles near the ocean surface can significantly influence sound propagation near the surface. During wind speeds of 8m/s the attenuation near the surface can be near 60 dB/m and the speed of sound may be reduced by order 10m/s [16]. Therefore, wind dependent noise at depth is often affected by the presence of bubbles. Noise levels at higher frequencies, typically above 20 kHz, tend to be masked by bubble layers near the surface [4]. Below 200 Hz, bubbles have been found to amplify the pressure oscillations caused by turbulence and at higher frequencies in the kHz range, single bubble oscillations can be important contributions to observed noise levels [25].

2.1.4 Marine organisms

Marine organisms contribute to ocean noise with both intentional and unintentional sounds. Intentional sounds include dolphin clicks, whale calls, and various fish vocalizations and are generally used for communication, hunting, or gathering information about the surrounding environment. Unintentional sources include the sound produced by the air released during fish buoyancy correction or by large schools of fish. These biological sounds are often time dependent and can be diurnal or seasonal [19]. Noise of biological origin typically is short in duration but is frequently repeated [31].

Fish produce a variety of different sounds for communication or as a result of swimming and feeding. The source of noise is often related to the swim bladder and the noise itself is emitted as a pulse of sound with a peak energy of less than 1 kHz. Seasonal chorusing behaviour is also an important source between approximately 50 Hz and 5 kHz and can raise the noise level by more than 20 dB. Although noise contributions from fish have been studied in local areas, the general effect on ocean ambient noise has rarely been assessed. Some invertebrates, notably snapping shrimp, also produce sound though they are not often considered dominant contributors to the overall ambient sound [31].

Vocalizations by marine mammals range from less than 10 Hz to more than 200 kHz and vary by species. Mysticetes (baleen whales) generally produce lower frequency noise than Odontocetes (dolphins and toothed

whales). Mysticetes produce a variety of sounds such as low frequency moans, simple narrowband calls and complex broadband calls. The moans have peak frequencies below 200 Hz, whereas the narrowband calls are closer to 1 kHz. The complex calls are typically amplitude or frequency modulated pulses. Odontocetes produce constant frequency or frequency modulated whistles as well as broadband clicks which have peak frequencies that range from 1 to 200 kHz and 1 to 25 kHz, respectively [19]. Source levels of the sounds produced by marine mammals vary by type. High source levels tend to be from echolocation clicks and can reach levels of around 230 dB re 1 μPa at 1 m. Low-frequency communication whistles have lower source levels, generally below approximately 190 dB re 1 μPa at 1 m. The contribution of marine mammal vocalizations to the ambient sound tends to be local in space, an exception being the low frequency calls made by baleen whales [19].

The characterization of noise produced by marine organisms is important in order to identify similarities and differences with anthropogenic noise sources. It is then possible to study the effects of anthropogenic noise sources on biological ocean ambient noise.

2.1.5   Shipping activity

An increase in global commercial shipping, as well as ship size and propulsion power, has led to an increase in overall shipping noise [15]. Shipping activity is a dominant source of noise at low frequencies between around 10 and 500 Hz [31]. A broad peak in the noise levels is present between 10 Hz and 200 Hz is attributed to shipping activity and distant traffic noise is an important contributor in this frequency range [31]. Past the peak frequency in its spectrum, a steep negative slope is seen. The main source of low frequency noise generated by ships is a result of propeller cavitation. Broadband noise produced by propeller cavitation and flow over the hull increases with ship speed [19].

The total contribution of shipping activity to the ambient noise is highly dependent on sound propagation characteristics, bathymetry as well as ship distribution and quantity [31][15]. Noise from individual ships at close range includes narrowband components with peak frequencies at less than 1 kHz in addition to the broadband cavitation component [31].

2.1.6   Seismic sources

Noise from seismic sources depends on the magnitude and location of the seismic activity as well as the propagation path. Peak frequencies range from approximately 1 to 100 Hz depending on conditions. This type of noise is infrequent and of relatively short duration [31]. Volcanic and hydrothermal activity or moving

sediment on the ocean floor are also local sources that may contribute to the overall ocean noise.

2.1.7   Depth dependence

Most sources of deep ocean noise originate at the ocean surface with noise levels that vary with depth. Noise produced by a given wind speed will be approximately 5 dB higher in shallow water than in deep water for the same frequency [31]. The spectrum slope has also been seen to increase with depth [24]. In addition, in the frequency band from 1 to 10 kHz, noise is downward traveling and bottom reflections do not make an important contribution to noise levels in deep water [3]. Barclay and Buckingham [3] note that this result is expected from sources at the ocean surface.

For a surface source where noise travels in a vertical direction, measurements of noise level as a function of depth up to approximately 4500 m have shown that noise levels tend to decrease with increasing depth for frequencies above 177 Hz [24]. Similarly, a decrease in noise levels below 100 Hz with increasing depth in measurements made up to near 4400 m [18]. Observations have also led to the conclusion that the correlation between noise spectrum levels and wind speed is independent of depth [24]. However, wind speed effects tend to increase with frequency [18]. It has also been observed that above 200 Hz and in high wind speed conditions, there is little change in noise level with depth [18].

2.1.8   Other sources

Other noise sources worth briefly mentioning include seismic surveys, sonars, explosions, industrial activity and ice. Industrial activity may be an important source in coastal areas or in the case of oil drilling. Noise generated by ice depends mainly on the type of ice and temperature. Sound is produced from rigid ice cracking (thermal or mechanical stress induced) and moving ice packs. Lastly, pressure fluctuations (i.e., thermal noise) are the dominant natural noise source above 100 kHz [31].

Turbulence in the ocean may occur as a result of advection, convection, density currents, the interaction of water masses as well as at the ocean surface or bottom boundaries. Turbulence may also be created as the transducer itself interacts with the surrounding water motion. This may lead to noise and is not considered a source of ambient noise [31]. Further, the transducer will record any pressure fluctuations in the ocean even if they are not associated with radiating noise. Thus, if the transducer is in a turbulent region the pressure fluctuations of the turbulence itself will be recorded [31]. These fluctuations are much larger in magnitude than those from any resulting noise. However, in the case of ocean turbulence, peak levels occur around 1 to 10 Hz [31] and notably outside the band of interest of the present study. Any pressure fluctuations

radiated from turbulence are small compared to ambient noise levels even in highly turbulent areas such as a turbulent jet [31].

2.2 Sound transmission

Sound propagation in the ocean is affected by spreading loss, transmission loss and attenuation. The SONAR equation (equation 2.3) relates sound pressure level (SPL) to transmission loss (TL) and source level (SL).

$$SPL = SL - TL \quad (dB) \tag{2.3}$$

SPL, TL and SL are defined below in dB as equations 2.4, 2.5 and 2.6, respectively.

$$SPL = 20 \log \frac{P}{P_{ref}} \quad (dB) \tag{2.4}$$

$$TL = -20 \log |[trans(r, f)] \quad (dB) \tag{2.5}$$

$$SL = 20 \log \frac{P_0}{P_{ref}} \quad (dB) \tag{2.6}$$

where P_0 is the source pressure, P is the root mean square sound pressure and P_{ref} is a reference pressure, typically 1 μPa in oceanographic applications. The transmission factor term in equation 2.5 accounts for the complexity of sound propagation underwater. This term depends on bathymetry, sound speed profiles, multipath arrivals, range, source frequency, caustics, absorption, scattering and the type of divergence from the source to the receiver [16].

Further, attenuation losses occur as the signal is traveling. Losses from absorption depend on viscosity and molecular relaxation of boric acid and magnesium sulfate. Equation 2.7 defines the total absorption coefficient, α, in dB/km [10].

$$\alpha = \frac{A_1 P_1 f_1 f^2}{f^2 + f_1^2} + \frac{A_2 P_2 f_2 f^2}{f^2 + f_2^2} + A_3 P_3 f^2 \quad (dB/km) \tag{2.7}$$

where subscipts 1, 2 and 3 denote boric acid, magnesium sulfate and pure water, respectively. Additionally, f_1 and f_2 are relaxation frequencies, P are pressure terms and A are terms dependent on depth, temperature, salinity, pH and sound speed. The absorption coefficient, α, therefore increases with frequency. For reference, coefficient values can be found in [10].

2.3 Acoustic measurements

2.3.1 Acoustic Doppler current profiler

Acoustic Doppler current profilers (ADCPs) are an important instrument in the field of acoustical oceanography. They are a frequently used instrument to make current velocity measurements. ADCPs measure current velocities using the principles of the Doppler effect. The Doppler shift is defined as the frequency shift between an immobile source and a moving receiver or an immobile receiver and a moving source. The Doppler shifted frequency is then,

$$f_t - f_r = \Delta f = \frac{(v_r - v_t) \cdot \hat{k}}{c} f_t \tag{2.8}$$

where $\hat{k}$ is the direction of sound propagation, f_t and f_r are the transmitted and received frequencies, v_t and v_r are the transmitted and received vector velocities for either an immobile source or receiver. One can see that if the receiver and the source are moving towards each other the frequency shift will be negative, resulting in a red shift. The reverse will results in a blue-shift. In equation 2.8 the sound speed is assumed to be uniform and the displacement between the source and receiver is assumed to be small.

ADCPs typically consist of 3 or 4 transducers that emit sound pulses at a 20° to 30° angle from the vertical. ADCPs transmit sound pulses at a fixed frequency that reach sound scatterers present in the ocean. Small particles floating in the water column and plankton may act as scatterers. The scatterers float in the water and on average, move at the same horizontal velocity as the surrounding water. Once the sound pulse reaches a scatterer, scattering occurs, and some sound will be reflected back to the transducer. The reflected sound will be Doppler shifted according to the velocity of the scatterer, thereby allowing a measurement of the water velocity. The scatterer will behave as a source at frequency f_r such that the Doppler shifted frequency becomes,

$$\Delta f = \frac{2(v_r - v_t) \cdot \hat{k}}{c} f_t. \tag{2.9}$$

Using the principles outlined above, the ADCP will measure the velocity component parallel to each acoustic beam. Thus, using 3 or 4 acoustic beams a measurement of the velocity in 3-dimensions is made. The ADCP beams may be used to measure current velocity profiles. The measured velocity is divided into depth cells along the acoustic beam. Panel A of figure 2.2 shows this for an upward looking ADCP. In the event of high current speeds, it is possible for the ADCP to tilt, as in panel B of figure 2.2. In this case, depth cells must be mapped such that cells at the same depth are paired up for velocity calculations. Depth cell mapping allows the current velocity with depth to be measured when the ADCP is tilted.
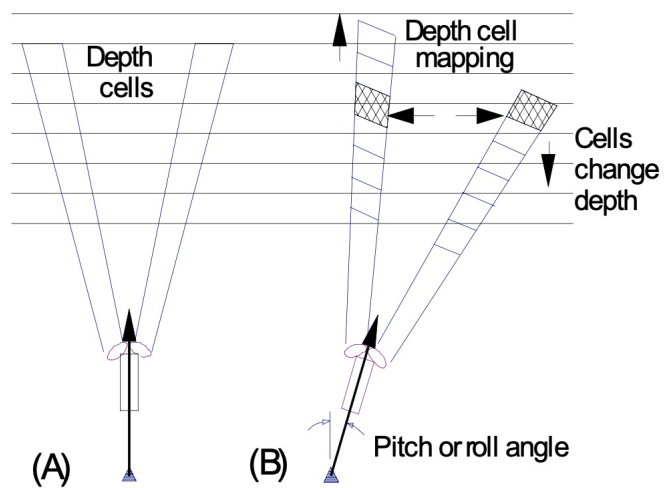
Figure 2.2: ADCP depth cells (A) and tilted ADCP with depth cell mapping (B) [27].

2.3.2 Hydrophone measurements

Hydrophones are used in water to make acoustic observations. They contain a piezoelectric sensor that detects pressure changes as sound waves are received. The pressure changes lead to voltage generation which induces an electrical current and the voltage is recorded. The sensitivity of a hydrophone is a measure of this process and is generally given in units of dB re 1 V/μPa. The sensitivity of the hydrophone used here is shown in figure 2.3 as a function of frequency. The hydrophone sensitivity curve is used to convert the measured signal into pressure units of μPa for further analysis.
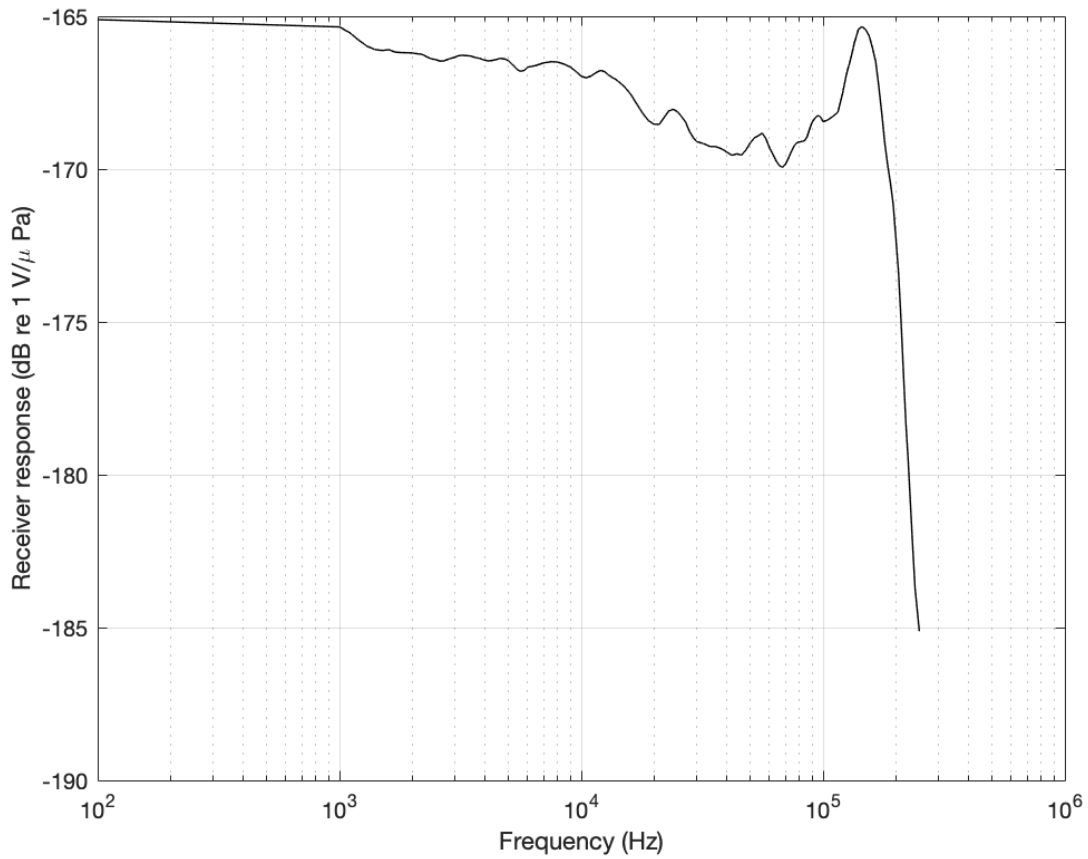
Figure 2.3: Hydrophone M36-V35-100 sensitivity as a function of frequency.

Chapter 3

Signal processing methods

In the following chapter, different signal processing methods are described. First, spectral analysis is presented. Spectral analysis involves the frequency spectrum of signals. The power spectral density (PSD) of a signal and the Welch method, used to estimate the PSD, are both defined. In the case of tidal signals, it is possible to employ spectral analysis however, it is preferable to use a method which takes advantage of the known tidal frequencies. Tidal analysis is needed to evaluate the tidal constituents present in a signal and to estimate future tidal current velocities. An overview of tidal analysis and a function which performs this analysis is also outlined below.

3.1   Power spectral density

When considering signals, it is often useful to identify the distribution of signal energy as a function of frequency. This function is known as the power spectral density of the given signal. We can arrive at such a representation by using the Fourier transform,

$$\hat{x}(f) = \int_{-\infty}^{\infty} e^{-i2\pi ft} x(t) dt \tag{3.1}$$

for a time series $x(t)$. For a continuous deterministic signal, the total energy of the signal is finite and we have,

$$E = \int_{-\infty}^{\infty} |x(t)|^2 dt < \infty \tag{3.2}$$

such that the Fourier transform exists. The energy spectral density (ESD) is then defined as,

$$S_E(f) = |\hat{x}(f)|^2. \tag{3.3}$$

Equation 3.3 defines an energy density which is confirmed by Parseval's theorem. The energy of the signal in the time domain is equal to the energy in the frequency domain, as stated by equation 3.4

$$\int_{-\infty}^{\infty} |x(t)|^2 dt = \int_{-\infty}^{\infty} |\hat{x}(f)|^2 df \tag{3.4}$$

If the signal is stationary and random, the total energy is unbounded and its Fourier transform does not exist. Therefore, the power spectral density (PSD) must be defined. The PSD of a signal represents the power present in the signal as a function of frequency. The ESD of a signal forms a Fourier transform pair with the signal's autocorrelation function which is defined as the correlation of a signal with a delayed duplicate of itself. The autocorrelation is thus used to define the PSD and is written as,

$$R_{xx}(\tau) = E[x(t)x(t+\tau)] \tag{3.5}$$

for a give time interval, τ. The PSD then becomes,

$$S_{xx}(f) = \int_{-\infty}^{\infty} R_{xx}(\tau) e^{-i2\pi f \tau} d\tau, \tag{3.6}$$

obtained using the Wiener-Khinchin relation.

3.1.1 Welch method

The Welch method is a method used to estimate the PSD of a signal. The PSD for a signal $x(t)$ is defined in terms of the discrete Fourier transform (DFT). The DFT differs from equation 3.1, the integral form of the Fourier transform, in that it is used for discrete signals. The PSD is written as,

$$S_{xx}(f) = \frac{1}{N\Delta t} \left| \Delta t \sum_{n=0}^{N} x_n e^{-i2\pi f n \Delta t} \right|^2 = \frac{1}{N\Delta t} |\hat{x}(f)|^2 \tag{3.7}$$

14

where N is the number of samples. The PSD is estimated by the Welch method using overlapping windowed data segments to compute the periodogram. The jth data segment of signal $x(t)$ is,

$$x_j(t) = x((j-1)K + t) \tag{3.8}$$

for $t = 1, ..., M$ and $j = 1, ..., S$ where the starting point of the segment is $(j-1)K$. $K = M/2$ is commonly used and corresponds to 50% overlap between the segments. The sequences do not overlap when $K = M$. The windowed periodogram $\phi_j(w)$ and the power P of the window function $w(t)$ are defined as,

$$\phi_j(\omega) = \frac{1}{MP} \left| \sum_{t=1}^{M} w(t) x_j(t) e^{-i\omega t} \right| \tag{3.9}$$

$$P = \frac{1}{M} \sum_{t=1}^{M} |w(t)|^2 \tag{3.10}$$

The windowed periodograms are then averaged to estimate the PSD.

$$\phi_W(\omega) = \frac{1}{S} \sum_{j=1}^{S} \phi_j(\omega) \tag{3.11}$$

Equation 3.11 is called the Welch estimate of the PSD. The Welch method attempts to reduce the variance of the estimated PSD by assuming the signal content does not change between intervals and thus, averaging the window estimates.

3.2 Tidal analysis

Tides are generated by differential gravity caused by forces between the earth, sun and moon. In oceanic time series, tidal variations are often dominant signals, especially in coastal areas. When strong tidal signals are present, they are seen as sharp spectral peaks at diurnal and semi-diurnal frequencies. Spectral analysis can be applied to tidal signals. However, as the exact frequencies associated with tidal forcing are known prior to the analysis it is preferable to use a method where the knowledge of the frequencies is beneficial. Tidal forcing can be modeled according to fundamental frequencies. These frequencies arise from the Earth's rotation on its axis and around the sun and the rotation of the moon around the earth. Cycles of 24.8 hours, 355.24 days and 27 days are associated with these rotations. Some important tidal constituents include the principal lunar M_2 of 12.42 hours, the principal solar S_2 of 12.00 hours as well as K_1, the luni-solar diurnal

constituent. The effects of the periodicity of the lunar perigee, orbital tilt and perihelion are also encapsulated in the characteristic frequencies. In the past, filtering methods have been used to isolate or remove tidal signals. Some issues arise with these methods and thus, harmonic analysis is now more commonly applied. The method of tidal harmonic analysis can be applied to water levels and currents [12]. The east and north components u and v can be written as harmonic functions,

$$u(t) = u_0 + \sum_{k=1}^{R} u_k \cos(\sigma_k t - b_k) + n_x(t) \tag{3.12}$$

$$v(t) = v_0 + \sum_{k=1}^{R} v_k \cos(\sigma_k t - c_k) + n_y(t) \tag{3.13}$$

where $n(x)$ represents the noise in the current signal. The spectral representation of $\{W(t)\} = \{u(t), v(t)\}$ is then,

$$W(t) = \sum_{k=-R}^{R} w_k \exp(i\sigma_k t) + n(t) \tag{3.14}$$

$$= \sum_{k=0}^{R} \{M_k \cos(\sigma_k t - g_k) + i m_k \sin(\sigma_k t - g_k)\} \exp(i\theta_k) + n(t) \tag{3.15}$$

where the index represents the kth component, σ is the frequency and g_k is the Greenwhich phase. The current velocity vectors trace out ellipses described by the semi-major axis $M_k = |w_k| + |w_{-k}|$ and the semi-minor axis $m_k = |w_k| - |w_{-k}|$, the orientation of the major axis θ_k and the phase component of the ellipse g_k. The terms w_k and w_{-k} are defined as,

$$w_k = |w_k| \exp(i a_k) \tag{3.16}$$

$$= \frac{1}{2}(u_k \exp(-i b_k) + i v_k \exp(-i c_k)) \tag{3.17}$$

$$w_{-k} = |w_{-k}| \exp(i a_{-k}) \tag{3.18}$$

$$= \frac{1}{2}(u_k \exp(i b_k) + i v_k \exp(i c_k)) \tag{3.19}$$

where we have $\sigma_{-k} = -\sigma_k$. The amplitude of the kth component a_k is split up into the east and north amplitudes as b_k and c_k. Decomposition into orthogonal modes may be used in order to analyze all data simultaneously rather than applying the analysis to point measurements [12]. Harmonic analysis can be used to extract the tidal component of a signal and in turn, it may be used for tidal predictions.

16

3.2.1   t-tide model

A program titled *t-tide* to perform classical tidal harmonic analysis with the use of complex algebra was developed [23]. They model the tidal response for N constituents as,

$$x(t) = b_0 + b_1 t + \sum_{k=1,...,N} a_k e^{i\sigma_k t} + a_{-k} e^{-i\sigma_k t} \tag{3.20}$$

where the first two terms account for an offset and a linear drift, a_k is the complex amplitude and σ_k is the frequency. The tidal components are chosen from 45 astronomical and 101 shallow water components. A least squares fit is performed and the coefficients are chosen such that equation 3.21 is minimized.

$$E = \sum_m |x(t_m) - y(t_m)|^2 = \|Ta - y\|^2 \tag{3.21}$$

T represents the linear and sinusoidal basis functions evaluated at times t, $a = [b_0, b_1, a_1, a_{-1}, ..., a_{-N}]'$ and $y = [y(t_1), ..., y(t_m)]'$. Nodal and phase corrections may be applied and are needed to correct for small satellites whose frequencies are very similar in value to the main tidal components. Slow variations of the main tidal components are known as nodal modulations and may be corrected with the proposed nodal and phase corrections. Nodal corrections for a given latitude are calculated as,

$$\hat{a}_k e^{i\sigma_k t} = f_k a_k e^{i\sigma_k t + iu_k} = a_k e^{i\sigma_k t} + \sum_j a_{kj} e^{i\sigma_{kj} t} \tag{3.22}$$

$$f_k e^{iu_k} = 1 + \sum_j \frac{a_{kj}}{a_k} e^{i(\sigma_{kj} - \sigma_k)t} \approx 1 + \sum_j \frac{a_{kj}}{a_k} \tag{3.23}$$

where kj are satellite indices, f_k and u_k are the amplitude and phase nodal corrections. Equation 3.23 is obtained by cancelling common terms on equation 3.22. The fit of the tidal response is then adjusted by factors f_k and u_k such that any variations due to satellites are accounted for.

The tidal analysis yields the following parameters:

$$L_k = |a_k| + |a_{-k}| \tag{3.24}$$

$$l_k = |a_k| - |a_{-k}| \tag{3.25}$$

$$\theta_k = \frac{ang(a_k) + ang(a - -k)}{2} \text{mod} 180 \tag{3.26}$$

$$g_k = v_k = ang(a_k) + \theta_k \tag{3.27}$$

where L_k and l_k are the semi-major and semi-minor axes, respectively, θ_k is the orientation of the semi-major axis and g_k is the Greenwich phase i.e. the phase referenced to the phase of the equilibrium response at 0 degrees longitude. If the time series is scalar then $l_k = 0$ and $\theta_k = 0$ where the ellipse becomes a line along the positive axis. The sign of l_k determines whether the ellipse is drawn in a clockwise or counter-clockwise direction [23].

3.3 Algorithms to estimate weather from ambient noise

3.3.1 Wind speed algorithm

An algorithm to determine surface wind speeds from underwater noise has been developed by Vagle, Large and Farmer [30]. The Weather Observations Through Ambient Noise (WOTAN) wind speed algorithm relates sound pressure variations to wind dependent variables. Wind speed and ocean noise were measured between 3 and 25 kHz during the Frontal Air-Sea Interaction Experiment (FASINEX) in the North Atlantic Ocean. These measurements are used to derive the wind speed algorithm. Additionally, the algorithm was tested with independent data from 4 locations in order to verify the final equations and ensure their generality.

Many variables affect sound propagation from a source at the surface. These include directionality of the source, spreading losses, reflection, spreading, attenuation and refraction and multipath propagation. Thus, consideration of these variables is made in the development of the wind speed algorithm. Sound pressure level (SPL) data is standardized such that ambient sound is converted to a non-dimensional sound spectrum level at 1 m depth, ensuring that data from different locations are comparable. In addition, the measured spectra are sorted such that contamination by ships, precipitation, or bubbles is removed and wind only spectra are obtained. The following equations are used to determine if precipitation is present.

$$\Delta SPL(19.5 - 3.0) > (Q + 2)\log(19.5/3.0) \tag{3.28}$$

$$\Delta SPL(12.5 - 3.0) > -10.54 \text{ dB} \tag{3.29}$$

$$\Delta SPL(8.0 - 3.0) > (Q + 3)\log(8.0/3.0) \tag{3.30}$$

where Q is the slope (dB/decade) of the wind only spectra as a function of frequency. When these conditions

are met, a precipitation flag is set. Similarly, contamination by shipping noise is likely present when,

$$\Delta SPL(6.5 - 3.0) < (Q - 3)\log(6.5/3.0) \tag{3.31}$$

$$\Delta SPL(8.0 - 3.0) < -9.37 \text{ dB} \tag{3.32}$$

The wind speed algorithm is derived to determine several wind variables. These are the friction velocity, u_* and wind stress, τ as well as U3, U10 and U_N10 corresponding to wind speed at 3 m, 10 m and 10 m with stability correction, respectively. The algorithm begins with the calculation of the SPL at a reference frequency as,

$$SPL_0 = SPL(f) + Q\log(f/f_0) + \beta(f) \tag{3.33}$$

where Q is the slope of the wind only spectra, f_0 is the reference frequency of 8 kHz and $\beta(f)$ is a correction factor. The correction factor is a function of depth and frequency and is determined according to the sound speed profile as,

$$\beta(h, f) = -10\log\left(2\int_0^\infty \left[\frac{r\ sin^2\theta \exp(-\alpha l)}{l^2}\right] dr\right) \tag{3.34}$$

where θ is the angle between the surface and the path to 1 m depth, l is the path length and α is the attenuation factor. Using the calculated SPL_0 values the pressure fluctuations are then,

$$p_0 = 10^{(SPL_0/20)} \tag{3.35}$$

The wind speeds U3, U10 and U_N10 are defined by,

$$V = (p_0 - b)/s \tag{3.36}$$

where p_0 are the pressure fluctuations and V corresponds to the wind speed variables. Empirically derived constants b and s were determined from linear fits between the SPL and the logarithm of the wind speed at 10 m height, calculated at the reference frequency f_0. Therefore, the final wind speed equation for a height of 10 m is as follows,

$$U_{10} = \frac{10^{SPL_{8kHz}/20} + 104.5}{53.91} \tag{3.37}$$

A minimum of three hour averages of the SPL are needed in order to get reliable wind speed estimates [30]. The average length requirement is attributed to the changing wave conditions at the surface which

results in a lag between the wind speed and the measured ambient sound. In addition, the algorithm does not work in shallow waters due to bottom effects or close to shore because of other noise sources, such as industrial noise in coastal areas. Further, attenuation due to bubbles at high frequencies from high wind speeds may be present in the observed spectra. This becomes important at high wind speeds and thus, the algorithm may be less accurate in such instances.

3.3.2 Rainfall rate algorithm

Measurement of rainfall over the ocean is often challenging and thus, estimating rainfall over the ocean using ambient noise provides an alternative. Rainfall measurements are difficult in part due to rainfall rates varying greatly in time and space. Also, satellite resolution for rainfall measurements is low, typically less than 10 satellite passes per day. A method for rainfall measurement at sea using ambient noise has been previously presented [5]. The wind speed algorithm presented above is used in order to calibrate the hydrophone. Rainfall signals from 1 to 10 kHz are composed mainly of 2-3.5 mm drops that are strongly correlated with rainfall rate [4]. The sound intensity produced at a rainfall rate of R is,

$$I = aR^b \tag{3.38}$$

where R is measured in mm/h. The logarithm is taken of equation 3.38 to obtain an equation of the form,

$$\text{dBR}/10 = (SPL_{5kHz} - a')/b' \tag{3.39}$$

where a' corresponds to the intercept, b' to the slope of the linear fit of rainfall rate versus SPL_{5kHz} data and $dBR = 10\log_{10}(R)$. An empirical derivation led to equation 3.40, relating the rainfall rate and sound pressure level [5].

$$\text{dBR}/10 = (SPL_{5kHz} - 42.4)/15.4 \tag{3.40}$$

Equation 3.40 was validated using independent data and good agreement was observed [5]. Additionally, the rainfall rate is related to the spectrum of the noise level as,

$$\text{slope}_{rain} = 8.33 \times \log(R) - 14.3 \tag{3.41}$$

20

where slope$_{rain}$ is the spectrum slope for a given rainfall rate [4]. Equation 3.41 is used to determine the expected noise at rainfall rate R. Since the accuracy of the estimated rainfall rate depends on the SPL measurement, a calibration method is recommended. The calibration method uses wind speed data and provides a frequency dependent sensitivity correction for the instrument. The acoustic signal from rain is wind dependent and at low frequencies, noise is often contaminated by breaking waves [5]. However, this effect is frequency dependent and can be removed. Above 30 kHz, sound level during periods with high rainfall rate decreases with increasing wind speed. Lastly, they determined that the peak near 15-25 kHz, associated with light rainfall, is highly affected by wind and is not a reliable signal for rainfall rate calculations. However, this signal can be used to detect rainfall.

3.3.3 Weather classification

An algorithm for weather classification of acoustic data exists [20]. The algorithm includes steps to detect noise produced by shipping, heavy rain, drizzle and bubbles. For completeness, the rainfall algorithm in section 3.3.2 and the wind speed algorithm in section 3.3.1 are included as part of this algorithm. The algorithm is divided into steps; the first is to check for excess low frequency noise associated with shipping traffic. Equation 3.42 determines if excess low frequency noise is present compared to high frequency noise, indicating the presence of shipping noise [20].

$$SPL_{20kHz} < 0.7 \cdot SPL_{4kHz} + 2$$

$$\text{and} \tag{3.42}$$

$$SPL_{20kHz} < -0.7 \cdot SPL_{4kHz} + 86$$

An example of how this test operates is shown in figure 3.1. Step 2 searches for high frequency noise that is associated with heavy rain using equation 3.43. Sound levels at 20 kHz are compared to levels at 5 kHz. The 52 dB threshold is included as the rainfall algorithm presented above is defined for levels above this value. If ambient bubbles are present then equation 3.44 is used [20]. Figure 3.2 presents an example of this test in use.

$$SPL_{20kHz} > 0.5 \cdot SPL_{5kHz} + 19 \quad \text{or} \quad SPL_{20kHz} > 47.5$$

$$\text{and} \tag{3.43}$$

$$SPL_{5kHz} > 52$$
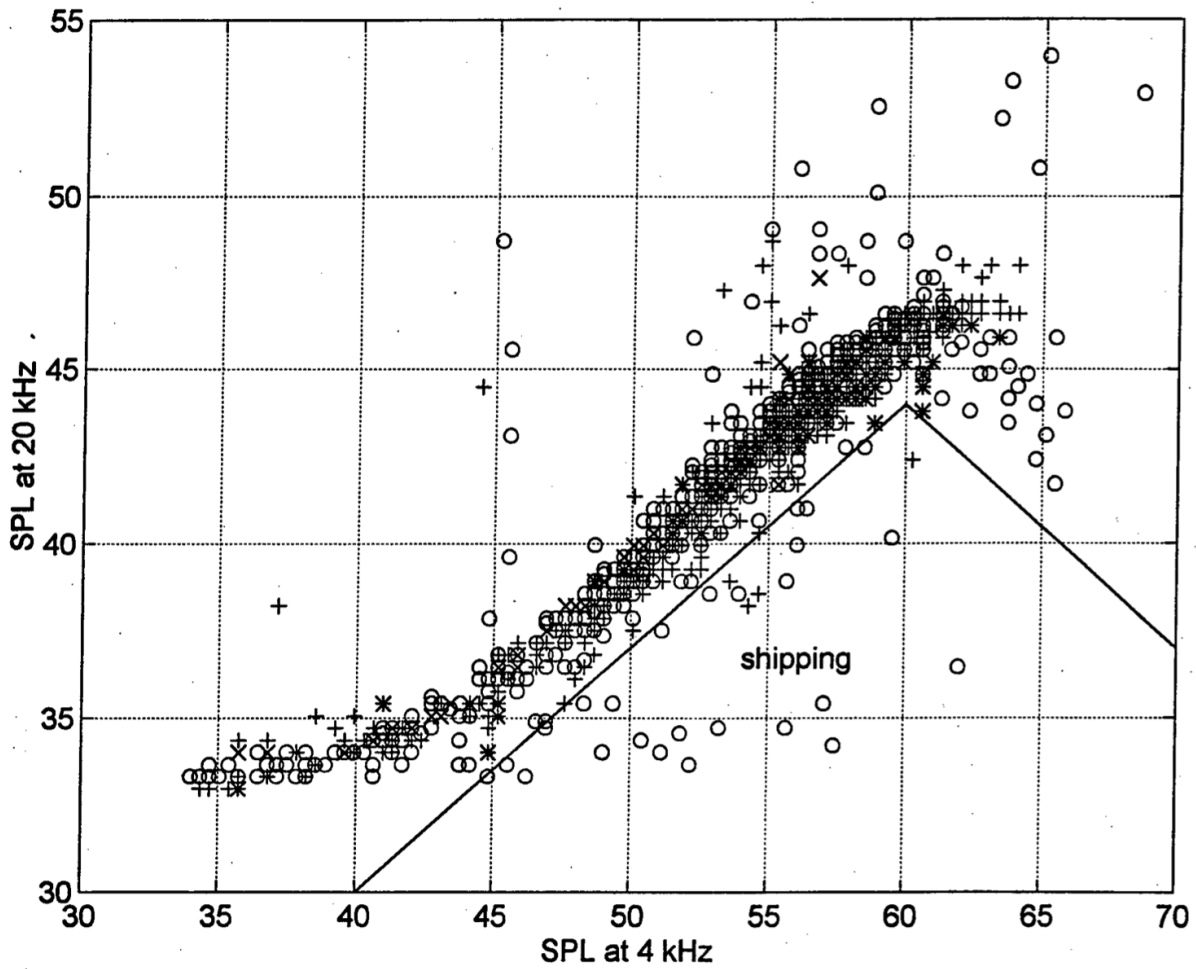
Figure 3.1: Shipping noise test presented by [20]. Lines indicate threshold of shipping noise. Different marker shapes correspond to different data collection locations. See [20] for reference.
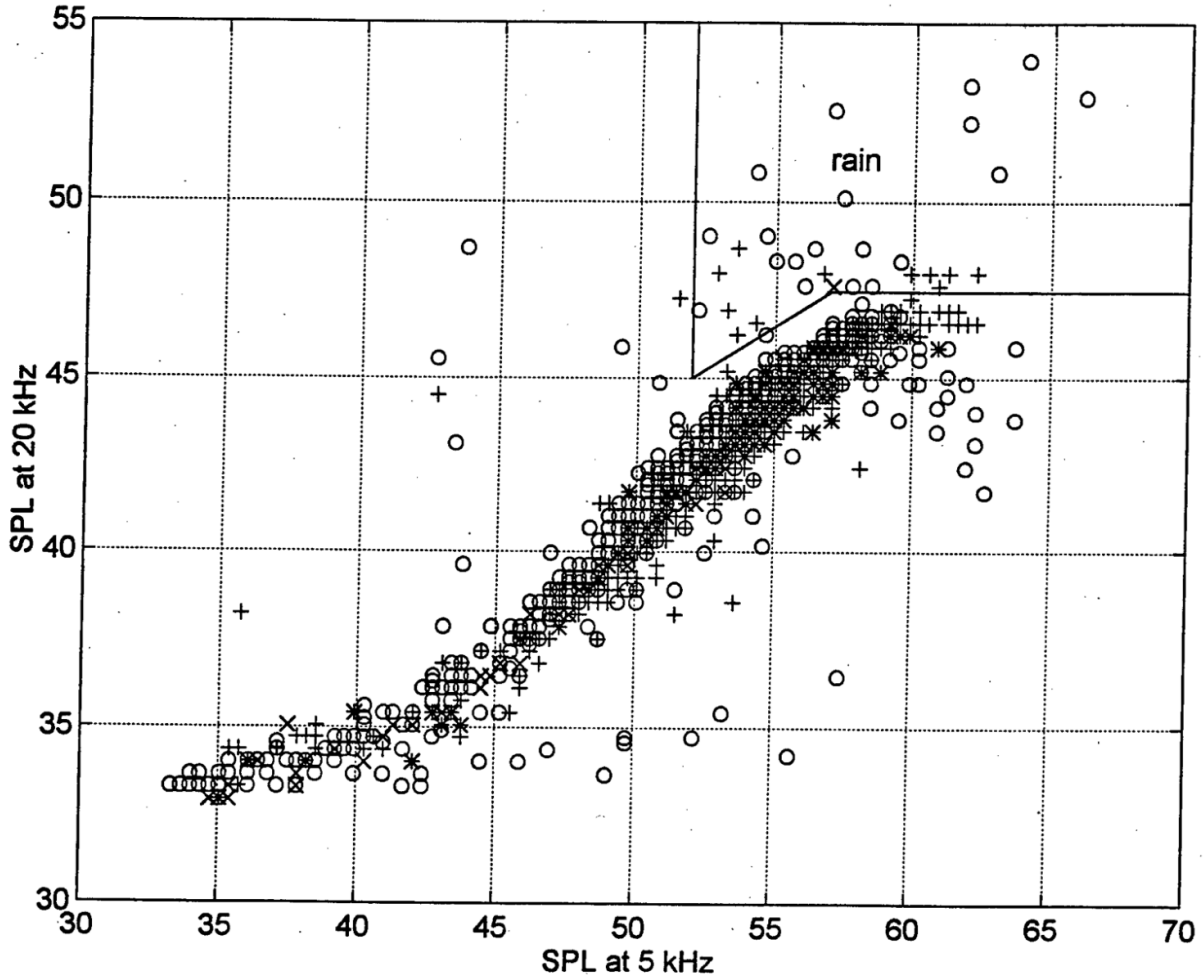
Figure 3.2: Rain noise test presented by [20]. Lines indicate threshold of rain noise. Different marker shapes correspond to different data collection locations. See [20] for reference.

$$SPL_{20kHz} + 1.1 \cdot SPL_{8kHz} > 109.5 \tag{3.44}$$

The next step in the algorithm involves checking the data for signs of drizzle or small rain drops. If equation 3.45 is satisfied then drizzle is likely present and is shown in figure 3.3.

$$SPL_{20kHz} > 0.8 \cdot SPL_{8kHz} + 4 \quad \text{and} \quad SPL_{20kHz} > 36 \tag{3.45}$$

Step 4 is a check for bubbles using equation 3.46. When ambient bubbles are present in the surface layer in high quantities noise levels are affected. High frequencies tend to be attenuated by small bubbles wheres
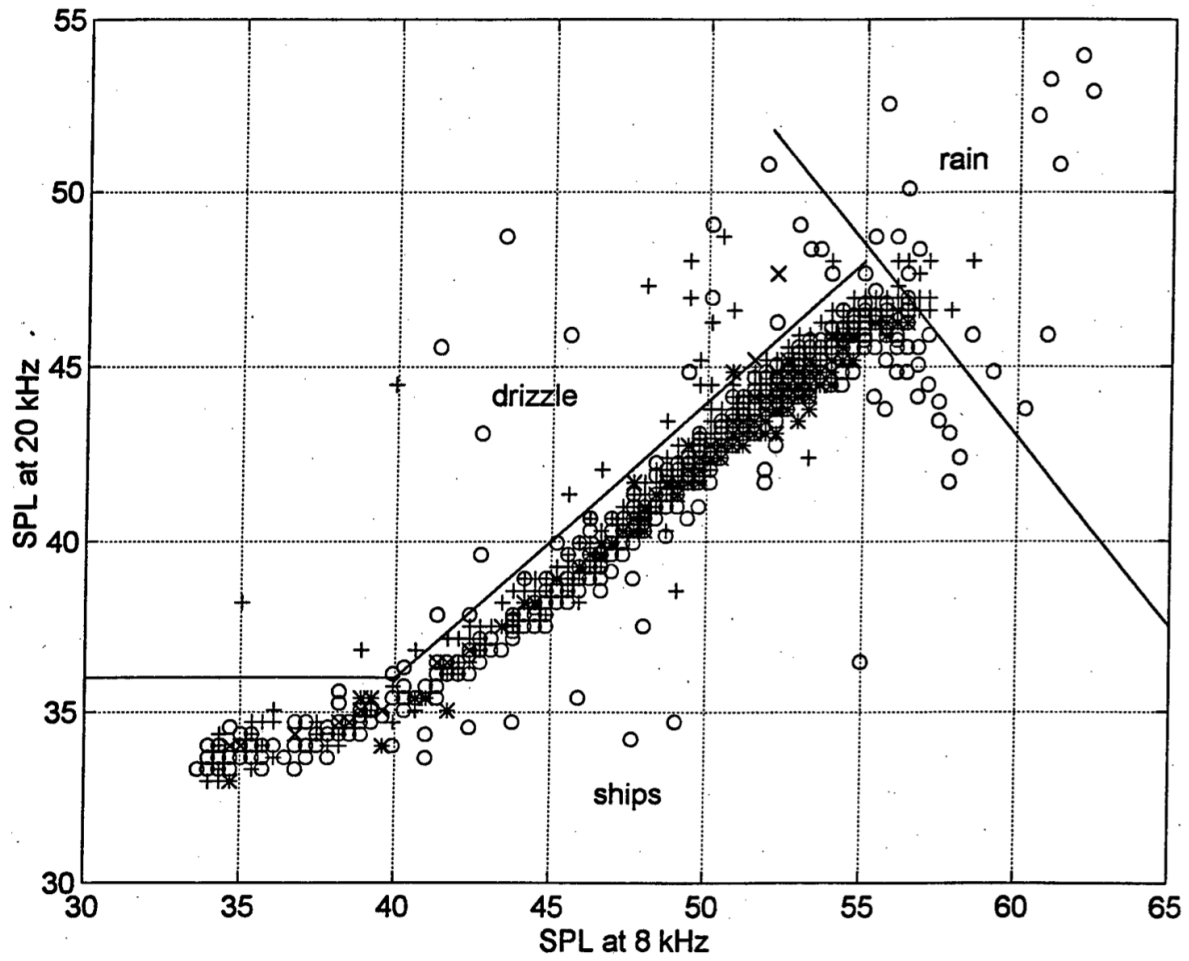
Figure 3.3: Drizzle noise test presented by [20]. Lines indicate threshold of drizzle noise. Different marker shapes correspond to different data collection locations. See [20] for reference.
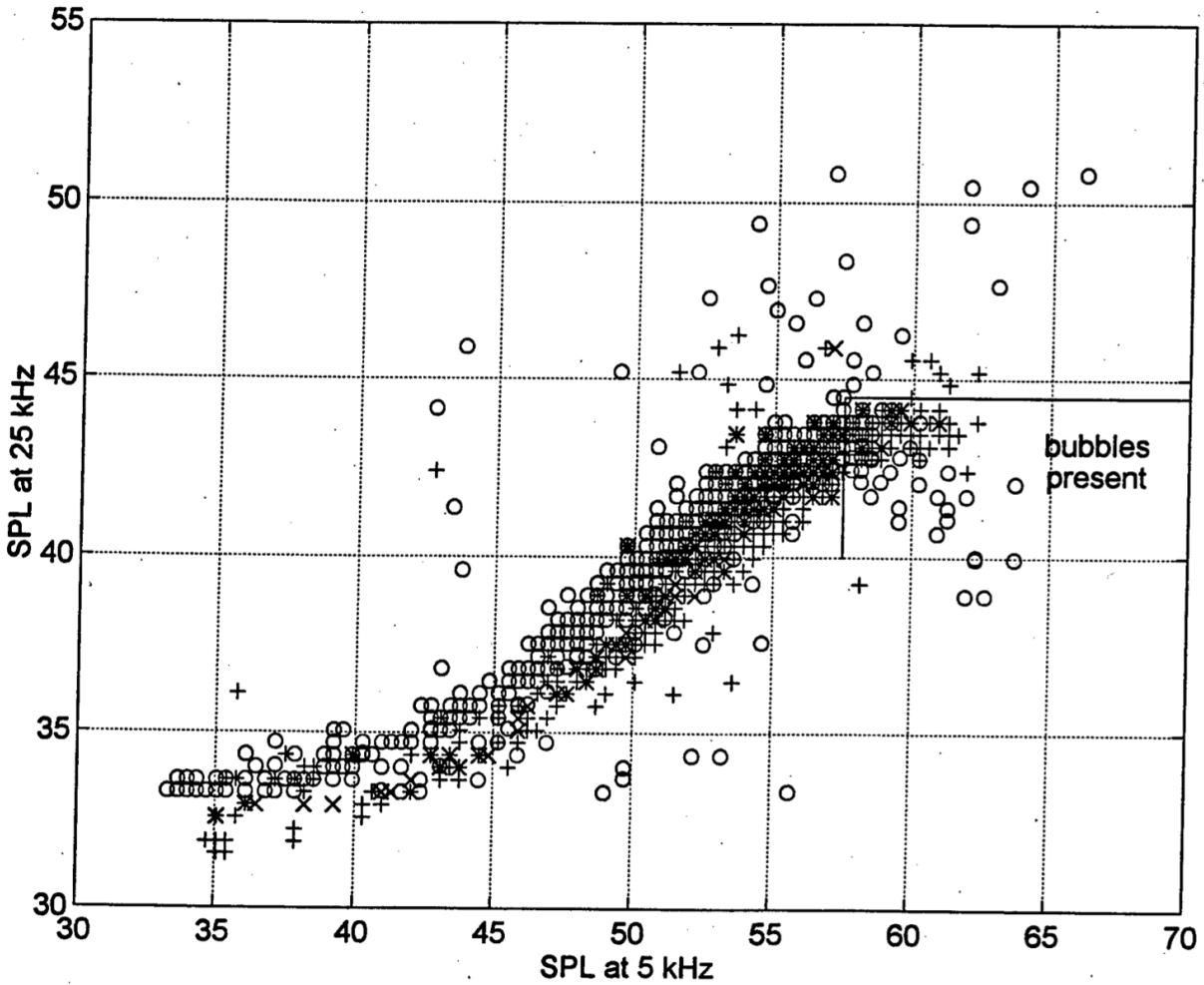
Figure 3.4: Bubble presence test presented by [20]. Lines indicate threshold where bubbles are likely present. Different marker shapes correspond to different data collection locations. See [20] for reference.

larger bubbles needed to attenuate lower frequencies are too buoyant to remain in the water column [20]. An example of this test is shown in figure 3.4.

$$SPL_{25kHz} < 44.5 \quad \text{and} \quad SPL_{5kHz} > 58 \tag{3.46}$$

The steps described above are used to assess the data's contamination and determine if the data is suitable for the wind speed algorithm to be used. The final step is to use the wind speed algorithm defined in section 3.3.1 to estimate the 10 m wind speed.

3.3.4 Bottom interaction correction

As presented above, wind speed and rainfall rate estimates can be derived from underwater noise levels. As sound propagates, it may interact with the ocean surface or the bottom and contribute to the observed noise. In the deep ocean, it is reasonable to assume that the sound source at the surface is equivalent to a plane on an infinite half-space. This does not hold in shallow areas due to bottom interactions. Therefore, surface and bottom interactions need to be considered, if wind speed and rainfall rate are to be estimated in shallow water. The following bottom interaction model is presented in [1].

Image sources may be used to describe bottom and surface reflections. The sound propagates from the source at the surface and reflects when it reaches the bottom. Upon reflection, sound will appear to originate from an image source, as shown in figure 3.5. This reflection will act as a dipole and the sound will continue to propagate in a single direction. Each reflection acts as an image source to the receiver and can be modelled as a source on a surface at a modified depth. This depth depends on the number of reflections that have occurred. Figure 3.5 presents the image surfaces for a signal after one and two reflections, with modified depths of $(2h - D)$ and $(2h + D)$, respectively.
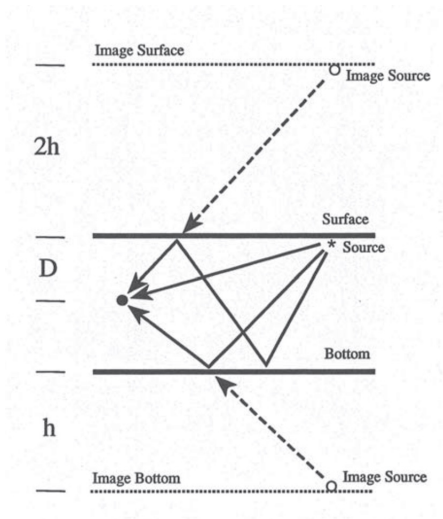
Figure 3.5: Image source model for sound reflections at an interface. Receiver is located at depth D.

If sound is assumed to be generated by uniformly distributed points on the ocean surface, then the sound intensity at the receiver can be calculated by,

$$I = \int_{\phi=0}^{2\pi} \int_{r=0}^{\infty} \frac{a^2}{R^2} \cos^2 \theta e^{-2\alpha R} r dr d\phi \qquad (3.47)$$

26

where ϕ and r are the angle and distance to a point above the receiver, a is the spatial source level density, R is the distance to the receiver, α is the absorption coefficient. The geometry is presented in figure 3.6 for a receiver at depth D and a source at the surface.
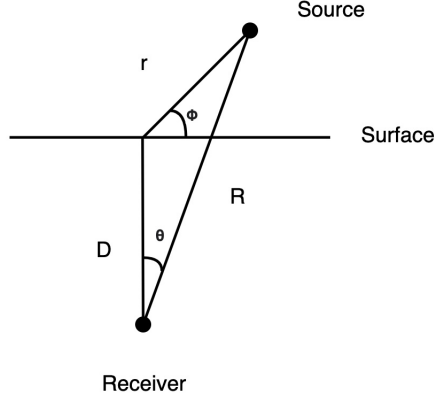
Figure 3.6: Geometry of receiver at depth D and surface source.

Integrating over the surface from $\phi = 0$ to $\phi = 2\pi$ yields a factor of 2π. Further, changing to an integration over θ equation 3.47 can be written as,

$$I = 2\pi a^2 \int_0^{\pi/2} \cos^3 \theta \sin \theta e^{-2\alpha D/\cos \theta} d\theta \tag{3.48}$$

Next, bottom and surface interactions can be included. Let β and γ represent the acoustic energy absorbed through bottom and surface interactions, then equation 3.48 becomes,

$$I = 2\pi a^2 \int_0^{\pi/2} \cos^3 \theta \sin \theta (e^{-2\alpha D/\cos \theta} + \beta e^{-2\alpha(2h-D)/\cos \theta} + \beta\gamma e^{-2\alpha(2h+D)/\cos \theta} + ...)d\theta \tag{3.49}$$

Finally, noting that the infinite sum in the integrand of equation 3.49 is a geometric series yields,

$$I = 2\pi a^2 \int_0^{\pi/2} \cos^3 \theta \sin \theta ((\frac{e^{4\alpha h/cos\theta}}{\beta\gamma} - 1)^{-1}(e^{-2\alpha D/\cos \theta} + \frac{1}{\gamma}e^{2\alpha D/\cos \theta}) + e^{-2\alpha D/\cos \theta})d\theta \tag{3.50}$$

The effects of this bottom correction model, equation 3.50, are presented in figure 3.7. In all cases, the surface reflection coefficient is chosen as $\gamma = 1$ assuming that any losses at the surface will be small and will not result in loss of energy. The effect of the instrument depth is shown in the top panel of figure 3.7 which corresponds to the frequency dependent absorption, α. The sound level is reduced at high frequencies and
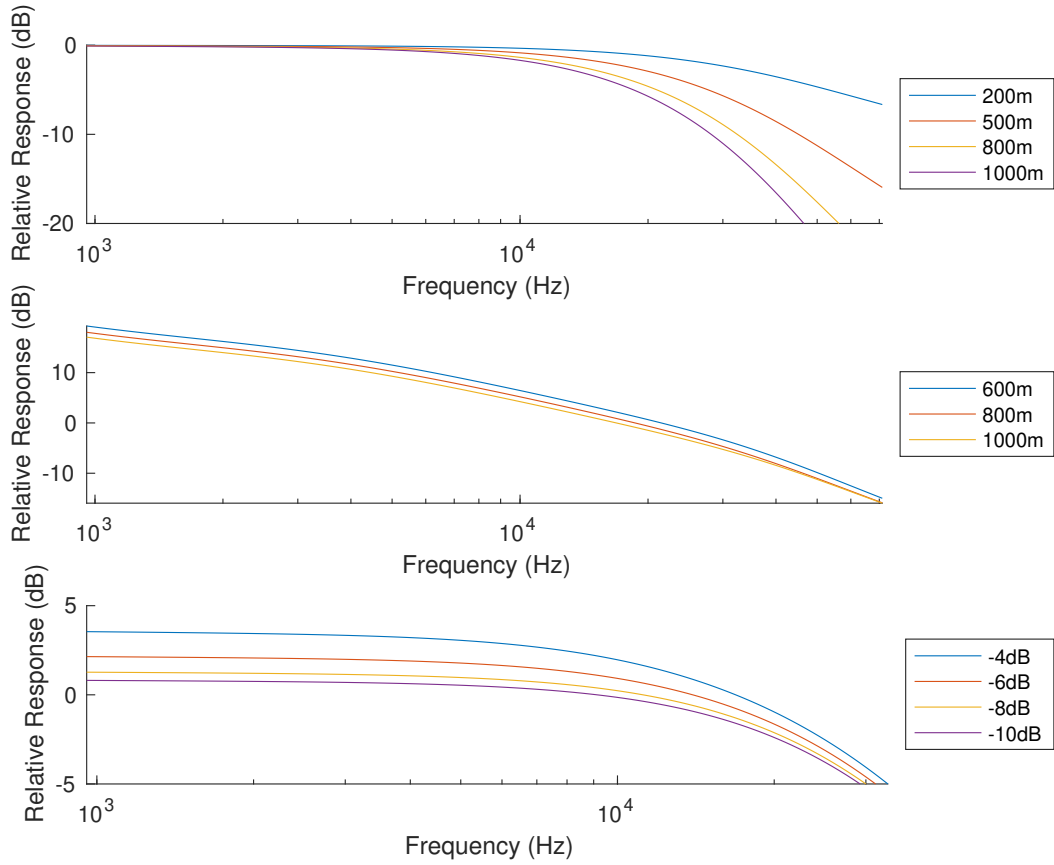
Figure 3.7: Bottom interaction model effects. Top panel presents the effects of acoustic absorption with no bottom reflections for depths of 200m, 500m, 800m, 1000m. Middle panel presents the bottom effects for an instrument at a depth of 500m and a bottom depth of 600m, 800m and 1000m. Lower panel presents the bottom effects for an instrument positioned on the bottom at 500m with bottom attenuations of -4dB, -6dB, -8dB and -10dB.

varies with instrument depth. The middle panel of figure 3.7 presents the effect of bottom reflections for an instrument at 500m and the bottom at 600m, 800m and 1000m. Here, no attenuation or bottom losses are considered and the effects are attributed to absorption losses. Bottom reflection losses are considered in the bottom panel of figure 3.7. Bottom reflection coefficients are evaluated ranging from -10 dB to -4 dB. The frequency dependence observed in this curve is a result of absorption, as the current model assumes that the bottom reflections are independent of frequency [1].

Chapter 4

Data acquisition

4.1 Area of interest

Ambient noise recordings were collected on the northeastern edge of Saglek bank, off the coast of Northern Labrador. The exact location of moorings HiBioA-17 and HiBioA-19 are shown in figure 4.1, which are positioned approximately 1 nautical mile apart. This area is of interest for several reasons. Firstly, high current speeds are observed on the edge of Saglek bank. These currents are tidally driven and highly influenced by the Frobisher bay tidal dynamics where the tidal heights reach nearly 11 meters. The strong currents are thought to bring a large quantity of nutrients to the area, leading to a rich biodiversity. Notably, various species of corals, sponges and other marine organisms have been observed and collected in the surrounding area. Moreover, marine mammals known to visit this area include pilot whales, white-beaked dolphins and bottlenose whales [7].

Additionally, the coast of Northern Labrador is an area that sees very limited shipping activity. Figure 5.15 presents shipping traffic within 100 km of the mooring locations during the deployment periods. In this area, 5 ships were present during the deployment period from 2019-2020 and 1 ship was present over the 2017-2018 period. The limited shipping activity in this area allows ocean noise observations to be made in the absence of anthropogenic noise.
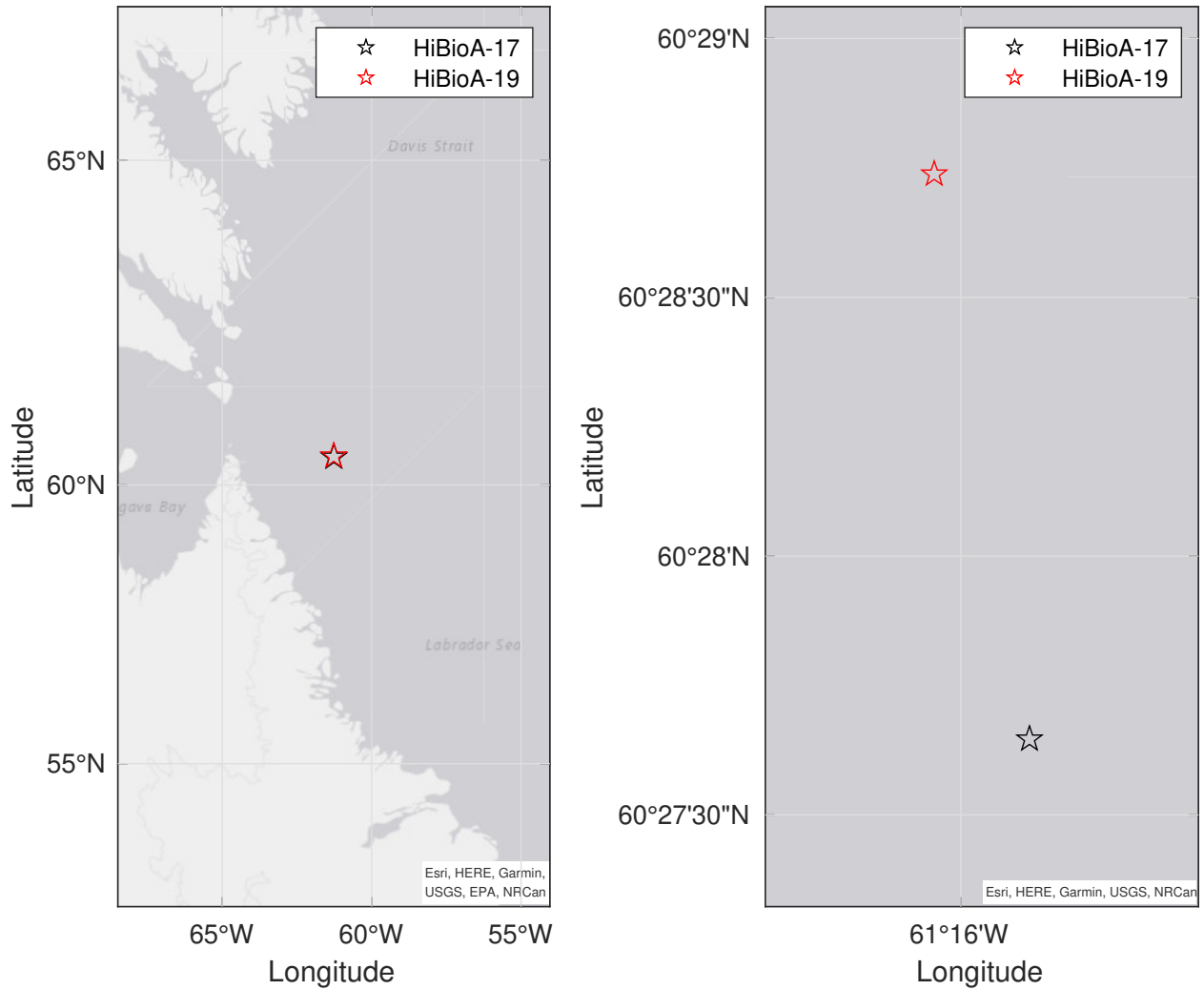
Figure 4.1: HiBioA-17 and HiBioA-19 mooring location off the coast of Northern Labrador shown as black and red stars, respectively. Right panel presents a closer view of the location shown in the left panel. HiBioA-17 was deployed from October 2017 to March 2018 at (60 27.6464 N, 61 15.7307 W). HiBioA-19 was deployed from July 2019 to September 2020 at (60 28.738 N, 61 16.1043 W).
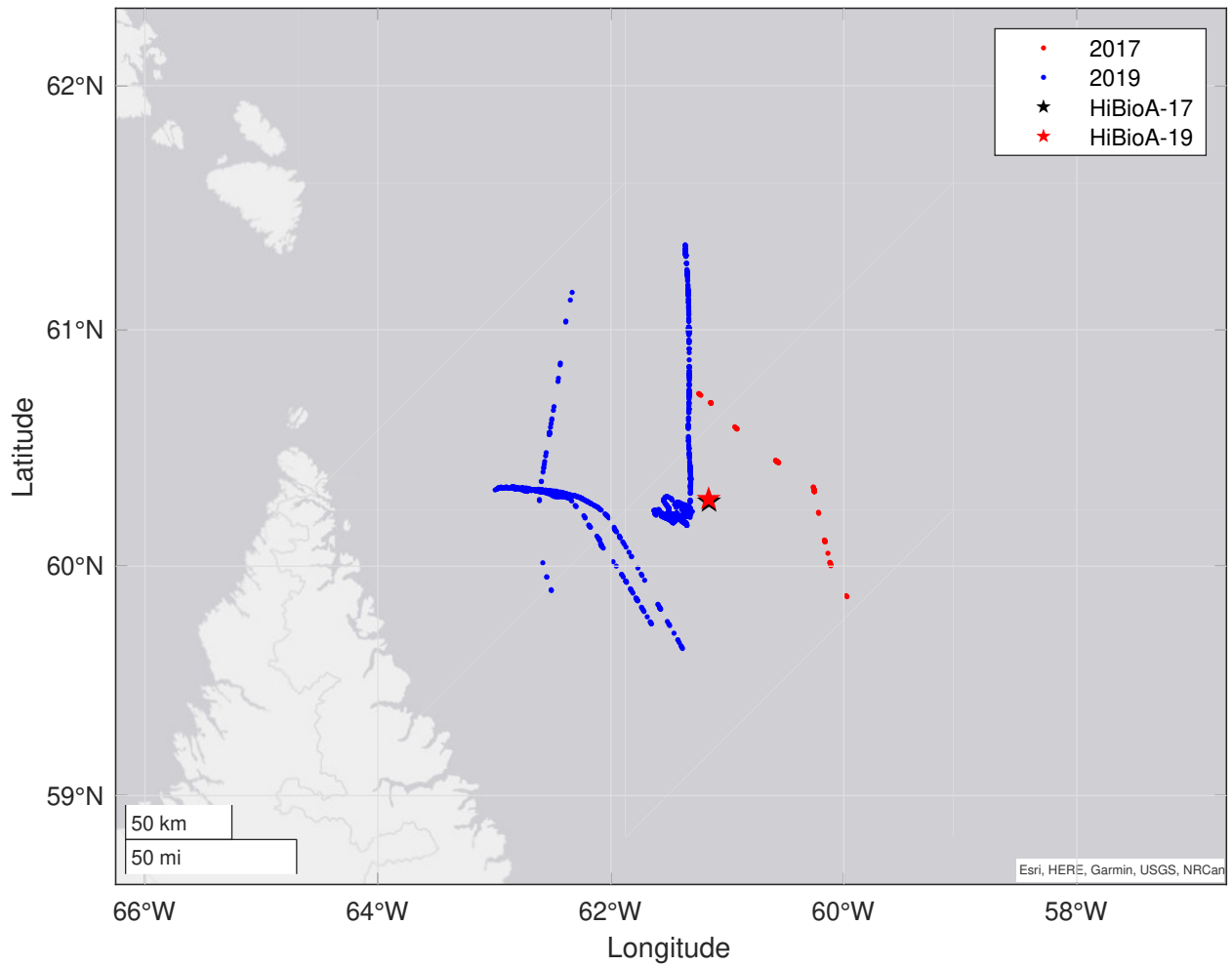
Figure 4.2: Shipping traffic from October 2017 to March 2018 shown as red dots. Shipping traffic from July 2019 to September 2020 shown as blue dots. Traffic present within 100 km of the mooring locations is shown. Mooring locations are shown as black and red stars.

The surrounding bathymetry is presented in figure 4.3. HiBioA-17 and HiBioA-19 were deployed at a depth of approximately 500 m. The moorings are located on the edge of Saglek bank where the ocean floor slopes down to the East and eventually reaches depths of nearly 1000 m, which is associated with the deep ocean. Tidal currents are normally relatively weak in the deep ocean but are amplified as they interact with the steep shelf edge. The steep topography in this area will serve to steer currents along the slope and coastal Kelvin waves will be channeled along the shelf break. Notably, the southward flow of the Labrador current and the strong currents associated with the tidal resonance that occurs in Frobisher bay are important in this area.
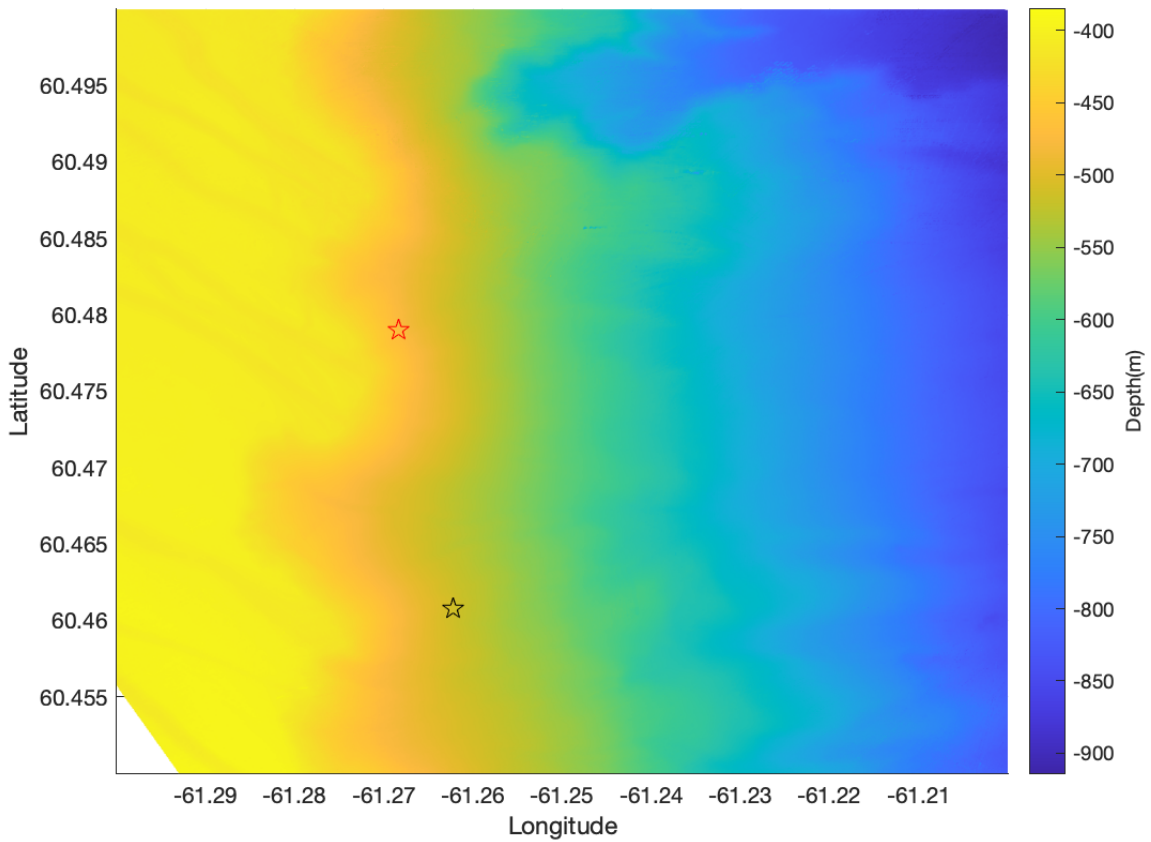
Figure 4.3: Bathymetry surrounding mooring location. Colorbar indicates depth. Moorings are shown as red and black stars.

4.2 Instrumentation

Acoustic noise recordings and current velocity measurements were made as part of two mooring deployments. HiBioA-17 was deployed from October 2017 to the end July 2018. Acoustic data corresponding to this mooring is available until March 2018. HiBioA-19 was deployed from July 2019 to the end of August 2020. An internal malfunction led to current meter data being recorded for only the first 4 months of the deployment period. Both moorings were equipped with an Autonomous Multichannel Acoustic Recorder (AMAR), sediment trap and settlement plate. The mooring design of HiBioA-19 is shown in figure 4.4.
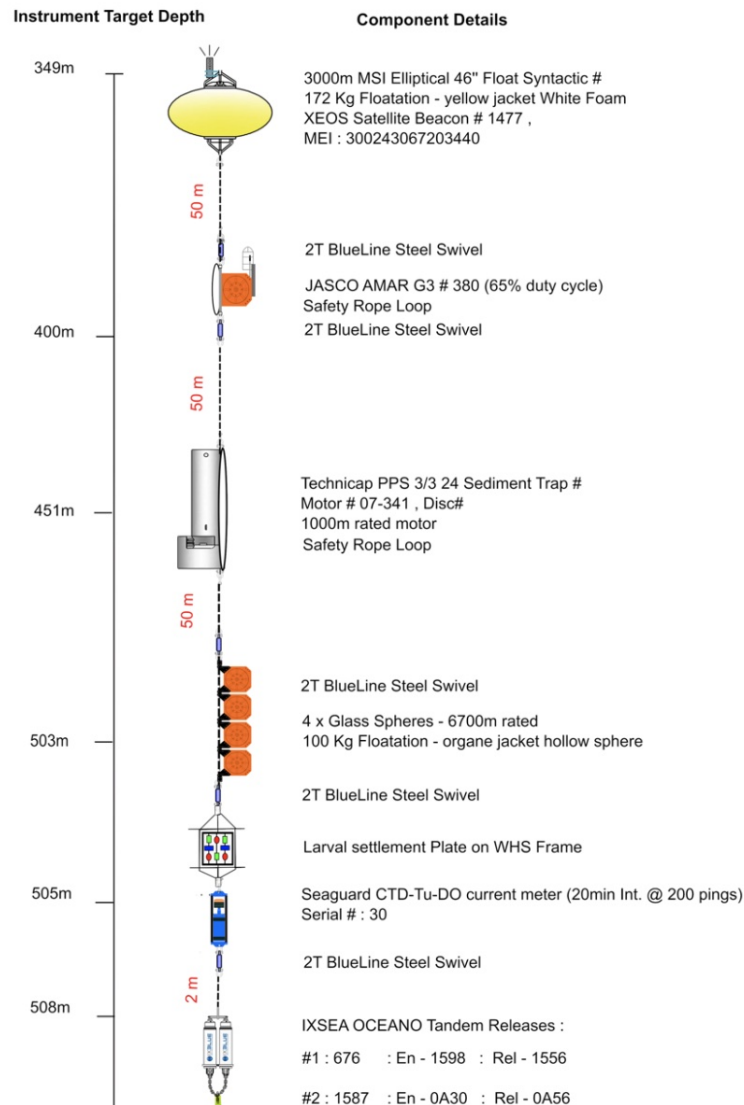
Figure 4.4: HiBioA-19 mooring design.

The HiBioA-17 mooring design was similar to figure 4.4, where a three beam ADCP was used to measure current velocities. The HiBioA-19 mooring included a CTD-Tu-DO current meter which measures conductivity, temperature, density, turbidity and dissolved oxygen in addition to current velocities. The AMARs for both moorings were outfitted with omnidirectional hydrophones with sampling frequencies of 8 kHz and 250 kHz.

4.3   ADCP depth cell mapping

The bottom mounted moorings were significantly affected by the high current speeds in this area such that they were knocked over and tilt angles became important. Tilt angles, as reported by the in-line current meter, reached 30 degrees. Pitch and roll values over the deployment period for HiBioA-17 are presented in figure 4.5. Large tilt angles may lead to artificial vertical velocities, and make high horizontal speeds suspect. As the current meter was downward looking and only 10 m from the bottom, vertical velocities should be negligible. Depth cell mapping may be used to correct for the high tilt of the current meter, thus ensuring that data is consistent in depth from the surface.

In order to resolve this issue, a depth correction that reorganizes data points with depth is applied. The top panel of figure 4.6 shows the apparent vertical velocities with and without the depth correction. Vertical velocities reach 0.1 m/s. The difference of the velocities is shown in the lower panel of figure 4.6. A velocity difference between 0.05 m/s and 0.1 m/s is observed when the depth correction is applied. However, the overall scale of the vertical velocity remains unchanged.
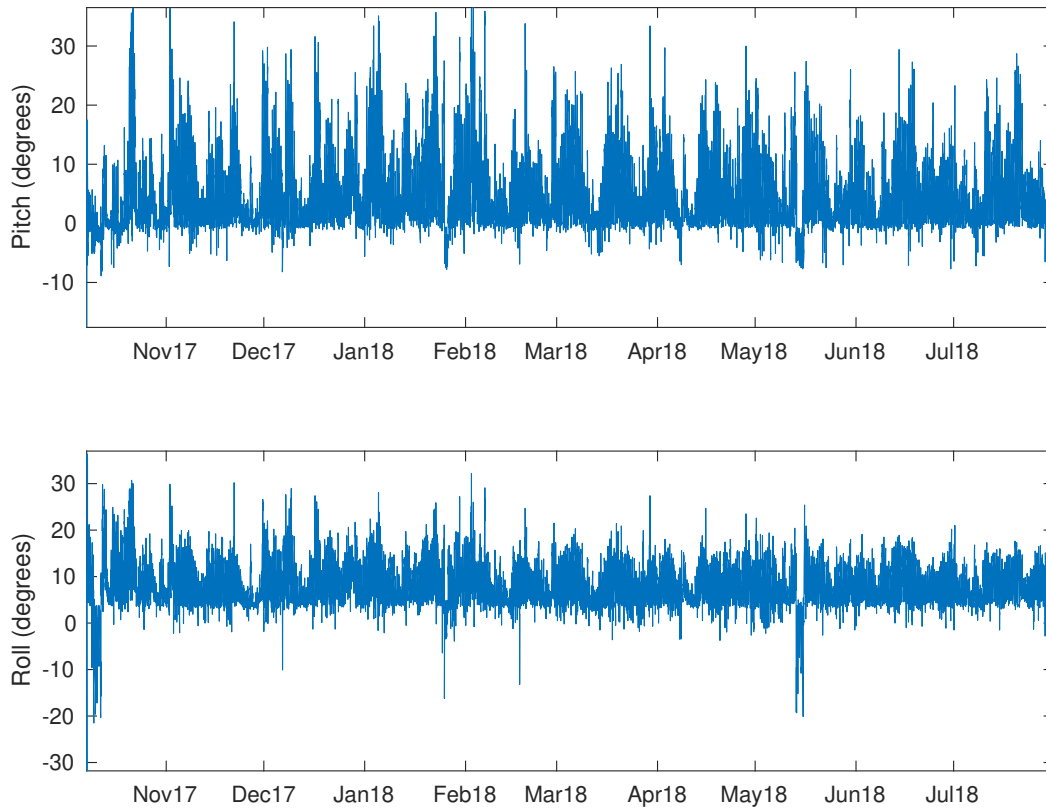
Figure 4.5: Pitch and roll of current meter over deployment period for HiBioA-17 mooring. Pitch and roll angles in degrees.
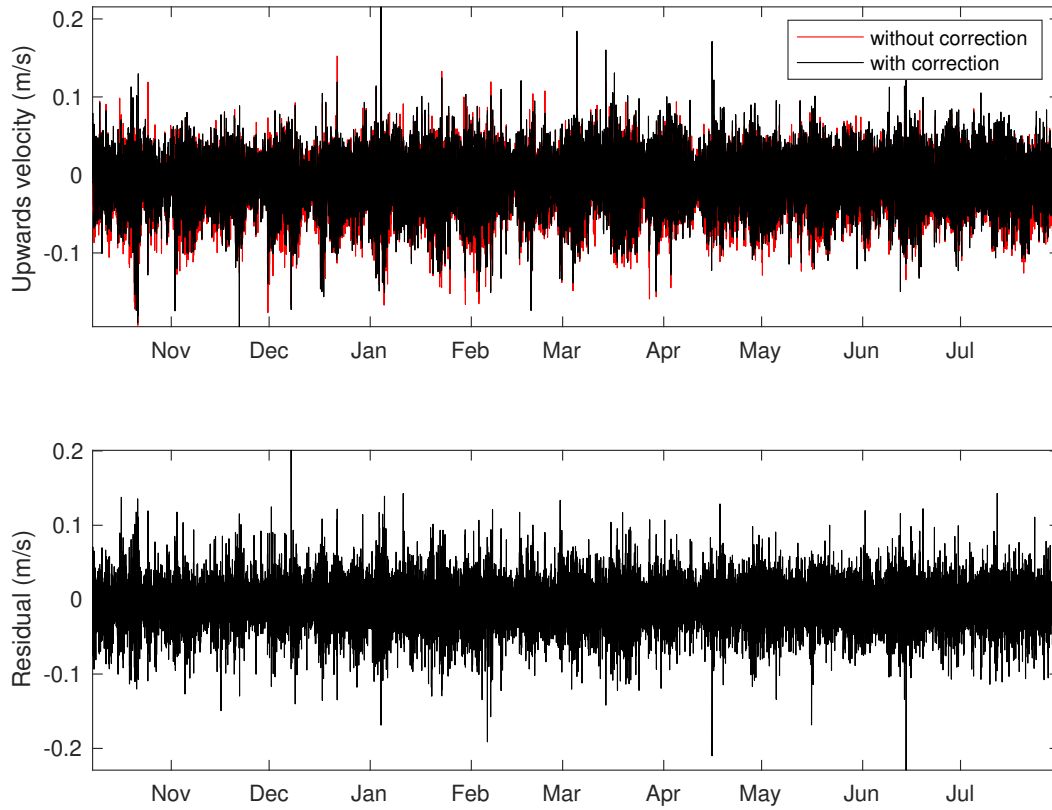
Figure 4.6: Vertical velocities in m/s with (black) and without (red) depth correction shown in the top panel. Residual values in m/s are shown in the lower panel.

Chapter 5

Results

5.1 Current measurements

Current velocity measurements from October 2017 to March 2018 are shown in figure 5.1. A 3 beam ADCP was used and thus, Eastward, northward and upwards velocities are presented. The average velocity up to 5 meters away from the ADCP head is shown. Depth cell correction has been applied to these measurements, as presented in section 4.3, in order to resolve the larger than expected upwards velocity component. The remaining vertical velocities will retain some of the bias associated with instrument tilt. Eastward and northward velocity measurements from a point current meter from July 2019 to November 2019 are shown in figure 5.2. Current velocities reach a maximum of around 0.5 m/s with a dominant northwest and southeast direction.
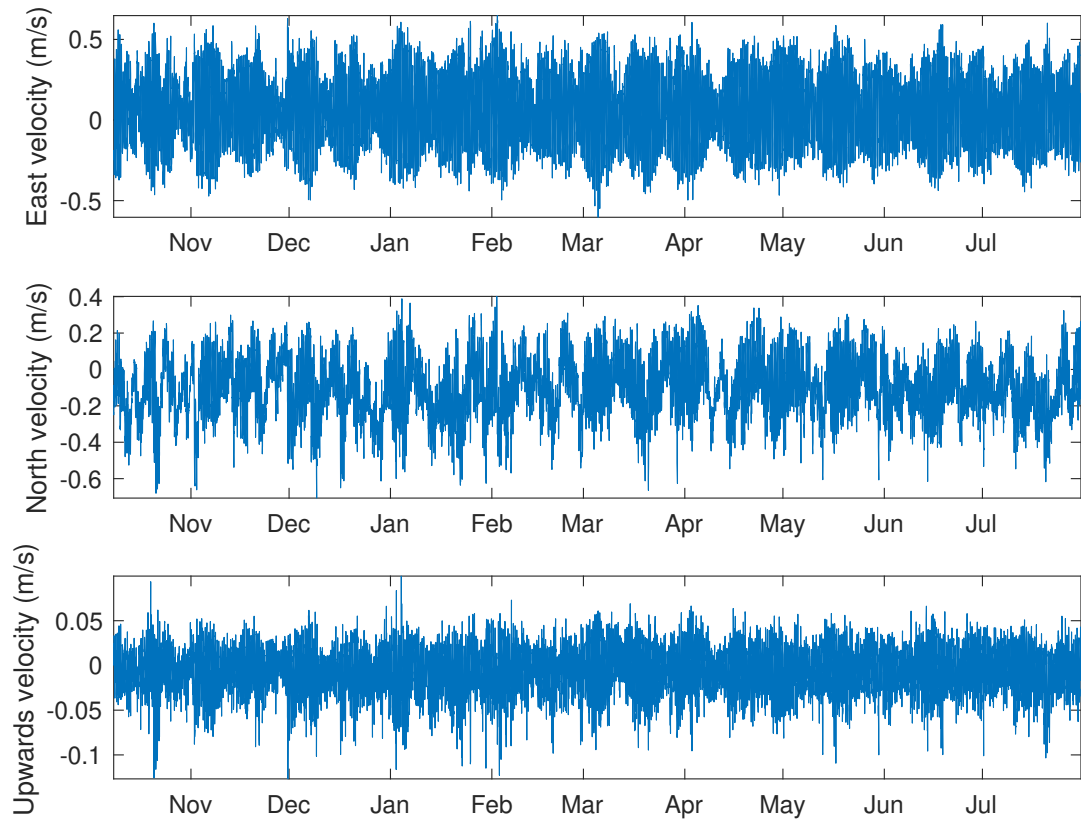
Figure 5.1: Eastward, northward and upwards velocities shown in top, middle and lower panels respectively. Velocities presented from October 2017 to March 2018.
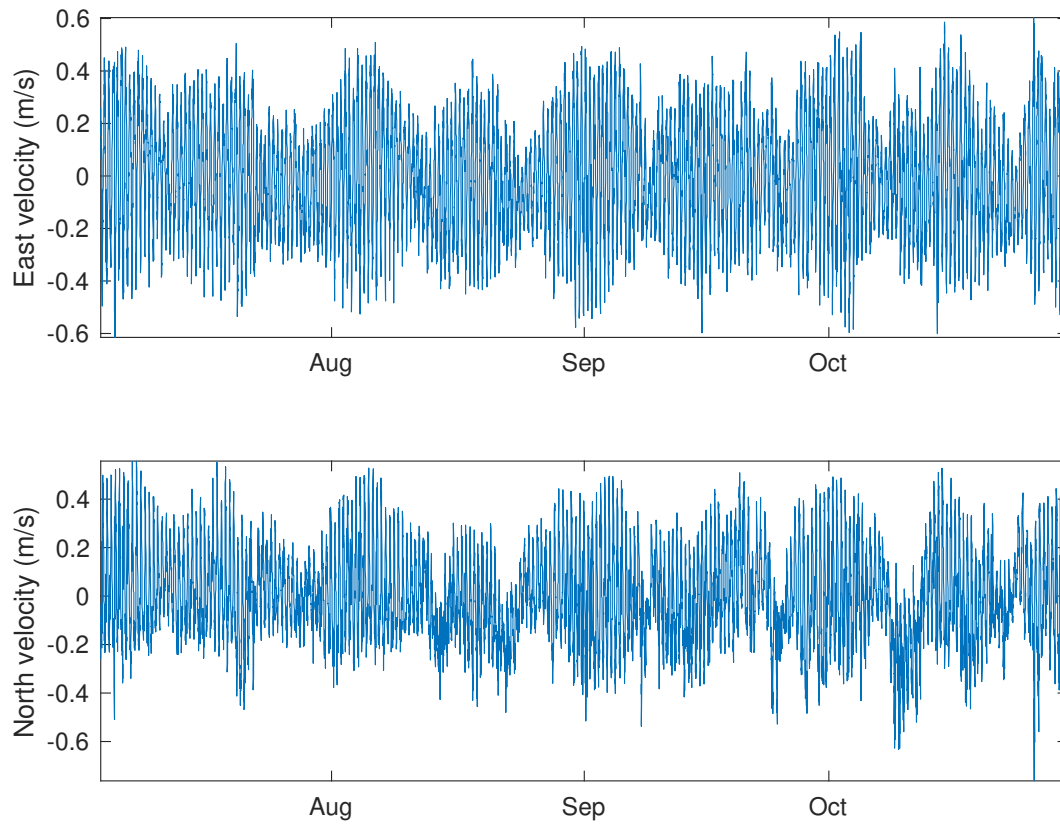
Figure 5.2: Eastward and northward velocities shown in upper and lower panels respectively. Velocities presented from July 2019 to November 2019.

The power present in the current speed time series as a function of frequency is presented in figure 5.3. Dominant cycles are seen at approximately 2, 4 and 8 cycles per day, corresponding to tidal variations. The 4 and 8 cycles per day are suggestive of non-linear effects such as rectification. Thus, currents are tidally driven and tidal harmonic analysis can be used to estimate future current speeds.
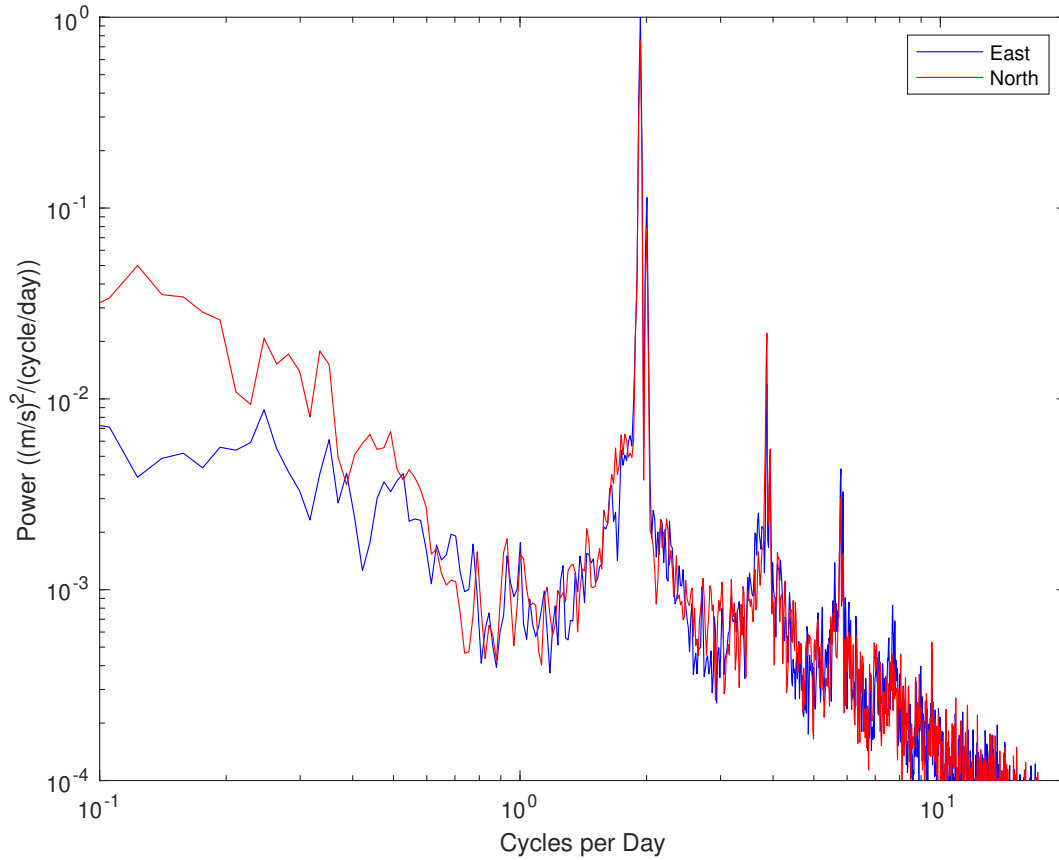
Figure 5.3: Power contained in current speed signals from October 2017 to March 2018 as a function of frequency. Dominant cycles at 2/day, 4/day and 8/day are tidal in origin.

5.2   Tidal prediction

The current meter on mooring HiBioA-19 suffered an internal malfunction, causing current measurements to be made up to November 2019 only. Following from tidal harmonic analysis, tidal predictions may be used to extend the observed current velocities over the remaining deployment period.

Tidal harmonic analysis was applied to obtain current speed estimates up to September 2020. The "T-TIDE" package was used for this analysis [23]. The estimated tidal components of the current velocity measurements from July 2019 to November 2019 are shown in figure 5.4 along with the original current observations. The difference of the two signals is presented in red and represents the non-tidal variations in the current speeds. The peak current velocities of the original time series tend to be larger than the peak velocities of the estimated tidal component.
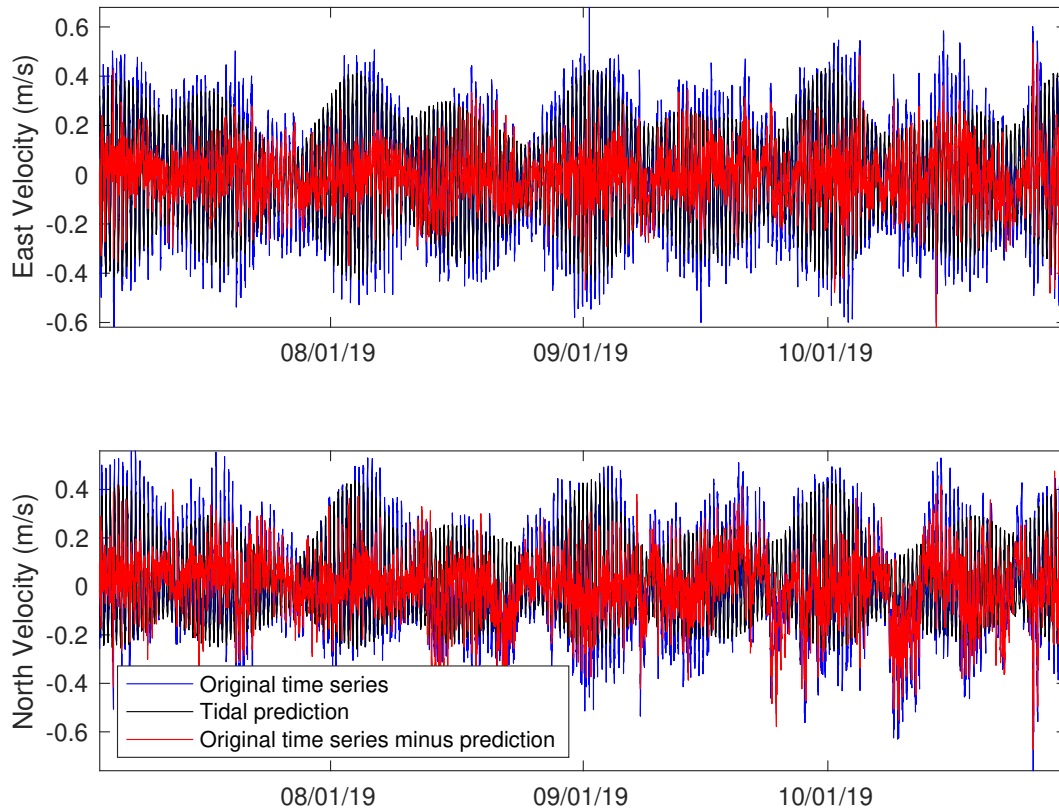
Figure 5.4: Original current speed time series (blue) and tidal component of current speed (black). Difference shown in red. Top panel present the eastward velocity and the lower panel presents the northward velocity. Current velocity measured in m/s.

The estimated tidal components presented in figure 5.4 are then used to predict future tidal current velocities that would occur beyond the time of the observations. Figure 5.5 presents the tidal prediction of the Northward and Eastward current velocities up to September 2020 in blue and the estimated tidal component of the observations in black. The velocity estimates reach approximately 0.4 m/s. The spring and neap tide cycle is clearly shown by the peaks and trough of the envelope of the signal.
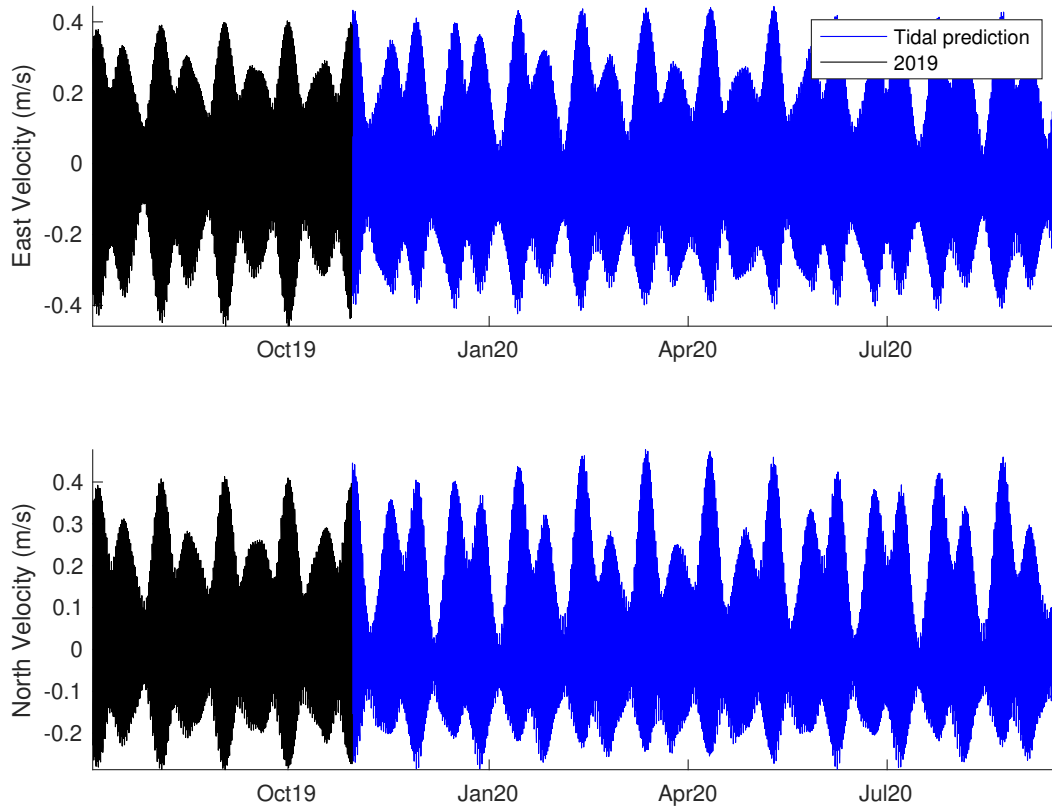
Figure 5.5: Estimated tidal component of current speeds and extended tidal prediction shown in black and blue, respectively. Top panel present the eastward velocity and the lower panel presents the northward velocity. Current velocity measured in m/s.

5.2.1 Tidal prediction for ROV dive support

In July and August 2021 the Amundsen cruise travelled from St. John's, Newfoundland to Iqaluit, Nunavut in order to recover moorings and continue the Saglek Bank and Labrador Sea biological research. Remotely operated vehicle (ROV) operations are sensitive to current speed and thus, current predictions were needed

to optimise ROV dives and sample collection near the mooring location.

The tidal prediction presented in figure 5.5 was extended by over one year up to the end of July 2021, and is shown as a blue line in figure 5.6 for July 24 2021 and July 25 2021. Prior to the ROV dive, direct current velocity measurements were possible and are shown in figure 5.6. The measurements suggest good agreement with the predictions, although some uncertainty is observed. The uncertainty may be attributed to non-tidal variations, errors in the predicted values or clock drift of the current meter.
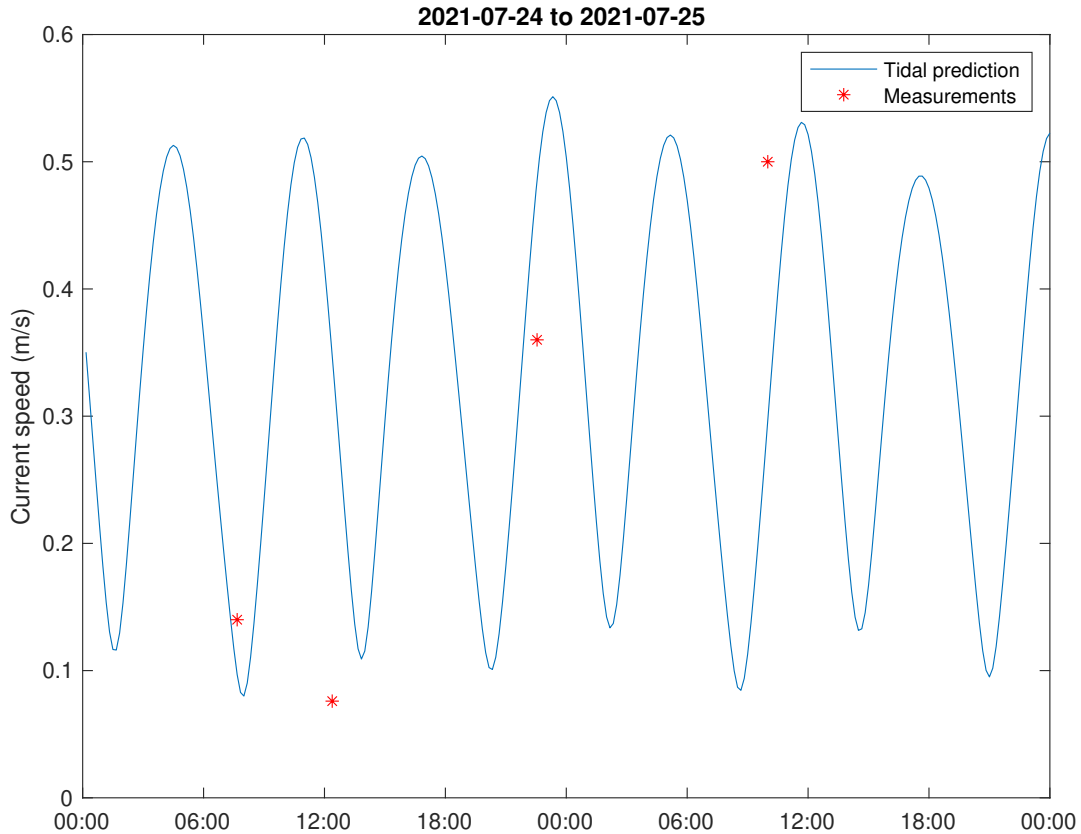
Figure 5.6: Tidal prediction for July 24 2021 and July 25 2021. Measured current speeds shown as red stars. Current speed in m/s.

5.3   Acoustic measurements

Noise levels recorded with the AMAR from October 2017 to March 2018 are shown in figure 5.7. The spectra are characterized by periods of high power at low frequency as a result of noise contamination associated with high current speeds. Further, a decrease in power is observed at high frequencies which is expected in the case of ocean noise.
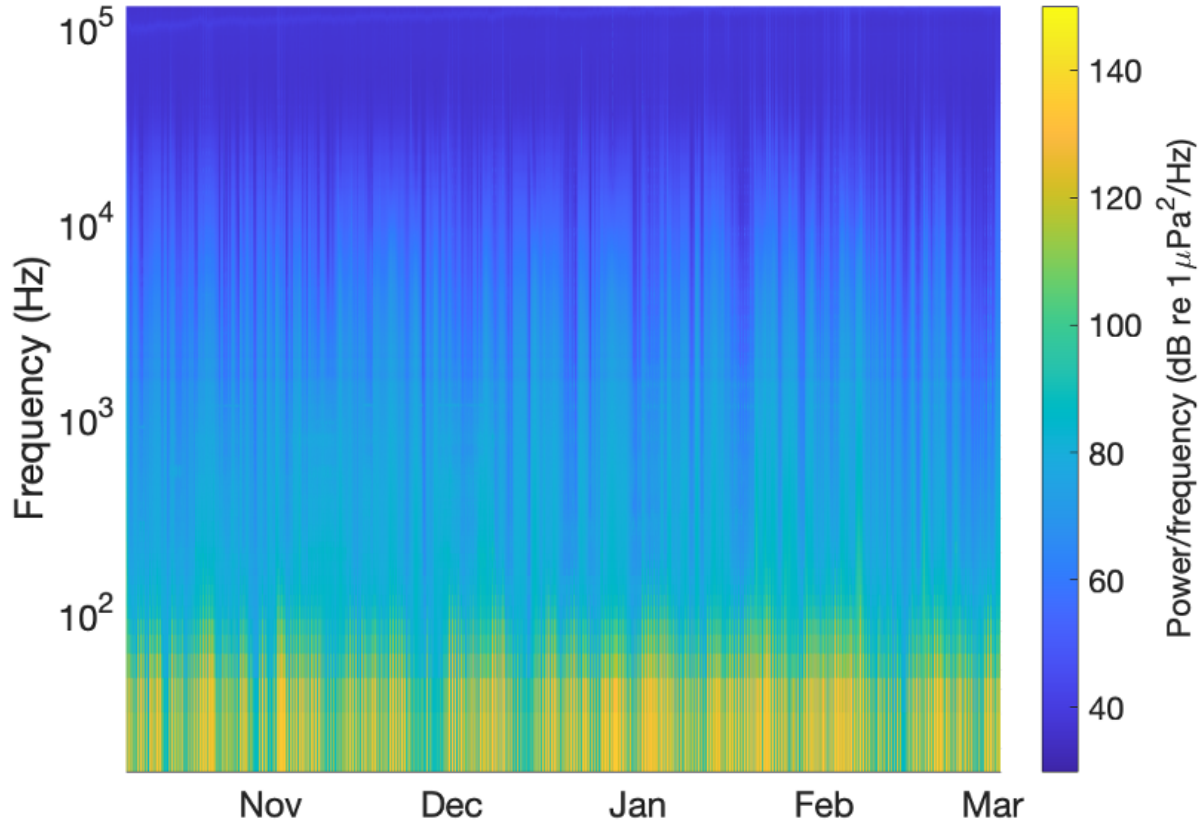
Figure 5.7: Noise levels as a function of frequency from October 2017 to March 2018.

To identify the impact of current speeds on noise levels, the noise levels were sorted with increasing current speed using the corresponding current velocity measurements presented in section 5.1. The result for noise levels from October 2017 to March 2018 are presented in figure 5.8. Noise levels at low frequency increase with current speed. Quiet periods are observed below approximately 0.2 m/s after which an important increase in power occurs. As naturally occurring ocean noise levels are not associated with current speed, this sorting method should yield unbiased noise levels.
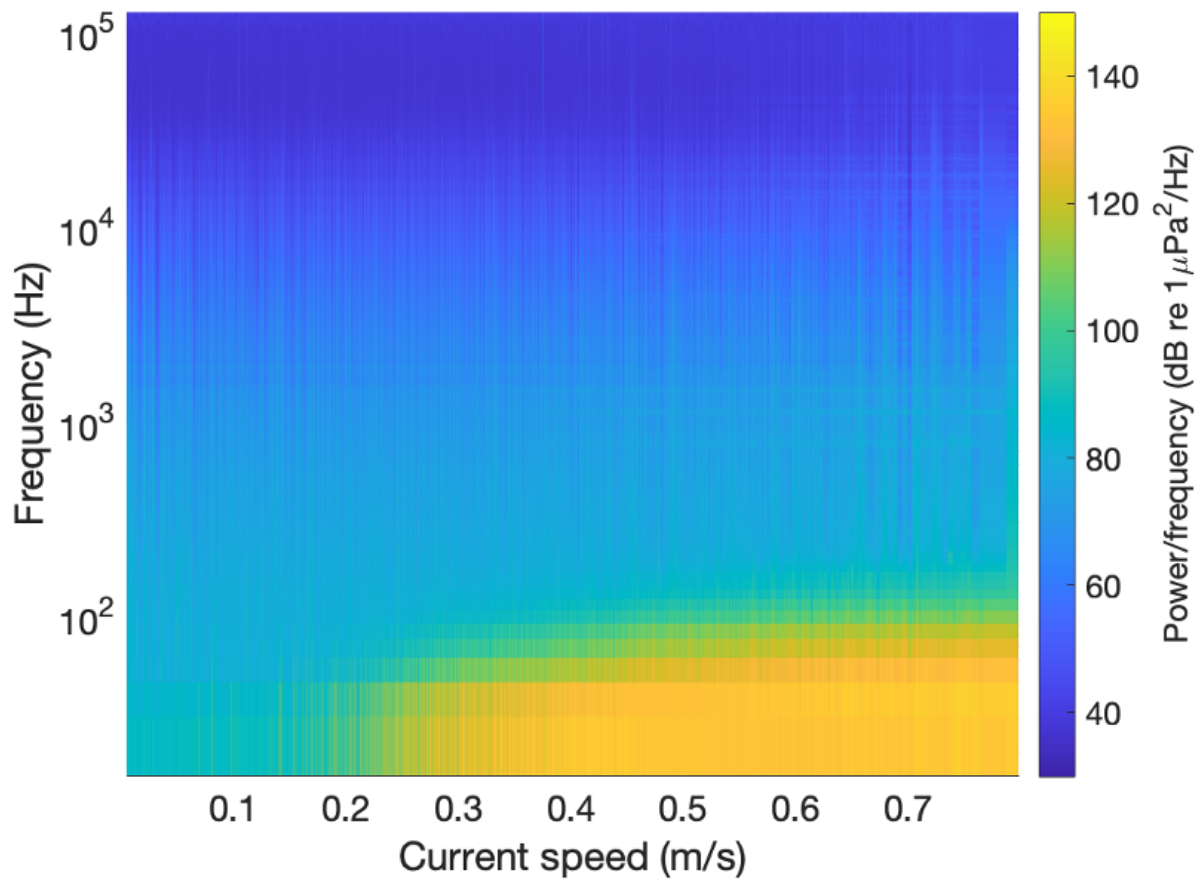
Figure 5.8: Noise levels as a function of frequency from October 2017 to March 2018 sorted with increasing current speed.

In order to recover naturally occurring ambient sound levels, a current speed threshold was selected. Figure 5.9 presents the noise spectra as a function of time where only periods with corresponding current speeds of 0.2 m/s or less are included. The resulting spectrogram show substantially reduced noise levels at low frequency.
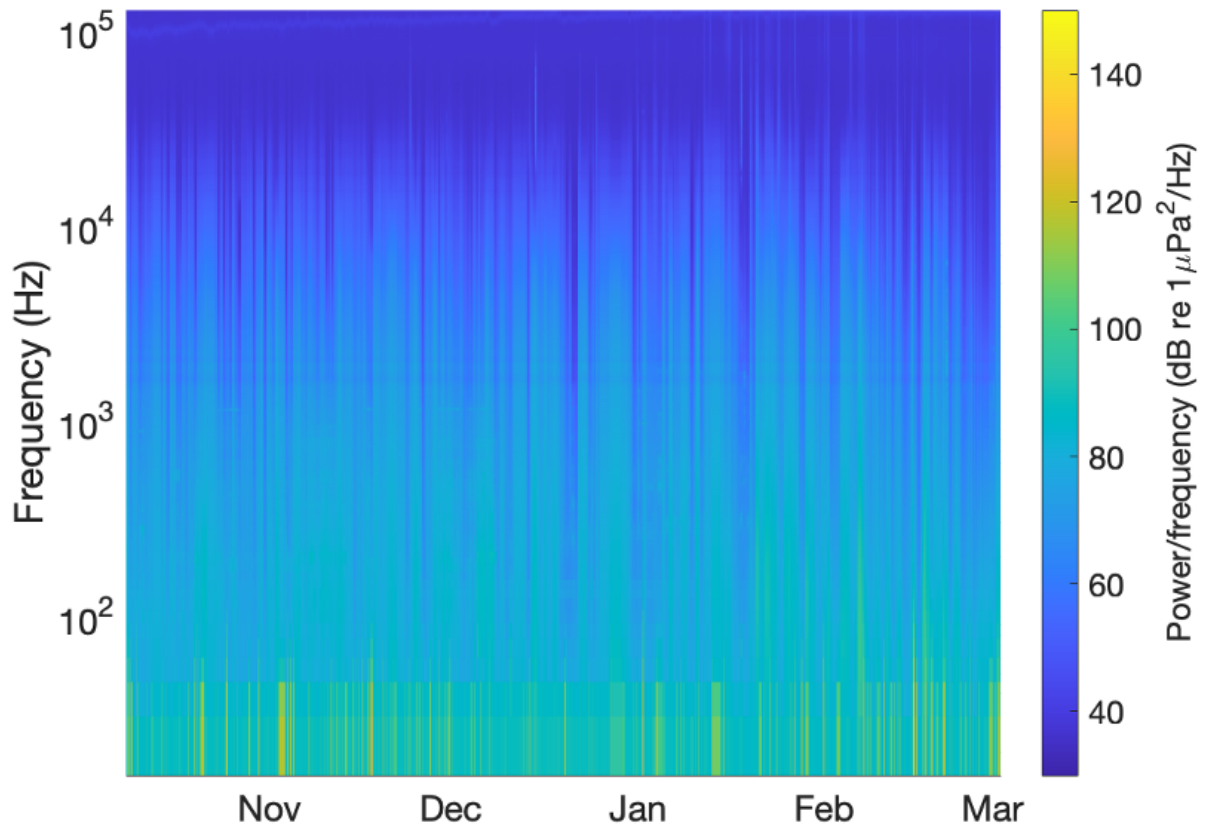
Figure 5.9: Noise levels as a function of frequency from October 2017 to March 2018 when corresponding current speeds were less than 0.2 m/s.

The procedure to eliminate mooring noise in the 2018 data was repeated using the data collected from July 2019 to September 2020. Noise levels recorded over this time period are shown in figure 5.10.
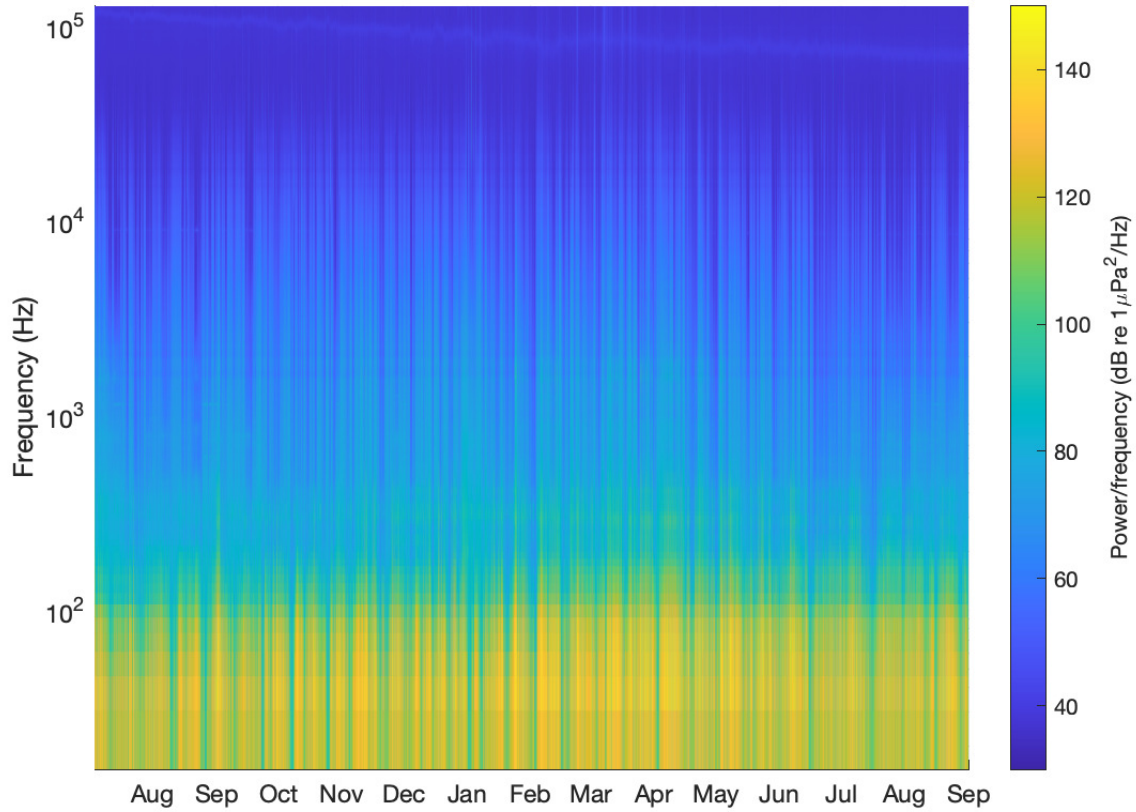
Figure 5.10: Noise levels as a function of frequency from July 2019 to September 2020.

Noise levels sorted as a function of increasing current speed for the period where observations were available, from July 2019 to November 2019, are presented in figure 5.11. The results in figure 5.11 demonstrate that the sorting method is not as effective for the 2019 data as it was for the 2017-2018 data. The resulting data improvement, shown in figure 5.12, is limited. Noise levels are sorted with current speed up to November 2019, the time period where current measurements are available.
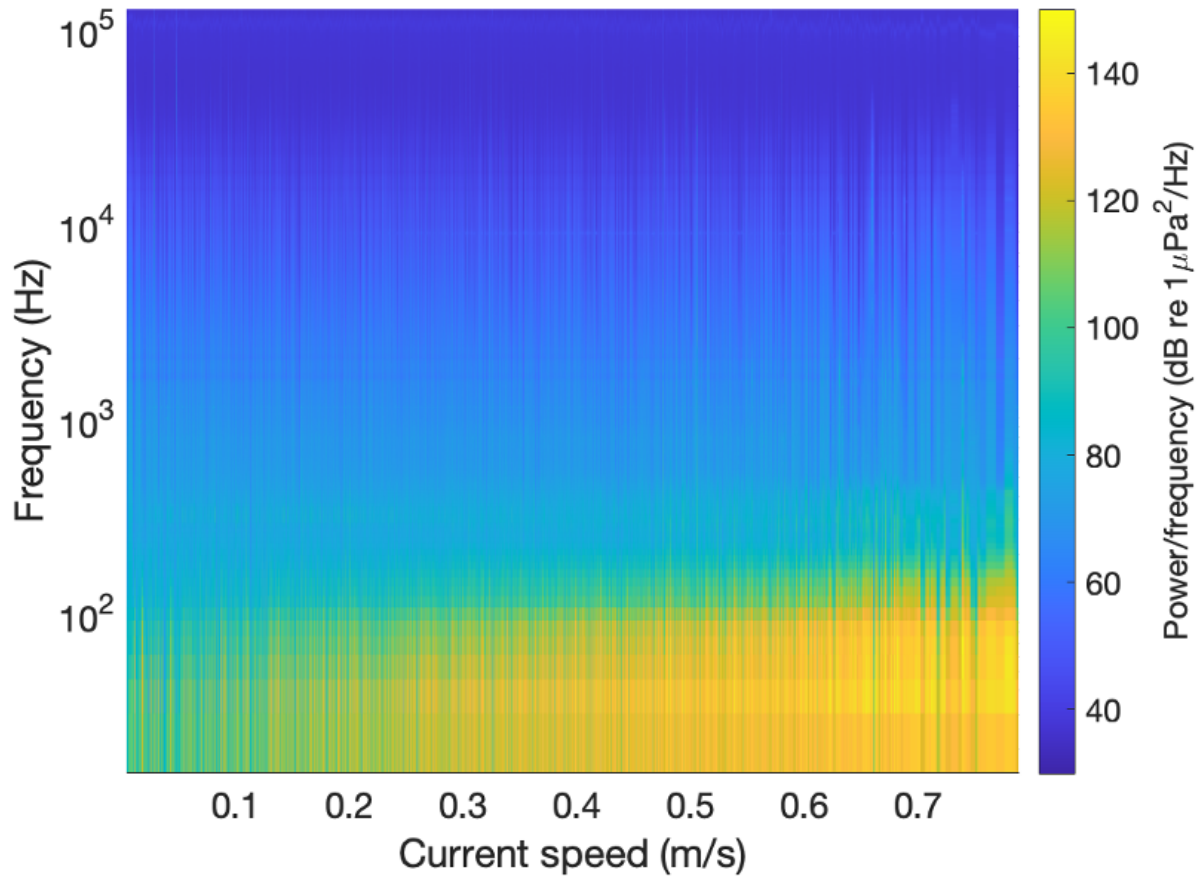
Figure 5.11: Noise levels as a function of frequency from July 2019 to November 2019 sorted as a function of increasing current speed.
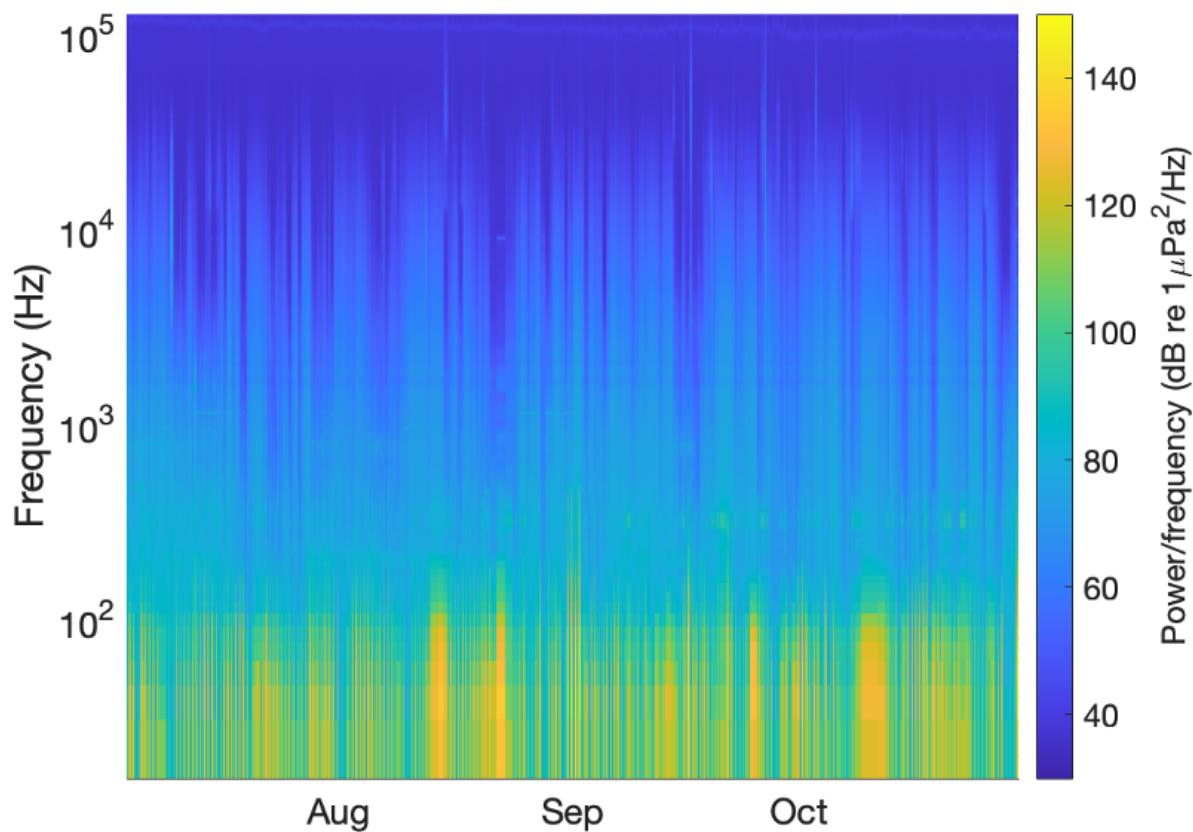
Figure 5.12: Noise levels as a function of frequency from July 2019 to November 2019 when corresponding current speeds were less than 0.2 m/s.

Acoustic recordings made from November 2019 to September 2020 were sorted according to current speed using the tidal predictions presented in section 5.2 and are shown in figure 5.13. Noise levels as a function of current speed for July 2019 to November 2019 are shown in figure 5.14 and correspond to a time period where speed observations were available. Current speeds are limited to 0.55 m/s for comparison with figure 5.13. In contrast to the data sorted with current speed measurements in figure 5.11, the sorting method using tidal predictions is not as effective. Nevertheless, the sorting method was applied in order to assess if data quality is improved. In the case of figure 5.13 no clear increase in low frequency power is observed with increasing current speed until perhaps when currents reach 0.5 m/s, where high power levels at low frequency may be slightly increased.
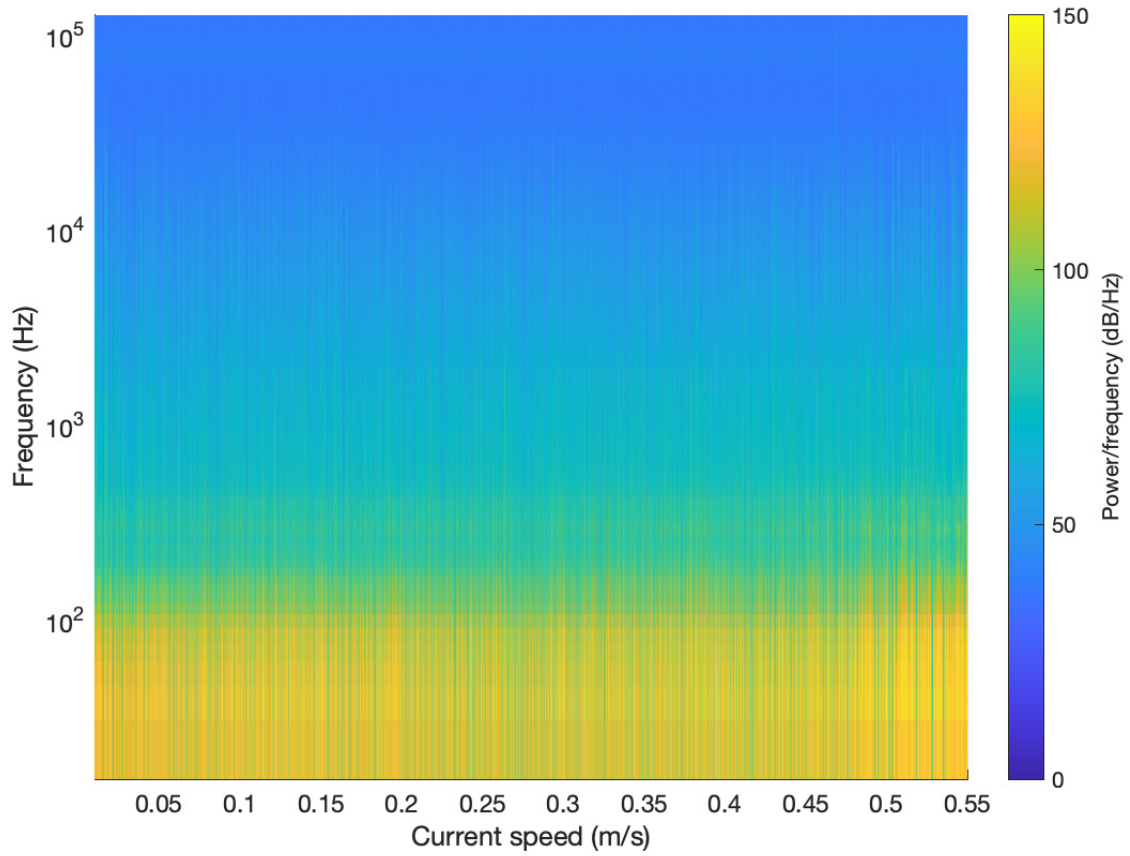
Figure 5.13: Noise levels as a function of frequency from November 2019 to September 2020 sorted with increasing current speed using current tidal predictions.
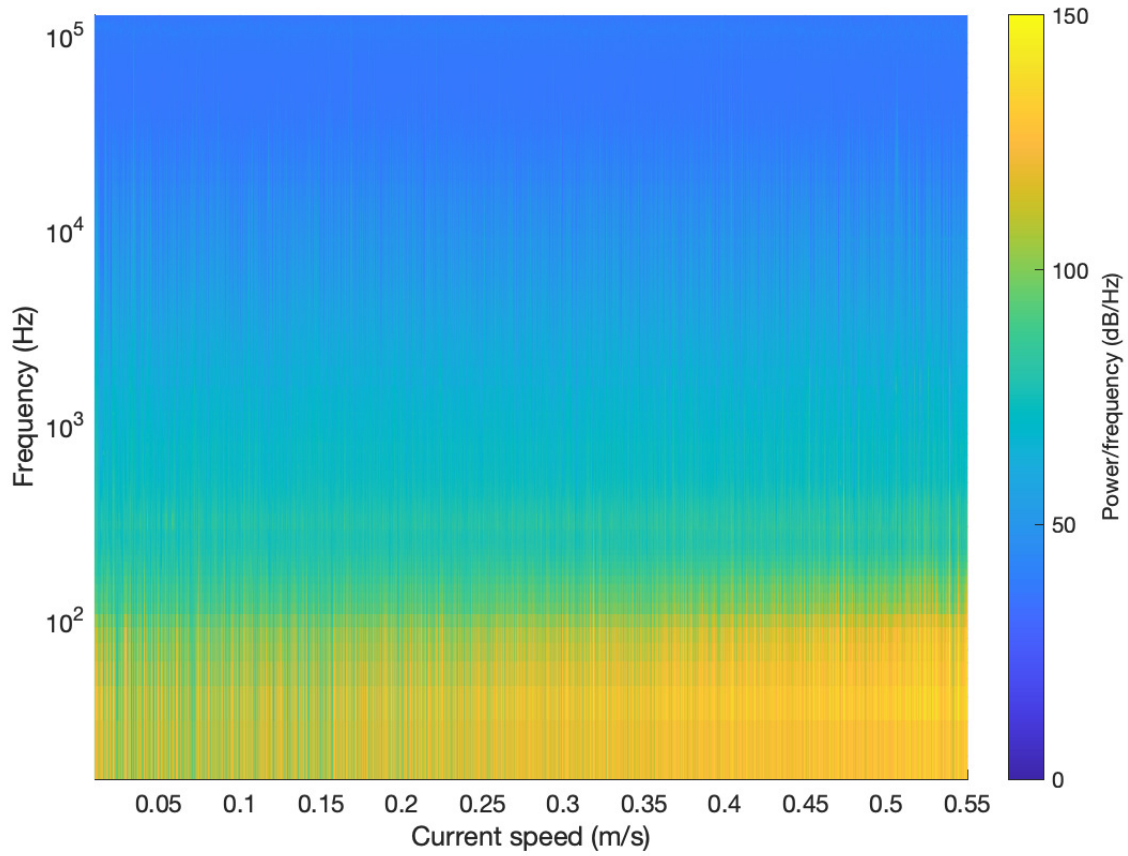
Figure 5.14: Noise levels as a function of frequency from July 2019 to November 2019 sorted with increasing current speed. Corresponding current speeds are restricted to less than 0.55 m/s for comparison with figure 5.13

5.4 Weather Classification

The weather classification algorithm, as presented in section 3.3.1, is applied in the following sections. Once the mooring noise signature is removed, it is possible to observe natural background noise signals caused by wind and rain. Shipping, rain, drizzle and bubble noise is identified for the entire data set and the reduced data set, as defined with the current speed threshold of 0.2 m/s.

5.4.1 Shipping noise

Shipping noise is identified according to equation 3.42, by marking periods when low frequency noise is disproportionately present. Two hour averages of the sound pressure level at 20 kHz is compared to the sound pressure level at 4 kHz in figures 5.15 and 5.16 from October 2017 to March 2018 and from July 2019 to September 2020, respectively. The data presented in figure 5.16, which corresponds to periods when ships are known to have been within 100km of the mooring location, is used to validate the shipping noise classification. All data where ships are present are successfully flagged which supports the accuracy of the algorithm. In figure 5.16, times where ships are known to be present are identified by the shipping noise algorithm and removed in the reduced data set. Shipping noise is identified in 15% and 20% of the data in figure 5.15 and in 22% and 24% of the data in figure 5.16. The flagged shipping noise may be attributed to mooring noise as shipping activity is low in this area.
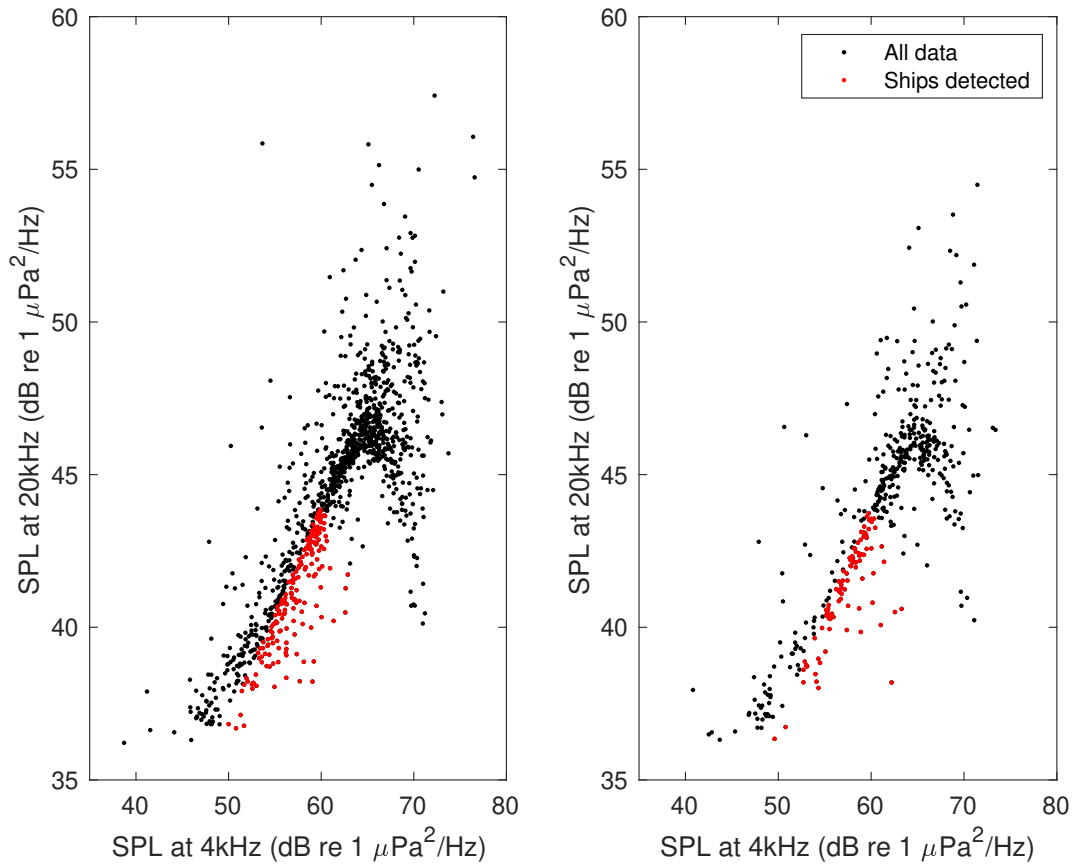
Figure 5.15: Sound pressure level at 20 kHz versus sound pressure level at 4 kHz from October 2017 to March 2018. Shipping noise indicated as red points. Left and right panels present the complete and reduced data sets, respectively.
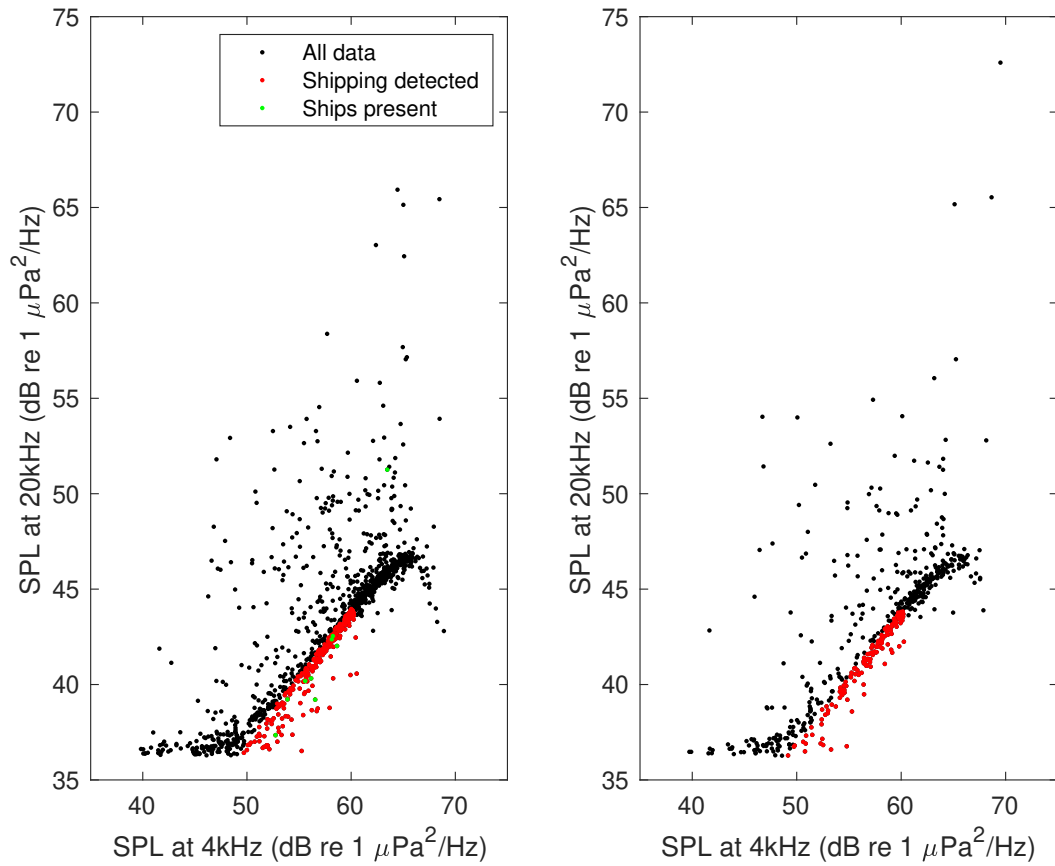
Figure 5.16: Sound pressure level at 20 kHz versus sound pressure level at 4 kHz from July 2019 to September 2020. Shipping noise indicated as red points. Points where ships are within 100km of the mooring location are shown in green. Left and right panels present the complete and reduced data sets, respectively.

5.4.2 Rain

Rain noise is detected using equation 3.43 by identifying periods where anomalously high levels of high frequency noise is associated with heavy rain. The sound pressure level at 20 kHz versus the sound pressure level at 5 kHz is presented in figure 5.17 for October 2017 to March 2018 and in figure 5.18 for July 2019 to September 2020. Sound pressure level is averaged every 2 hours to obtain these results. Rain events represent approximately 13% and 10% of the data points in figure 5.17 and represent 9% and 8% in figure 5.18.
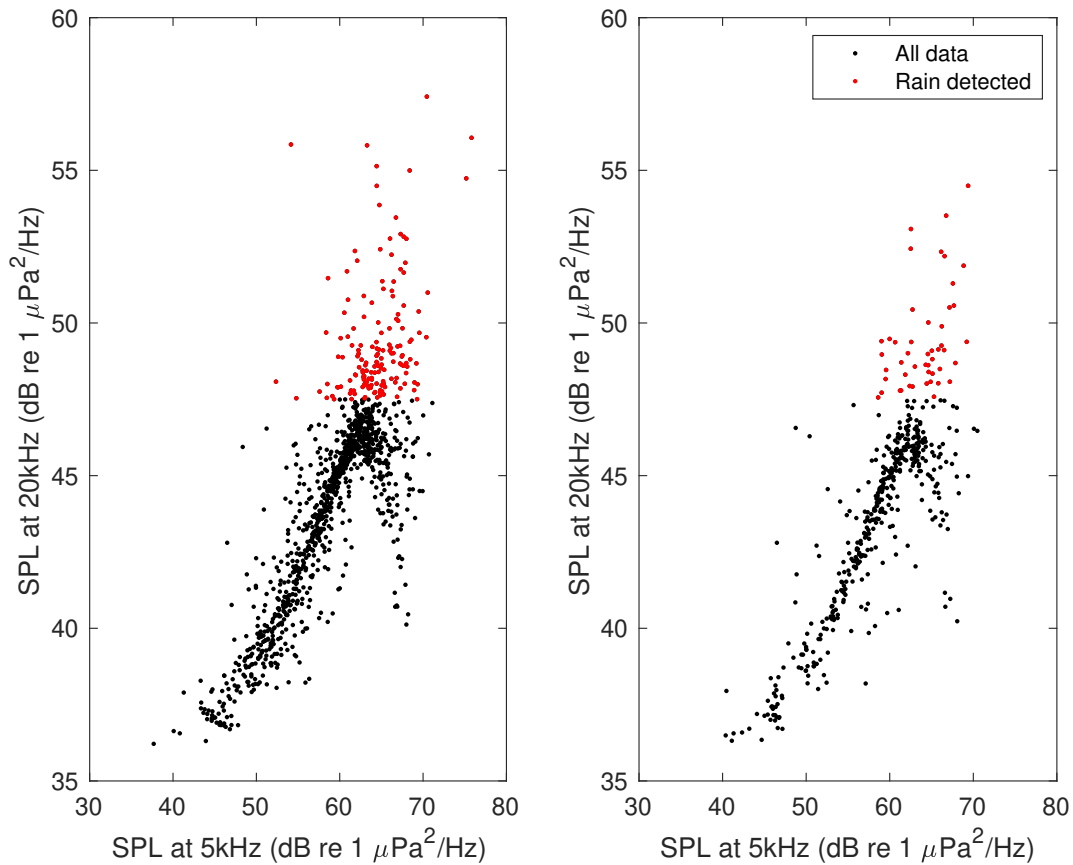
Figure 5.17: Sound pressure level at 20 kHz versus sound pressure level at 5 kHz from October 2017 to March 2018. Rain noise indicated as red points. Data points correspond to two hour averages of sound pressure level. Left and right panels present the complete and reduced data sets, respectively.
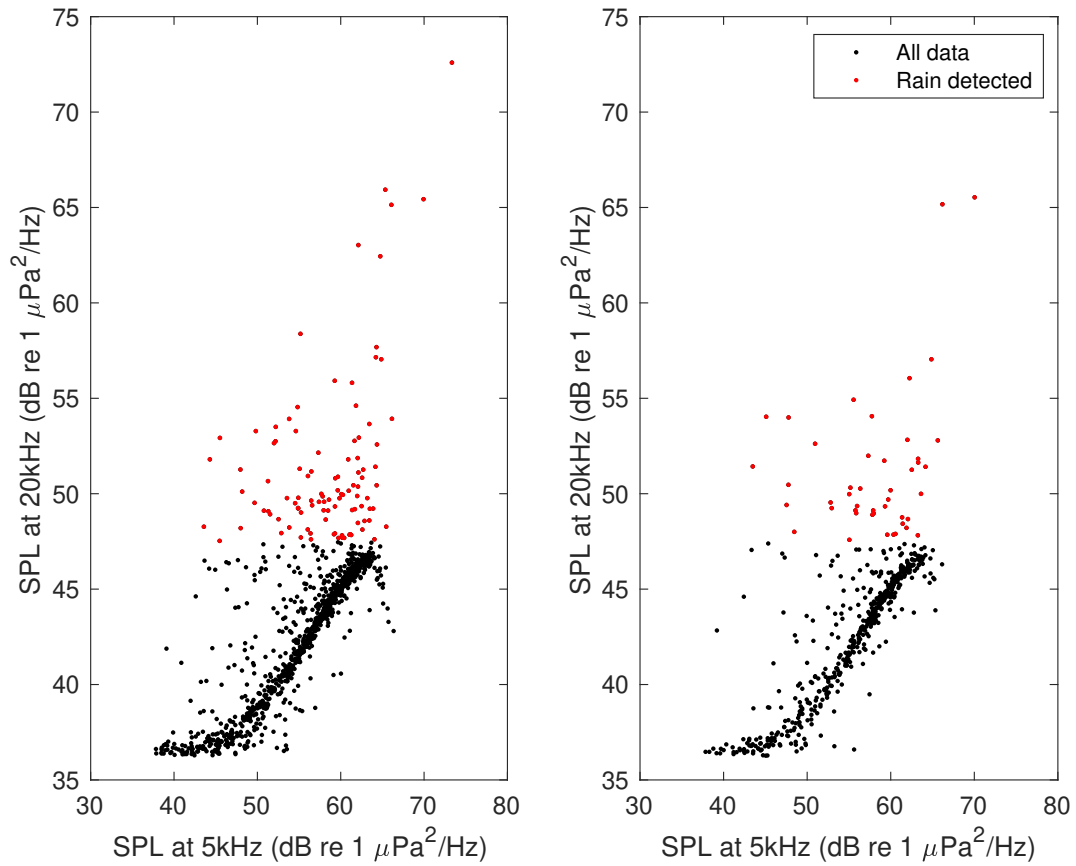
Figure 5.18: Sound pressure level at 20 kHz versus sound pressure level at 5 kHz from July 2019 to September 2020. Rain noise indicated as red points. Left and right panels present the complete and reduced data sets, respectively.

5.4.3 Drizzle

Equation 3.45 is used to identify drizzle events by detecting high levels of sound at intermediate frequencies of around 20 kHz. The results are shown in figures 5.19 and 5.20. Two hourly averages of the sound pressure level at 20 kHz is compared to that at 8 kHz for October 2017 to March 2018 and for July 2019 to September 2020. In figure 5.19, drizzle events account for 6% and 5% whereas in figure 5.20 they account for 23% and 21% of the total data. When noise levels are low, drizzle detection is not accurate, as seen below an SPL of 40 db at 8 kHz in figures 5.19 and 5.20.
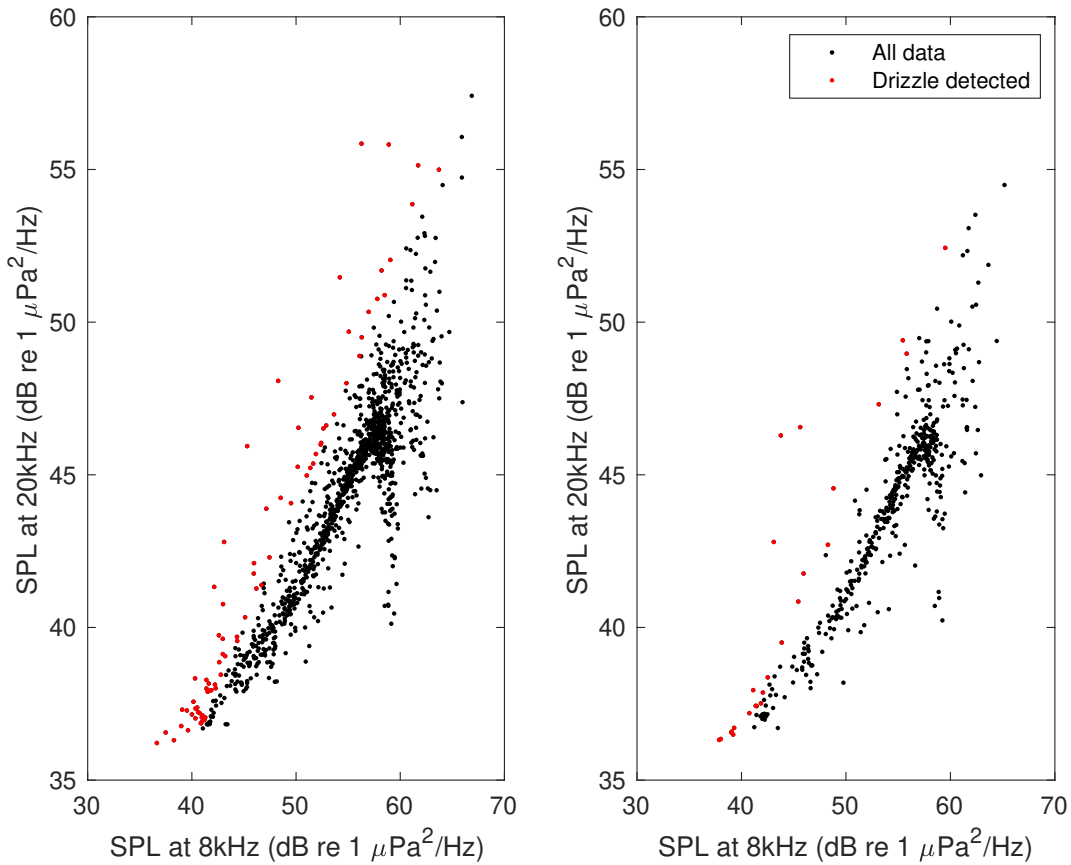
Figure 5.19: Sound pressure level at 20 kHz versus sound pressure level at 8 kHz from October 2017 to March 2018. Drizzle noise indicated as red points. Left and right panels present the complete and reduced data sets, respectively. Drizzle detection is not accurate below an SPL of 40 db at 8 kHz.
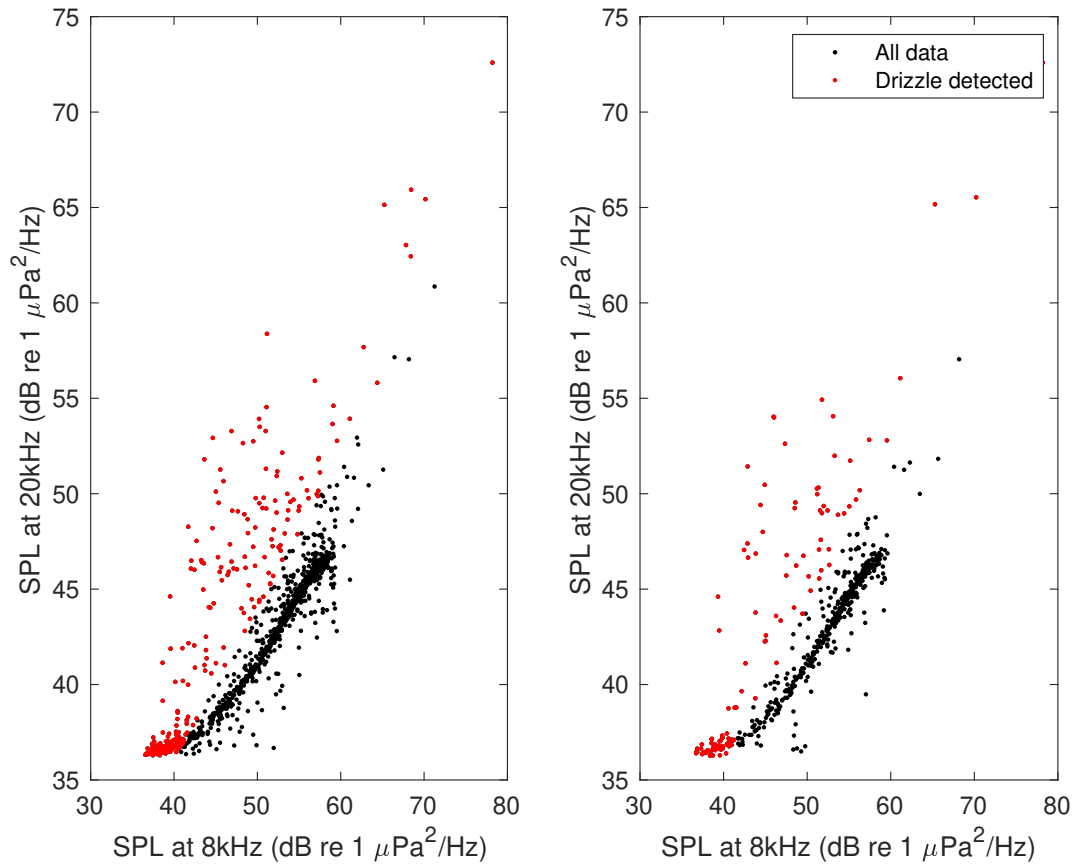
Figure 5.20: Sound pressure level at 20 kHz versus sound pressure level at 8 kHz from July 2019 to September 2020. Drizzle noise indicated as red points. Left and right panels present the complete and reduced data sets, respectively. Drizzle detection is not accurate below an SPL of 40 db at 8 kHz.

5.4.4 Bubbles

The presence of bubbles in the water column is identified using equation 3.46 where changes in noise levels due to sound absorption by bubbles is detected. The sound pressure level at 25 kHz versus the sound pressure level at 5 kHz is presented in figure 5.21 for October 2017 to March 2018 and in figure 5.22 for July 2019 to September 2020. Sound pressure level is averaged every 2 hours to obtain these results. Bubbles are detected in 49% and 51% of the total data in figure 5.21 and in 34% and 35% of the data in figure 5.22
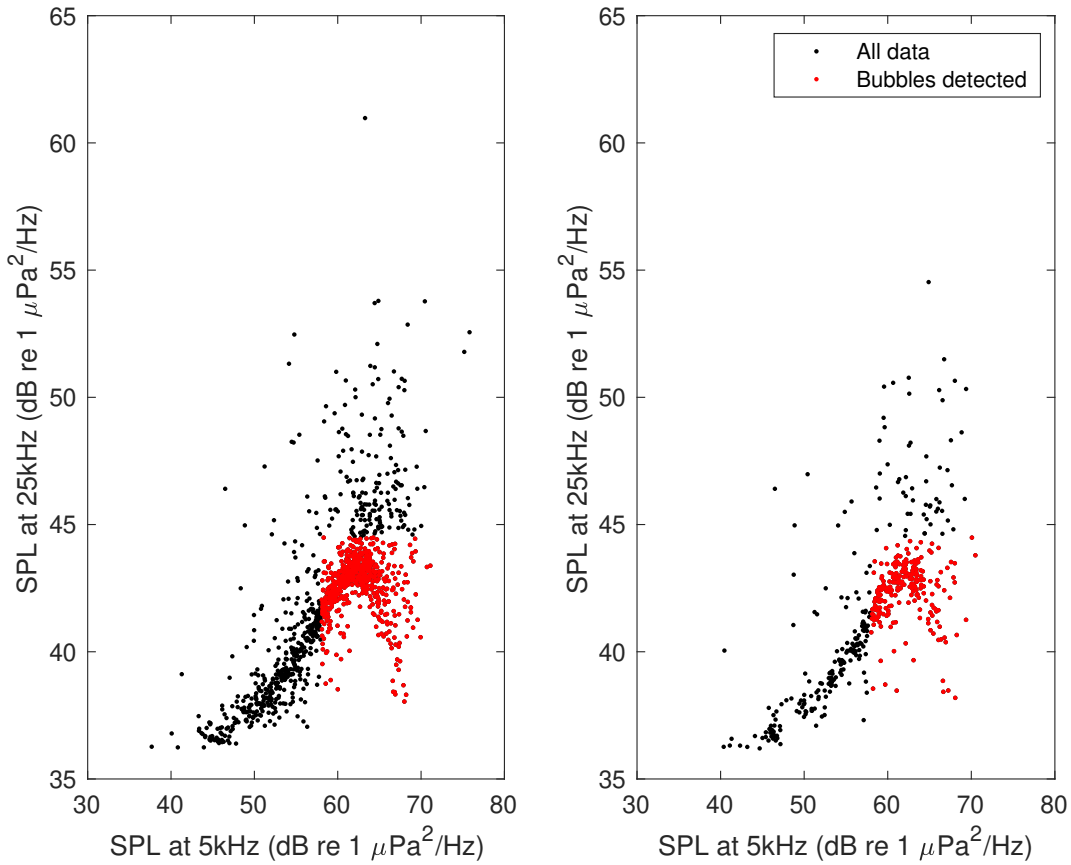
Figure 5.21: Sound pressure level at 25 kHz versus sound pressure level at 5 kHz from October 2017 to March 2018. Bubble noise indicated as red points. Left and right panels present the complete and reduced data sets, respectively.
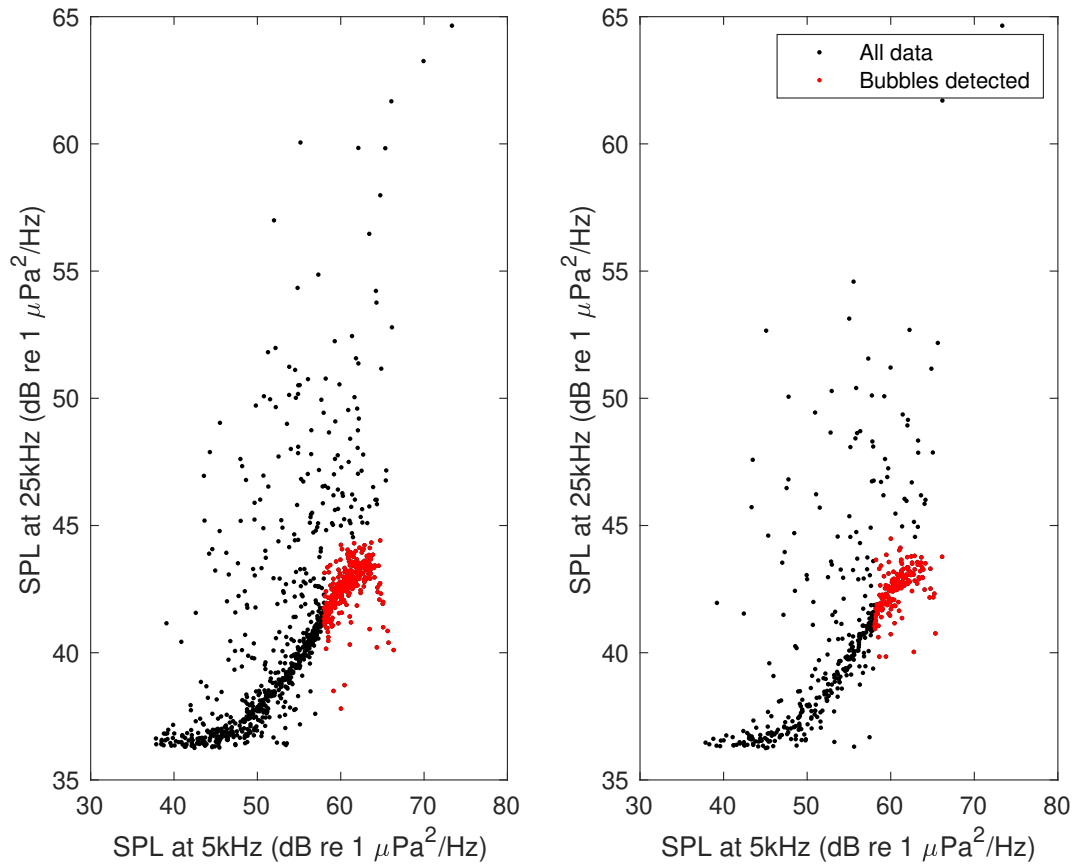
Figure 5.22: Sound pressure level at 25 kHz versus sound pressure level at 5 kHz from July 2019 to September 2020. Bubble noise indicated as red points. Left and right panels present the complete and reduced data sets, respectively.

5.5 Weather algorithms

5.5.1 Wind speed

The wind speed algorithm presented in section 3.3.1 was applied to noise levels recorded from October 2017 to March 2018 and from July 2019 to September 2020. The results are shown in figures 5.23 and 5.25. The wind speed estimates are compared to values according to the Global Deterministic Prediction System (GDPS) model. The GDPS model predicts atmospheric variables including temperature, wind speed and direction, cloud cover and precipitation. The model values are used as a comparison in order to evaluate the accuracy of the wind speed estimates. Although the calculated wind speeds tend to be larger than the GDPS model values, overall good agreement is observed between the estimates and the model values. The difference of the model values and the estimates are presented in figures 5.24 and 5.26. The average values for both October 2017 to March 2018 and for July 2019 to September 2020 are approximately -3. From October 2017 to March 2018 the difference value reaches a maximum value of nearly 25 m/s, although most values are within 10 m/s of each other. Similarly, from July 2019 to September 2020 the maximum difference values are near 20 m/s and most differences are within 10 m/s.
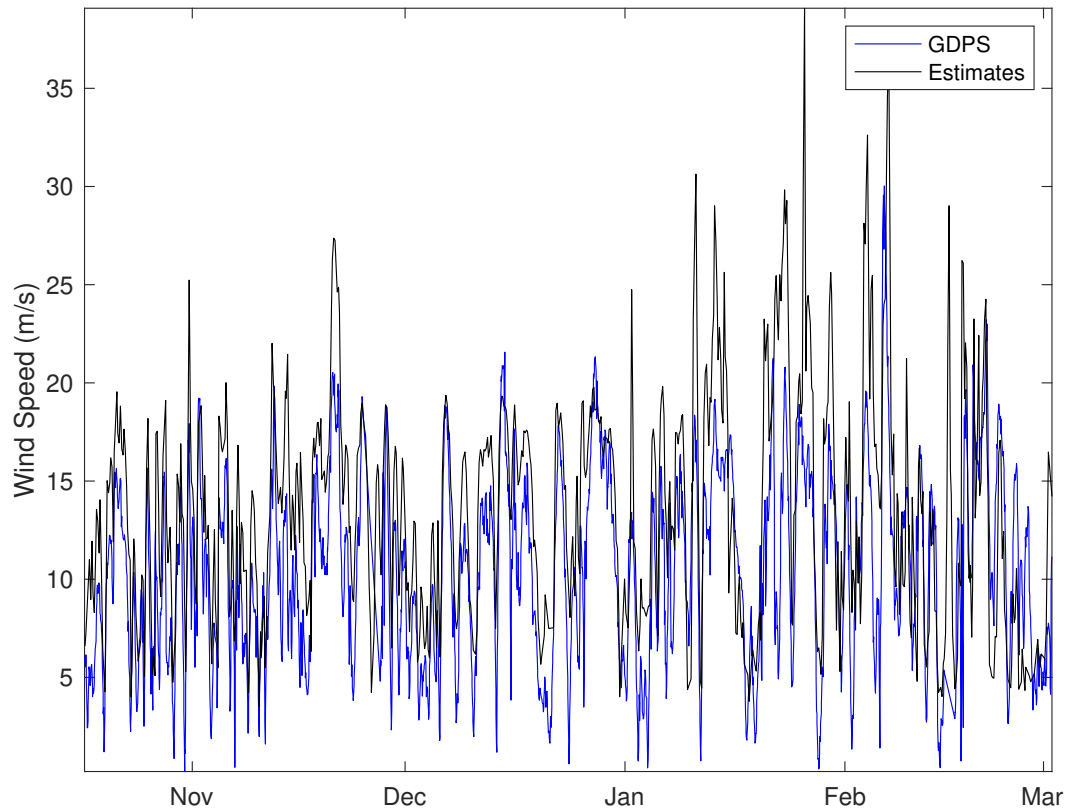
Figure 5.23: Wind speed estimates obtained using the WOTAN wind speed algorithm, shown in black. GDPS wind speed model values are shown in blue for comparison. Wind speeds calculated from October 2017 to March 2018.
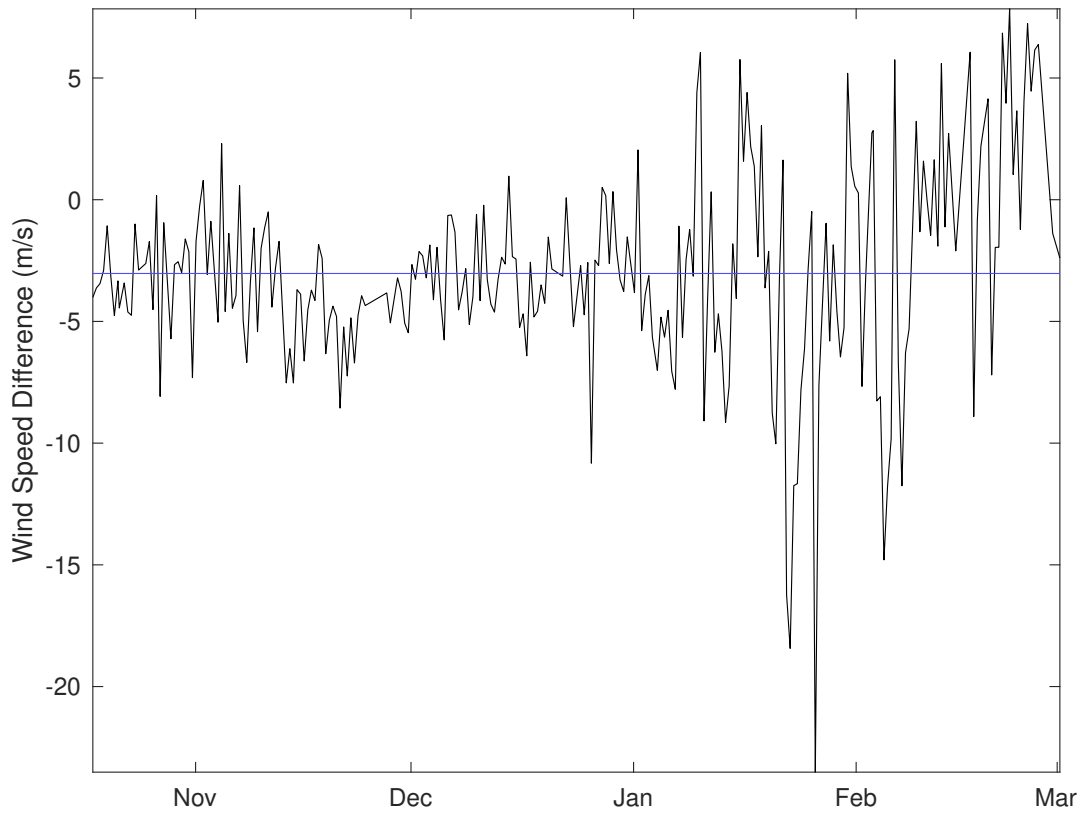
Figure 5.24: Wind speed difference between GDPS model values and estimates from October 2017 to March 2018. Average difference of -3.0 m/s shown as horizontal blue line.
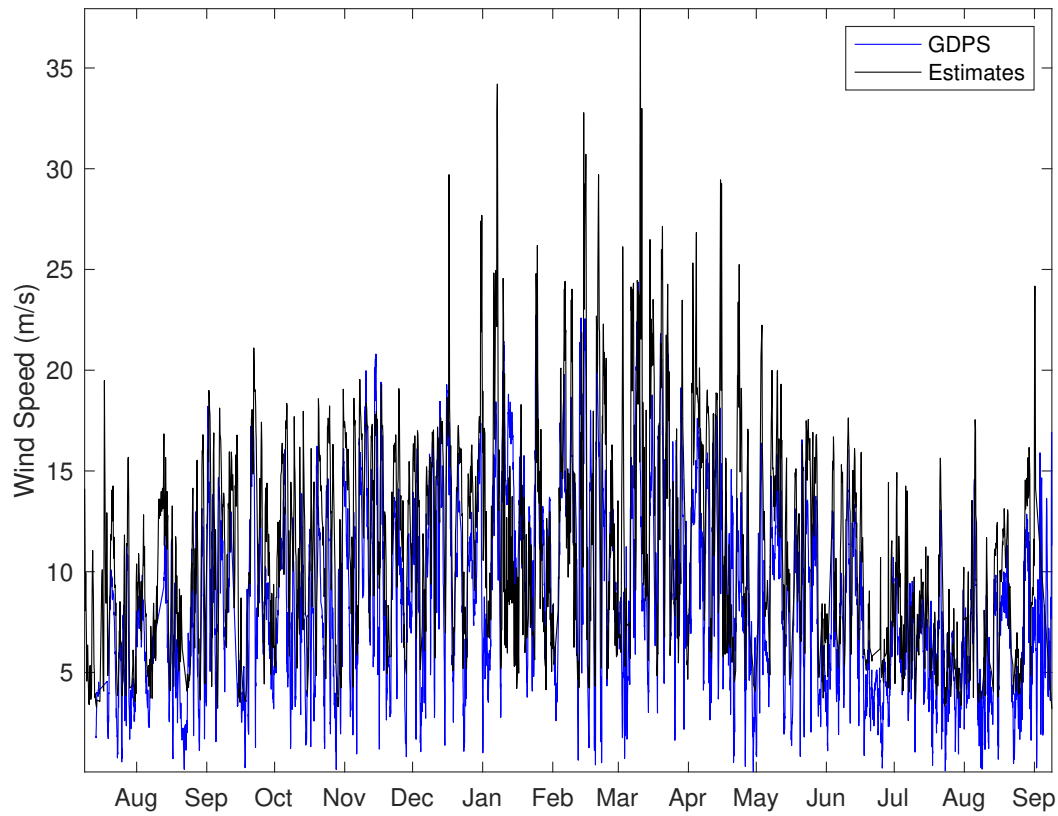
Figure 5.25: Wind speed estimates obtained using the WOTAN wind speed algorithm, shown in black. GDPS wind speed model values are shown in blue for comparison. Wind speeds calculated from July 2019 to September 2020.
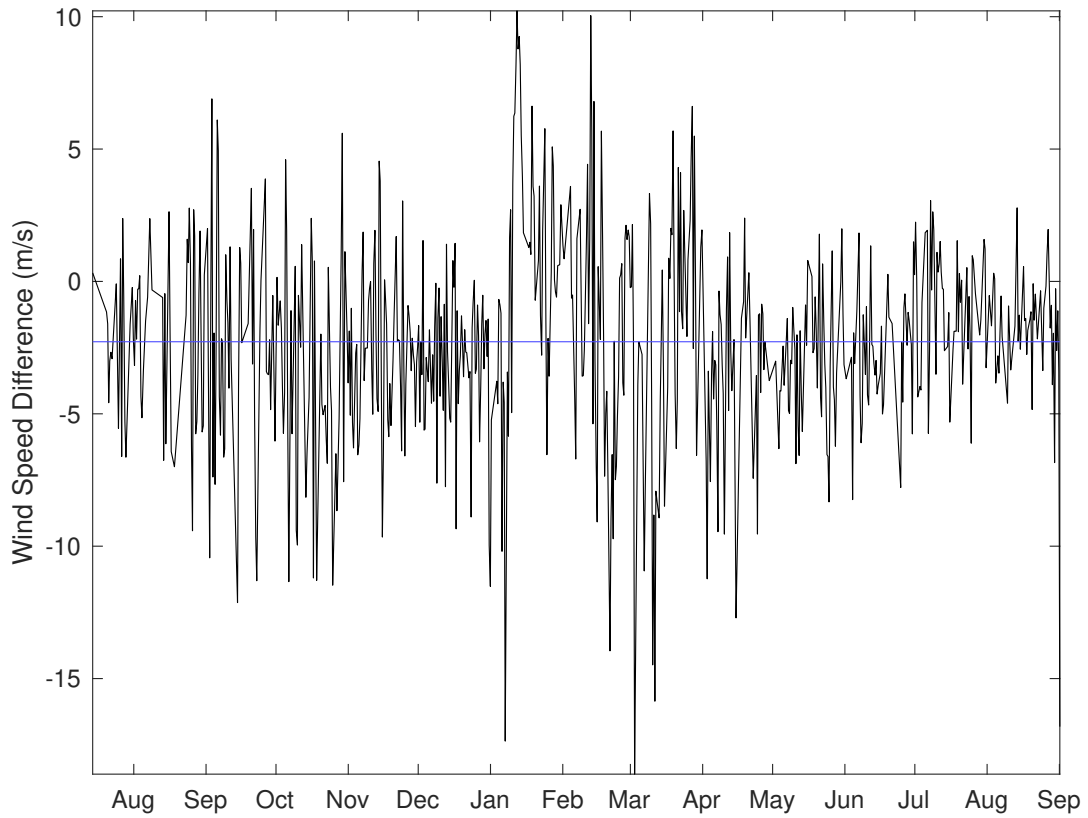
Figure 5.26: Wind speed difference between GDPS model values and estimates from July 2019 to September 2020. Average difference of -2.3 m/s shown as horizontal blue line.

5.5.2 Rainfall rate

Rainfall rates are calculated using the algorithm presented in section 3.3.2 and are shown in figures 5.27 and 5.29 for October 2017 to March 2018 and for July 2019 to September 2020, respectively. GDPS model values for quantity of precipitation are converted to precipitation rate and are then compared to the estimated values. Over some time periods, the estimates appear to align with the GDPS model values. The difference between the model values and the estimates is presented in figure 5.28 for 2017-2018 and in figure 5.30 for 2019-2020. In 2017-2018 a maximum of 12 mm/hr is observed and many difference values reach values near 5 mm/hr. The result is similar for the 2019-2020 data, where difference values reach a maximum of 15 mm/hr. Overall, the estimates and the model values do not show good agreement. Some error may be attributed to gaps in the model data.
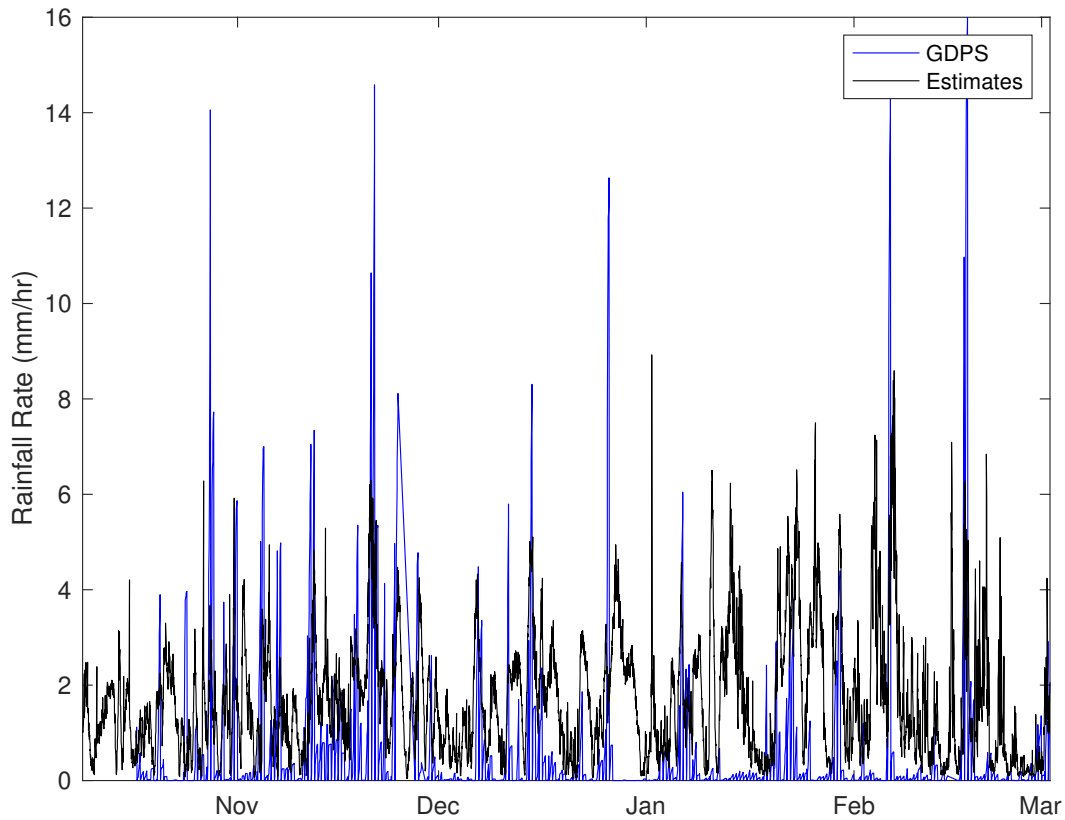
Figure 5.27: Rainfall rate estimates shown in black. GDPS rainfall rate model values are shown in blue for comparison. Rainfall rates calculated from October 2017 to March 2018.
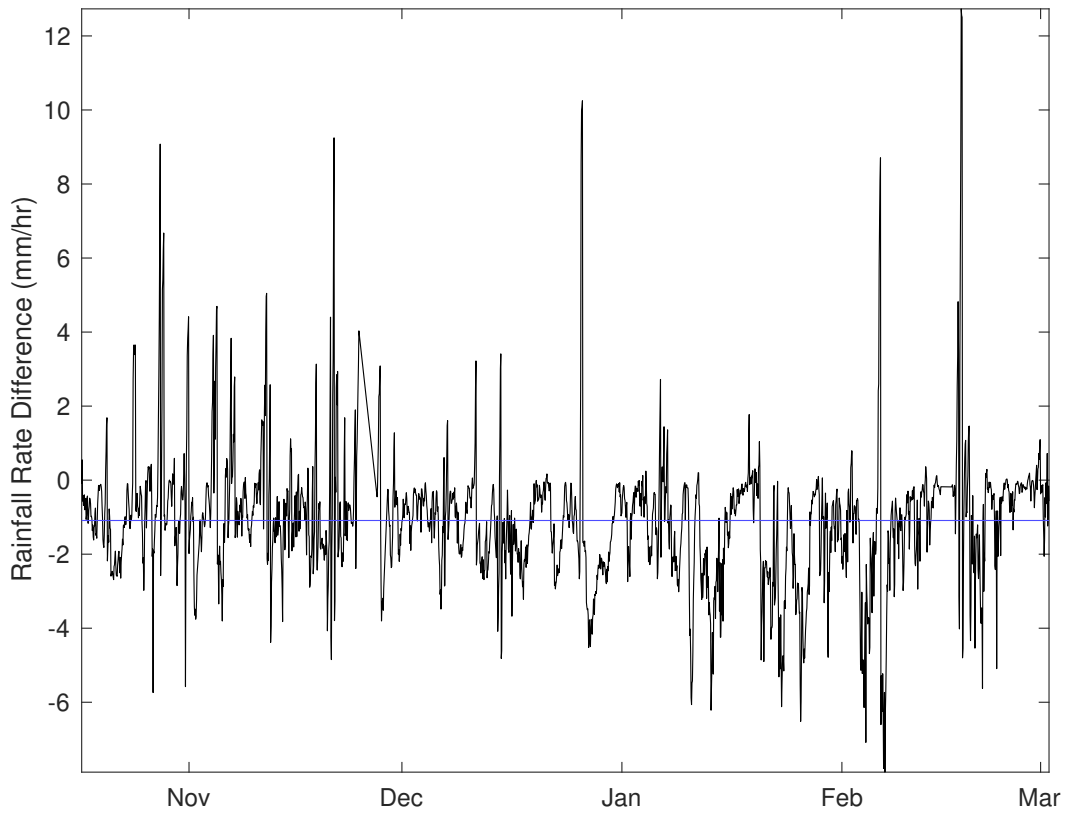
Figure 5.28: Rainfall rate difference between GDPS model values and estimates from October 2017 to March 2018. Average difference 0f -1.1 mm/hr shown as horizontal blue line.
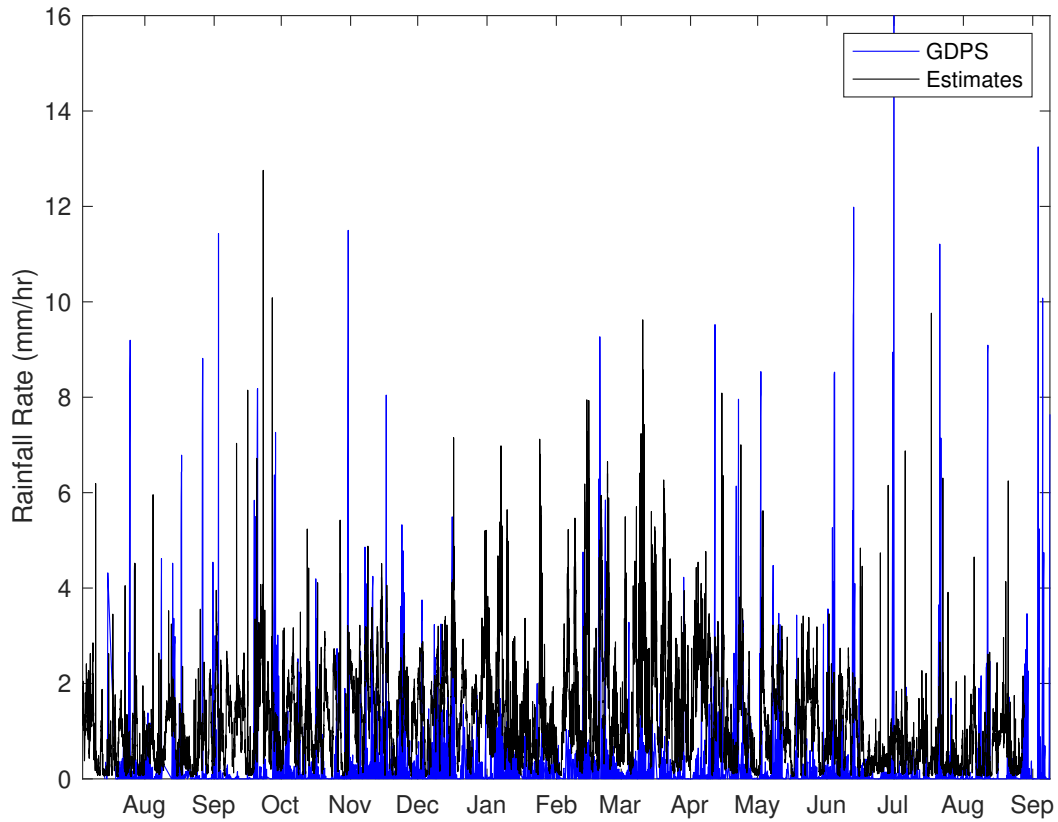
Figure 5.29: Rainfall rate estimates shown in black. GDPS rainfall rate model values are shown in blue for comparison. Rainfall rates calculated from July 2019 to September 2020.
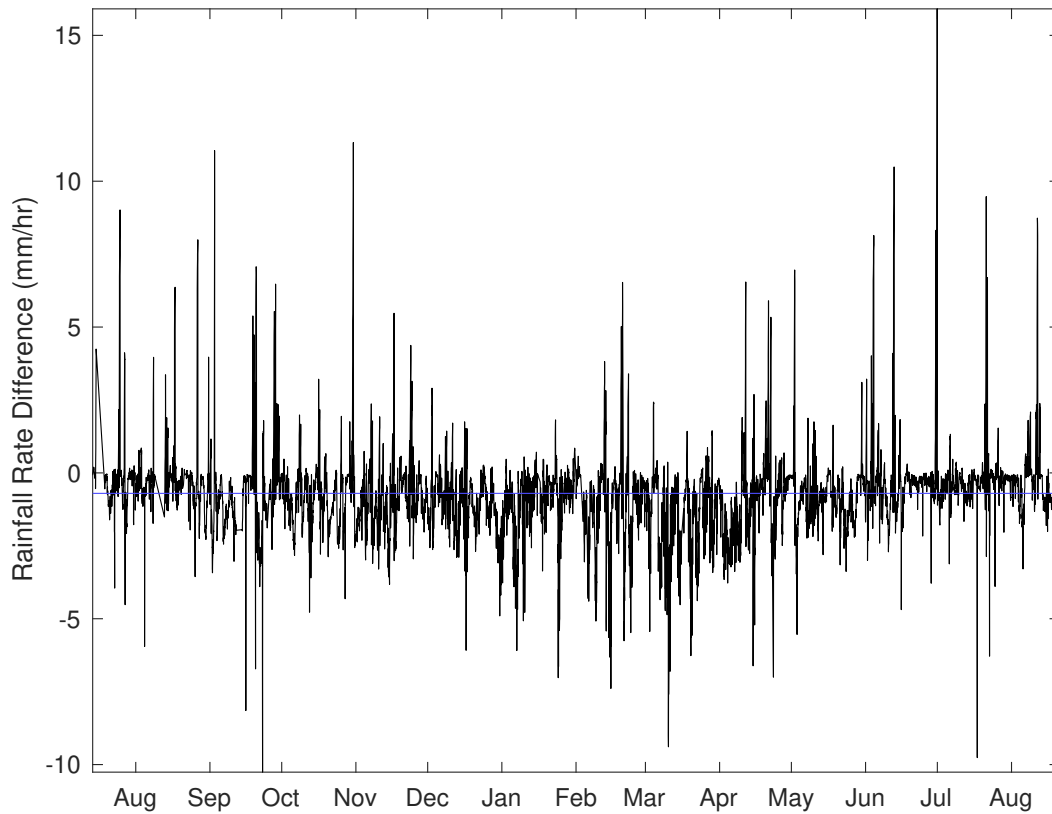
Figure 5.30: Rainfall rate difference between GDPS model values and estimates from July 2019 to September 2020. Average difference of -0.7 mm/hr shown as horizontal blue line.

5.5.3 Bottom interaction model

As sound originating at the surface propagates through the water column it may interact with the ocean bottom or surface and be reflected. Therefore, surface and bottom reflections are detected in addition to the direct sound wave and thus, act to increase the overall noise level. If not corrected, reflections will cause weather estimates to be inaccurate. Further, sound may be absorbed at the surface and bottom as it interacts with the sediment layer. High frequency attenuation is attributed to acoustic absorption in the water column. As the reflected signal travels a greater distance than a directly received wave, more absorption will occur.

The spectrum of surface noise received by an instrument at a depth of 500m is shown in figure 5.31. The effect of the bottom interaction model for a bottom loss of -5 dB is presented for ocean floor depths of 510m, 700m, 1400m and 1800m. At both high and low frequencies, the depth of the bottom does not appear to be important. This is expected due to minimal absorption occurring at low frequencies and due to high frequency signals being directly received by the instrument [1]. Most of the variation with bottom depth occurs at intermediate frequencies. Figure 5.31 also suggests that at low frequencies, the response may be affected by nearly 3 dB in all instances. Therefore, as a result of bottom reflections and absorption, the sound spectrum may be increased at low frequencies and decreased at high frequencies, respectively.

In the current experiment, the instrument is located at 500m depth and approximately 10m above the ocean floor, which corresponds to the blue curve in figure 5.31. The wind speed algorithm is a function of the sound spectrum at 8 kHz and a 1.75 dB response is observed at this frequency. The effect of this response on the wind speed estimates is presented in figure 5.32. A 1.75 dB change in spectrum level results will cause the wind speed to increase by nearly 3 m/s at wind speeds of around 15 m/s. This resulting sensitivity is high and thus, the bottom interaction model is not applied to the wind speed calculation.
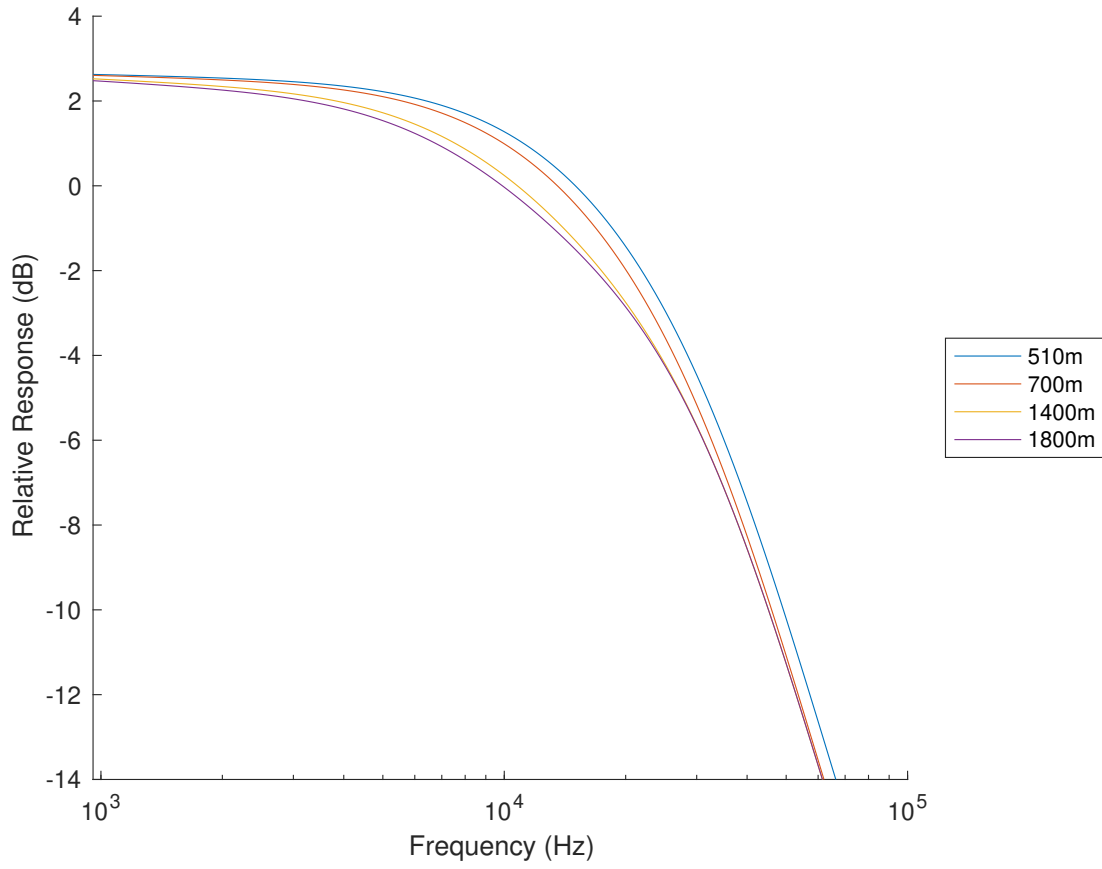
Figure 5.31: Spectrum for instrument depth of 500m and bottom depth of 510m, 700m, 1400m and 1800m with a bottom loss of -5 dB.
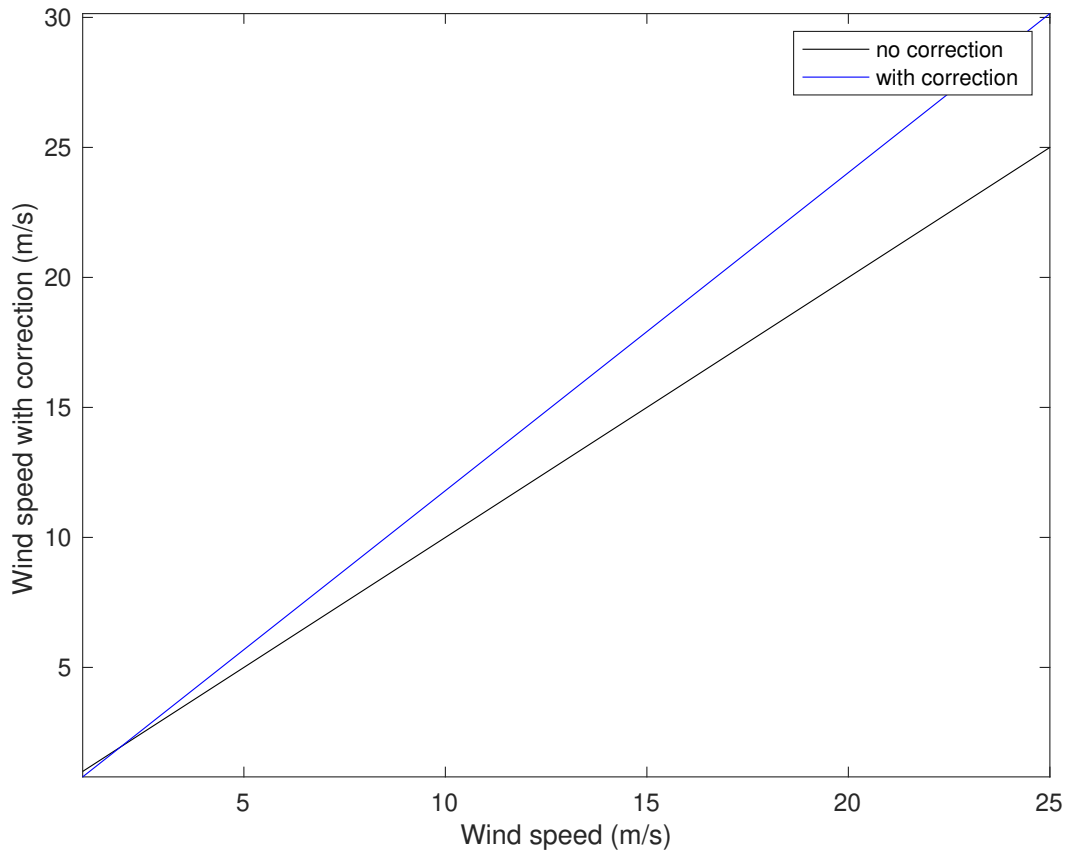
Figure 5.32: Effect of bottom interaction on wind speed estimate. Wind speeds calculated with and without correction shown in blue and black, respectively.

Chapter 6

Discussion

The objective of this work was to observe naturally occurring noise levels in a high biodiversity area without contamination by anthropogenic sources. The Saglek bank location sees minimal shipping and is thus an ideal location for this study. The predominant issues at this location were caused by high current speeds at depth. High current speeds led to the mooring being significantly tilted such that depth cell mapping was necessary to ensure accurate current velocity measurements. In addition, noise contamination occurred as the mooring itself made noise in the presence of such strong currents. This noise contamination thus impacted natural ambient noise recordings.

A method to eliminate the mooring noise was employed. Due to the mooring noise being strongly associated with current speed, we attempted to remove this noise contamination by sorting the noise levels as a function of increasing current speed. Next, a speed threshold was selected, below which the mooring noise is not observed. A reduced data set was recovered below the speed threshold of 0.2 m/s and represents naturally occurring ambient noise levels. Considering that no other naturally occurring ocean noise sources are strongly linked to current velocity, this procedure should provide an unbiased method to remove the mooring noise contamination. The sorting method yields significant data improvement for the data collected between October 2017 to March 2018.

In contrast, the data improvement is limited for observations made from July 2019 to November 2019 and the sorting method does not appear to account for all instances of high power at low frequencies. This data segment contains more noise which is not directly linked to current speed. Further, the sorting method is applied using tidal predictions up to September 2020. The sorting method is not effective with the tidal estimates which only account for tidal variations of the current speed. As observed in the current

speed measurements, non-tidal variations tend to reach approximately 0.2 m/s. The slower current speeds presented in the sorting method are near this value and thus, the estimates do not accurately reflect the tidal versus non-tidal origin of the current variations. However, as the current speed increases to near 0.5 m/s the sorting method appears to more accurately detect high power at low frequency. This results from faster currents being predominantly tidal in origin and the noise contamination being more strongly associated with these high current speed.

The current speed tidal estimates were also used as support for an ROV dive. During ROV dives, current speed measurements were made and may be used to validate the tidal estimates. The measurements and estimates show good agreement although, some error is observed. The error may be caused by a small time delay or simply a result of non-tidal variations not being included in the estimates.

The weather classification algorithm was applied to identify periods where noise resulted from shipping activity, rain, drizzle or where bubbles altered noise levels. First, ships are detected when low frequency noise levels dominate higher frequencies. The algorithm detects 5% more shipping noise in the reduced data set compared the entire data set in 2017-2018 and 2% more shipping noise in the reduced data set in 2019-2020. During this time, there were only 5 ships in transit indicating that the noise identified as shipping may be a result of mooring noise. In the case of noise levels from July 2019 to September 2020, time periods where ships are known to be present are correctly identified by the algorithm and removed in the reduced data set. Ship noise flagged by the algorithm at times where no ships are present may be attributed to the mooring noise. Next, noise resulting from rain was identified for both time periods. In either case, rain noise detected by the algorithm is diminished in the reduced data set. Similarly, drizzle events are decreased by 1% and 2% in the reduced data sets. In addition, bubbles are detected in a significant percentage of the data for both time periods. Namely, bubbles account for approximately 50% of the 2017-2018 data for both the full and reduced data sets. For the 2019-2020 data, bubbles represent around 35% for either data set. Bubbles are known to affect the underwater noise spectra caused by wind and rain and thus, may be a source of error in the presented weather estimates.

The wind speed estimates calculated using the WOTAN wind speed algorithm were compared to the GDPS model values. The comparison suggests the algorithm was successful, as the estimates and model values appear to align adequately such that increasing or decreasing trends occur in both the estimates and model values at the same time. However, for both the 2017-2018 and the 2019-2020 data the estimates tend to be larger than the model values. For 2017-2018 the maximum difference is nearly 25 m/s, although this value appears to be an outlier. The majority of the difference values are within 10 m/s. The maximum

74

difference for 2019-2020 is approximately 20 m/s, where most variations are also within 10 m/s. In contrast, the rainfall rate algorithm is not as successful. The calculated values overestimate the model values over most of the time periods. The difference in the model values and estimates exceed 8 mm/hr over both time periods and reach 4 and 5 mm/hr in many instances. This may be in part due to the spatial averaging involved in the GDPS model values as they are obtained from a 1 degree latitudinal and longitudinal grid. Further, some wind contamination is likely present in the flagged spectra of rainfall events. For increasingly fast wind speeds, larger rainfall rates are needed to obtain accurate estimates. Therefore, it may be beneficial to first identify wind speed and determine rainfall rate below some predetermined wind speed threshold. Lastly, the bottom correction model as presented in Kanachi [1], is not applied to the wind speed algorithm as the sensitivity of the model is considerably high with increasing wind speed. In the current experiment, the instrument is positioned near the bottom at 500m depth, corresponding to a relatively small difference of 1.75 dB and thus, bottom and surface reflections do not have a significant effect on ambient noise levels. It is likely that the assumption of total reflection from the surface is not realised at high frequencies which would further reduce the signal enhancement and make the correction less important.

Overall, it appears that the proposed sorting method may be used in some instances in order to observe naturally occurring noise levels in the presence of high current speeds. In particular, it appears that good quality current measurements are needed as our use of tidal predictions did not provide adequate speed accuracy to predict mooring noise. In order to obtain improved results it may be beneficial to identify other sources of noise contamination which are not tidal in origin such as noise caused by turbulence. Once removed, the proposed method may be more successful in identifying noise contamination associated with tidally driven currents. Further investigation is required, as this method is not effective in all data sets. However, the importance of ambient noise observations in the absence of anthropogenic contamination is clear such that natural noise levels may be analyzed and accurate weather information can be extracted.

Appendix A

Acoustic Intensity

A.1 Introduction

The following appendix presents an internship project completed as part of the iMerit NSERC CREATE program. The iMerit program aims to facilitate collaborations to address challenges associated with ocean research and includes a professional development component, a field component, and an industry internship. Jasco Applied Sciences provided an internship opportunity for the work presented in the following sections.

A.2 PAGE method

Acoustic intensity is typically measured using finite difference methods, where the pressure gradient across microphones is measured and is used to calculate the intensity. The phase and amplitude gradient estimation (PAGE) method offers a solution to frequency dependent finite difference methods by separating the measured complex pressure into it's amplitude and phase [28]. The active and reactive intensities are written as shown in equations A.1 and A.2, respectively.

$$\vec{I_a} = \frac{1}{\omega \rho_0} P^2 \nabla \phi \tag{A.1}$$

$$\vec{I_r} = -\frac{1}{\omega \rho_0} P \nabla P \tag{A.2}$$

where ω is the angular frequency, ρ is the density of the medium, ϕ is the phase and P is the pressure at the center of hydrophone array. The PAGE method is based on estimates of the phase gradient and amplitude pressure gradient to estimate intensity. The gradient of the phase is determined by a least squares estimate as,

$$\nabla\phi = (X^T X)^{-1} X^T \delta\phi \tag{A.3}$$

where X is the matrix of pairwise separation vectors as rows as shown in equation A.4.

$$X = [r_2 - r_1 | r_3 - r_1 | \ldots | r_N - r_{N-1}]^T \tag{A.4}$$

The pairwise phase differences between microphones is defined as $\delta\phi$ which is given by the pairwise transfer functions,

$$\delta\phi = \begin{bmatrix} H_{12} \\ H_{13} \\ \vdots \\ H_{N-1,N} \end{bmatrix} \tag{A.5}$$

The pressure amplitude gradient is similarly determined by a least squares estimate where δP corresponds to the pairwise differences between measured pressure amplitudes, as shown in equations A.6 and A.7.

$$\nabla P = (X^T X)^{-1} X^T \delta P \tag{A.6}$$

$$\delta P = \begin{bmatrix} P_2 - P_1 \\ P_3 - P_1 \\ \vdots \\ P_N - P_{N-1} \end{bmatrix} \tag{A.7}$$

Finite difference methods are limited by an upper frequency limit which is determined by the microphone spacing [28]. The spatial Nyquist limit occurs when $kd = \pi$ where k is the wavenumber and d is the spacing between microphones. As kd approaches π, finite difference methods tend to underestimate the intensity, whereas the PAGE method does not [11], [28], [29]. In addition, the PAGE method allows for phase unwrapping such that the upper frequency limit can be extended [6], [11], [28]. When phases are

unwrapped, the frequency limit will be determined by the noise present in the phase differences in the argument of the transfer functions [28]. In this report, the PAGE method is applied in an oceanographic context to determine acoustic intensity as well as estimate the direction of noise sources.

A.2.1 Methods

The PAGE method is employed using hydrophone data for an oceanographic application. The pairwise hydrophone separation vectors are defined according to the hydrophone array geometry. The orthogonal and tetrahedron arrays used are shown in figures A.1 and A.2.
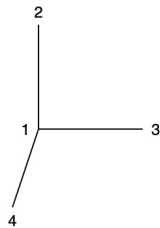
Figure A.1: Orthogonal hydrophone array geometry. x direction is to the right, y is upwards and z is towards the reader.
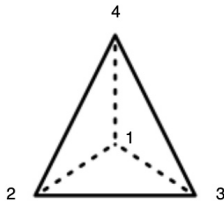
Figure A.2: Tetrahedron hydrophone array geometry. x direction is to the right, y is upwards and z is towards the reader.

The pressure at the center of the array, P in equations A.1 and A.2, depends on the array geometry. A comparison of methods to calculate the pressure at the center of arrays with various geometries has previously been reported [32][33]. The most accurate methods are determined from the following equations,

$$P_0 = (P_2 + P_3 + P_4 - P_1)/2 \tag{A.8}$$

$$P_0 = (P_1 + P_2 + P_3 + P_4)/4 \tag{A.9}$$

Equations A.8 and A.9 are used to estimate the pressure at the center of the orthogonal and tetrahedron array, respectively. The subscripts correspond to the hydrophone number shown in figures A.1 and A.2.

The phase difference between hydrophones is calculated using the cross spectrum between each hydrophone pair. The cross-correlation function between two random vectors x and y is defined as

$$R_{xy}(m) = E[x_{n+m}, y_n^*] = E[x_n, y_{n-m}^*], \tag{A.10}$$

where $E[.]$ is the expected value operator and $-\infty < n < \infty$. The cross power spectral density is then defined as

$$Power_{xy} = \sum_{m=-\infty}^{\infty} R_{xy}(m)e^{-jwm}. \tag{A.11}$$

The pairwise transfer function matrix (Eq. A.5) is determined using equation A.11.

Ensemble averaging is used to reduce the noise in the transfer functions. The transfer functions for each time block are calculated and their average is used in the intensity calculations[28]. The transfer functions thus become,

$$H_{ij,avg} = \frac{1}{N} \sum_{n=1}^{N} H_{ij,n}. \tag{A.12}$$

Here, N is the total number of time blocks, n is the block index and i, j are the hydrophone indices.

The phase is unwrapped to expand the frequency limit beyond the Nyquist limit. The slope of the phase differences between the hydrophone pairs is estimated using the phases up to 600Hz. The slope is then used to estimate the trend of the unwrapped phases at higher frequencies. The phases are then unwrapped according to,

$$\phi_u = \phi \pm 2\pi n \tag{A.13}$$

such that each phase value is shifted by 2π until it is as close as possible to the estimated trend line. The integer value $n = \{0, \pm 1, \pm 2, \ldots\}$, ϕ is the wrapped phase and ϕ_u is the unwrapped phase [6]. Once the unwrapped phases are obtained, the slope of the trend line is readjusted in order to reduce the error of the fit.

It is then possible to use equation A.3 to calculate the gradient of the phase and in turn, equation A.1 to obtain an estimate of the active intensity. The reactive intensity is directly estimated from the gradient of the pressure amplitude using equation A.2 over an increased frequency range. The directions of both the active and reactive intensities are determined by the direction of the gradients of the phase and the pressure

amplitude, respectively. As the PAGE method directly uses the gradient of the phase, it is possible to use the unwrapped phase gradients to identify the direction of the intensity. The intensity direction,

$$\theta = \arctan\left(\frac{\nabla\phi_y}{\nabla\phi_x}\right) \tag{A.14}$$

Alternatively, as employed in finite difference methods, the direction of the source may be estimated using the phase difference between hydrophones. Figure A.3 depicts a hydrophone pair receiving a signal from a distant source. The path difference between the hydrophones is calculated according to,
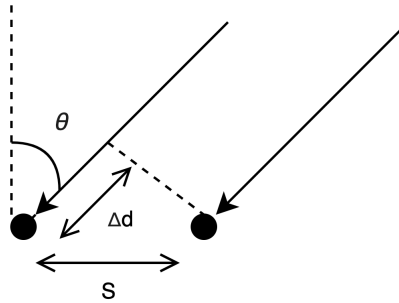
Figure A.3: Hydrophone pair receiving a signal from a distant source.

$$\frac{\delta\phi}{f} = 2\pi\frac{\Delta d}{c} \tag{A.15}$$

where the left hand side of equation A.15 corresponds to the slope of the phase differences trend line and Δd is the path difference between the hydrophones. Once the path difference is determined, the direction of the source θ is calculated as,

$$\theta = \arccos\left(\frac{\Delta d}{S}\right) \tag{A.16}$$

where S is the separation distance between the hydrophones. The direction is calculated for multiple hydrophone pairs in order to confirm consistency. In the following section, results obtained from the orthogonal array are presented for a time period where seismic shots are heard.

A.2.2 Results

The two hydrophone arrays were deployed on the eastern edge of Grand Banks in Newfoundland and Labrador. The orthogonal array was deployed from September 9th to October 18th during which a seismic

80

survey passed by this site. The hydrophone array was attached to an acoustic mooring deployed at a depth of 110 m. Marine mammals including fin whales and humpback whales are known to visit this area [14]. For further details, a soundscape characterization of this area has previously been presented [14].

To begin, a cross spectrum is formed using equation A.11 and the resulting phase differences are shown in figure A.4. A 2 second average over a 30 second period is used to reduce the noise in the phases. Phase wrapping is easily noticed and the phases obtained for hydrophone pairs H_{23}, H_{24} and H_{34} are the least noisy.
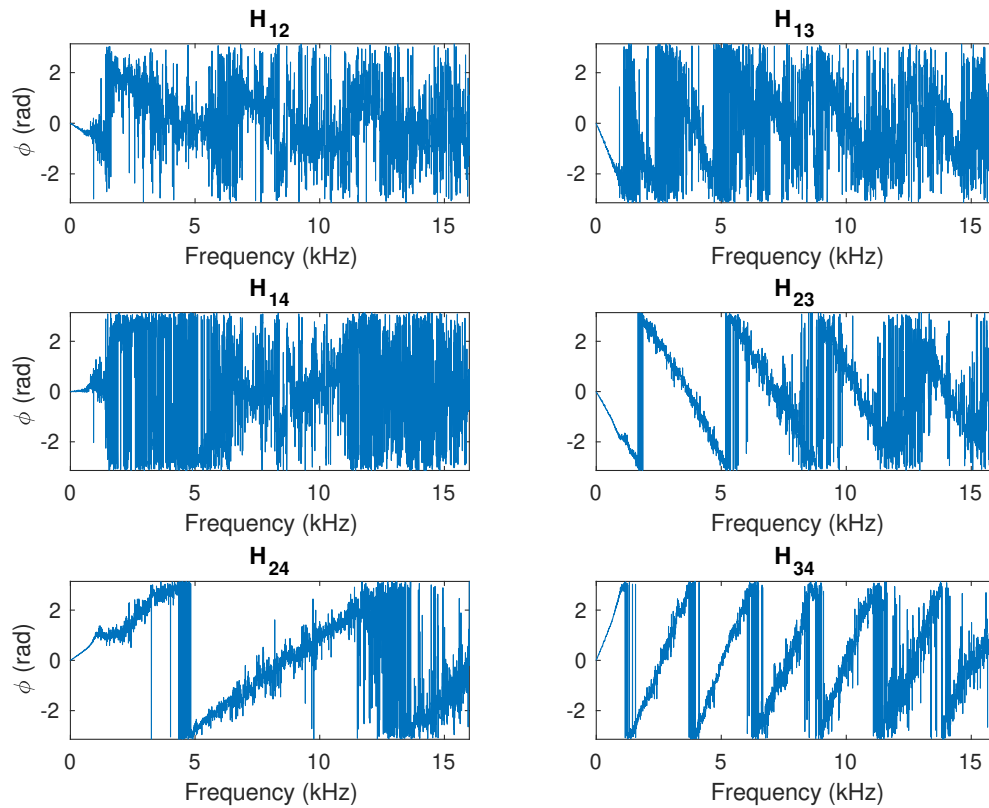
Figure A.4: Phase differences between hydrophone pairs. Phase difference between hydrophones i and j corresponds to H_{ij}. The result shown is for a 2 second average over a 30 second period.

Equation A.5 is used to form $\delta\phi$ which is then used in equation A.3 along with the pairwise hydrophone separation vector to calculate the gradient of the phase, $\nabla\phi$. The resulting $\delta\phi$ and $\nabla\phi$ are shown in figure A.5 as a function of frequency. Up to the Nyquist limit, these are seen to be linear as no phase wrapping occurs. Similarly for the pressure amplitude, equations A.6 and A.7 are used to obtain the result shown in figure A.6. Peaks for both δP and ∇P occur at lower frequencies and are expected below 100 Hz in the case of seismic survey noise.
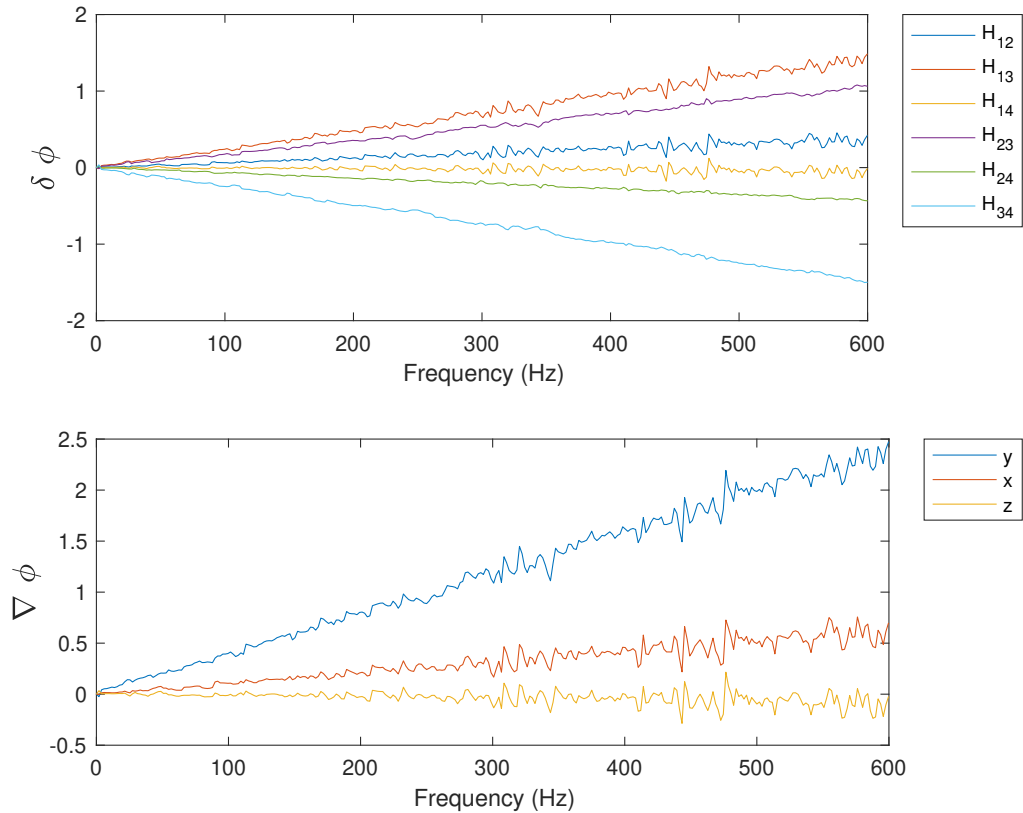
Figure A.5: Pairwise transfer functions, $\delta\phi$ and gradient of the phase as a function of frequency. Transfer function for hydrophone pair i and j corresponds to H_{ij}. Phase gradient components are labelled in the legend.
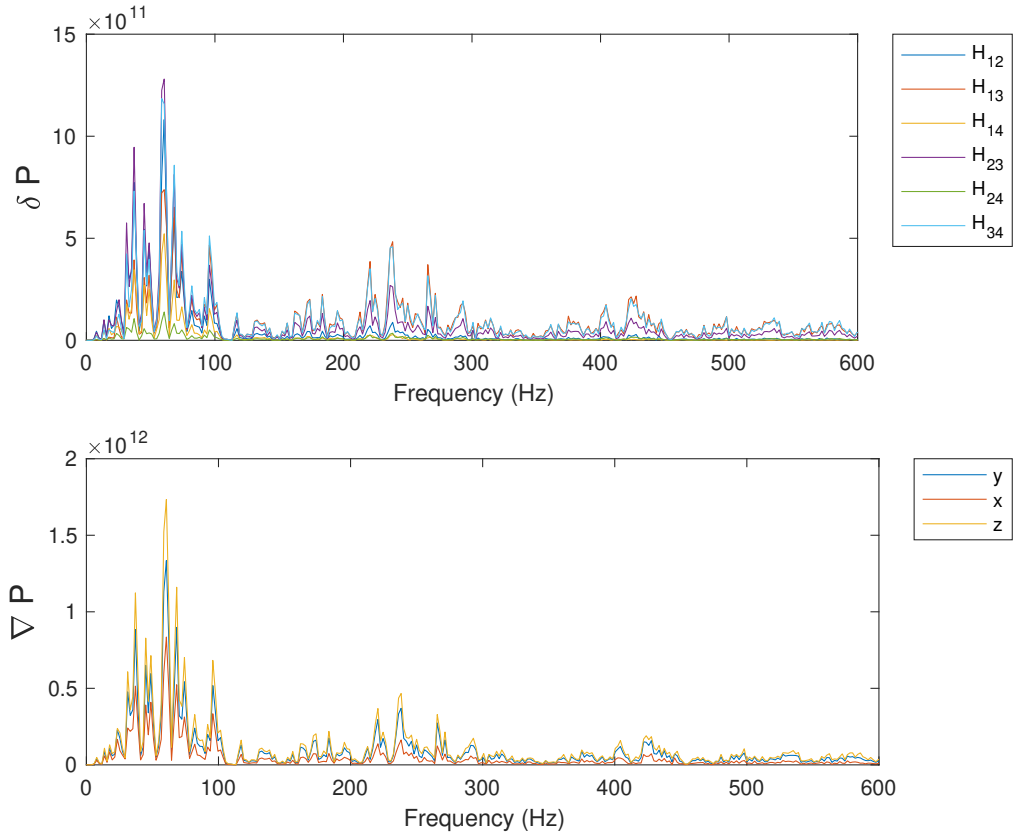
Figure A.6: Pairwise difference between measured pressure amplitudes, δP and the pressure amplitude gradient as a function of frequency. Pressure difference between hydrophones i and j corresponds to H_{ij}. Gradient components are labelled in the legend.

The active and reactive intensities are then calculated with equations A.1 and A.2 using the estimates of $\nabla\phi$ and ∇P, respectively. The pressure at the center of the array is determined by equation A.8 or A.9 according to the array geometry. The resulting intensities are shown in figure A.7 with the active intensity in red and the reactive intensity in black. The intensity is shown as a function of frequency up to just below the Nyquist frequency of 616 Hz.
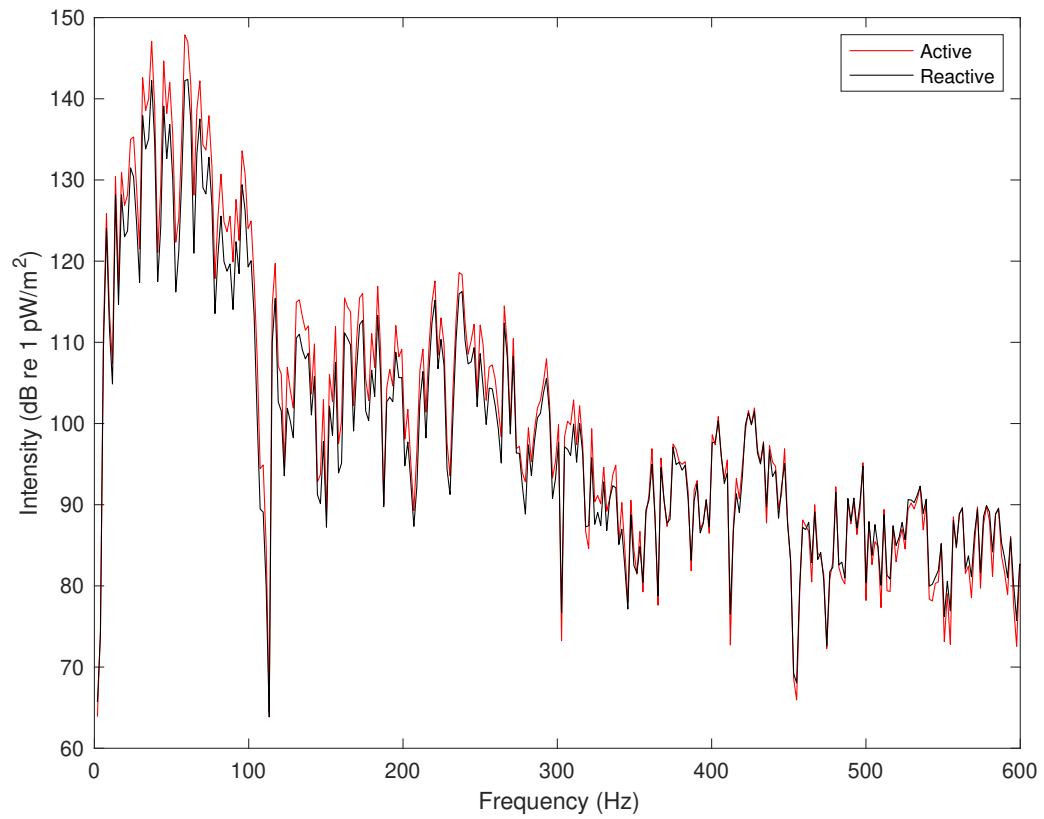
Figure A.7: Active and reactive intensities shown in red and black, respectively. Intensities are shown before phase unwrapping and below the Nyquist limit.

In order to unwrap the phases past the Nyquist limit, the phases as a function of frequency below this limit were fit to a linear trend. Figure A.8 presents the best fit line in red as well as the phases below 600 Hz in black. Each sub-figure is labelled with the corresponding hydrophone pair and the root mean square error (RMSE) of the trend line.
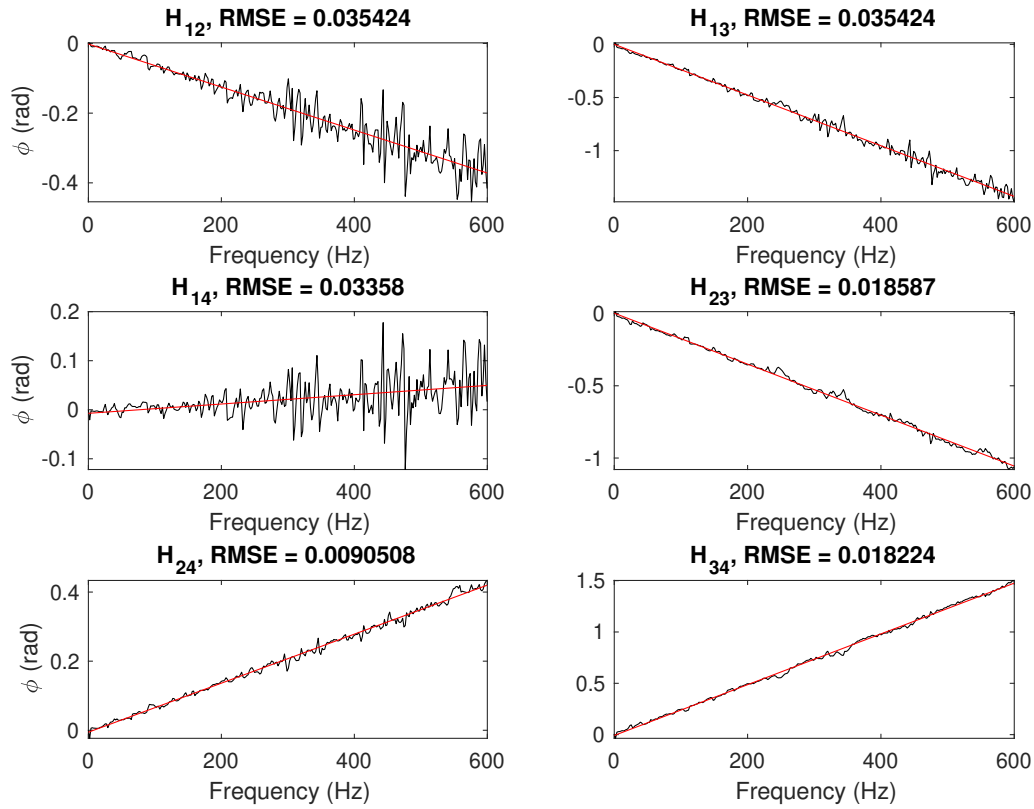
Figure A.8: Phase as a function of frequency up to 600Hz. Red line represents the linear fit used for phase unwrapping. Black line represents unwrapped phases. Hydrophone pairs H_{23}, H_{24} and H_{34} are the least noisy and have small RMSE values.

The phases are then unwrapped according to equation A.13 around the trend line. The result is presented in figure A.9 with the trend line in red and the unwrapped phases in black. The RMSE of the best fit line as well the corresponding hydrophone pair is labelled in each sub-figure.
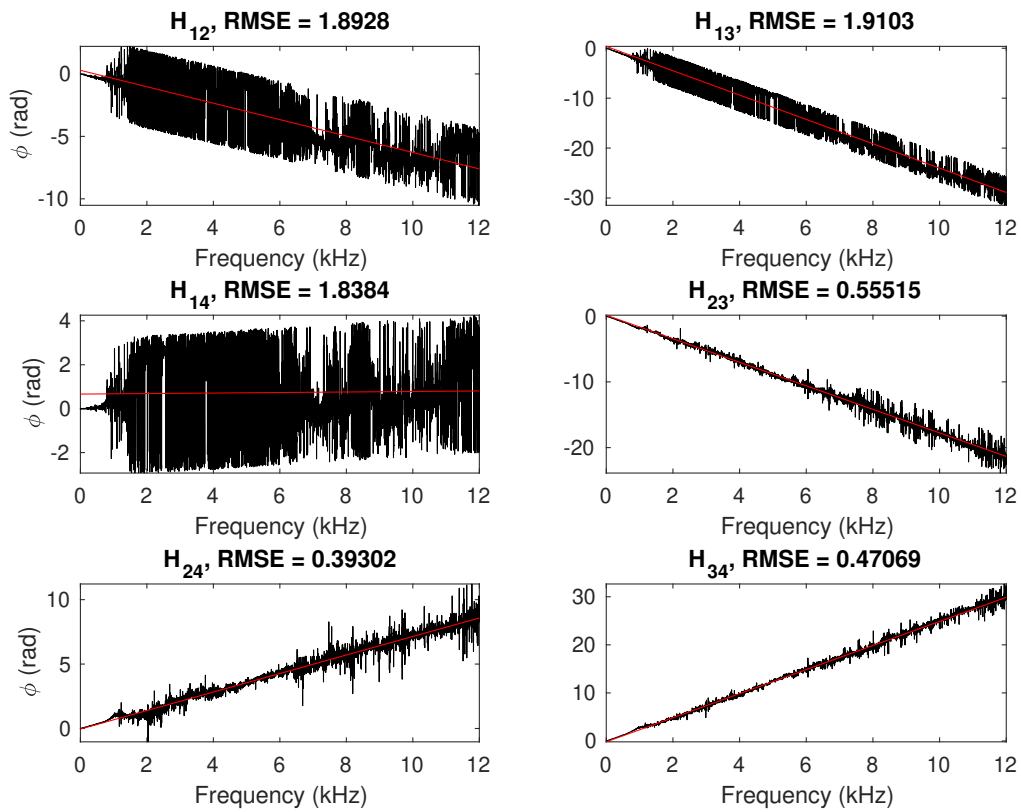
Figure A.9: Unwrapped phases in black, based on trend line shown in red. Trend line has been readjusted after unwrapping to reduce the RMSE. Hydrophone pairs H_{23}, H_{24} and H_{34} correspond to the smallest RMSE values.

The unwrapped phases are then used to estimate the intensity past the Nyquist limit. Figure A.10 presents the intensity calculated using the wrapped and unwrapped phases in red and black, respectively. The lower panel shows the residuals between the two values. As the frequency increases, the residuals tend to increase as the intensity values become noisier.
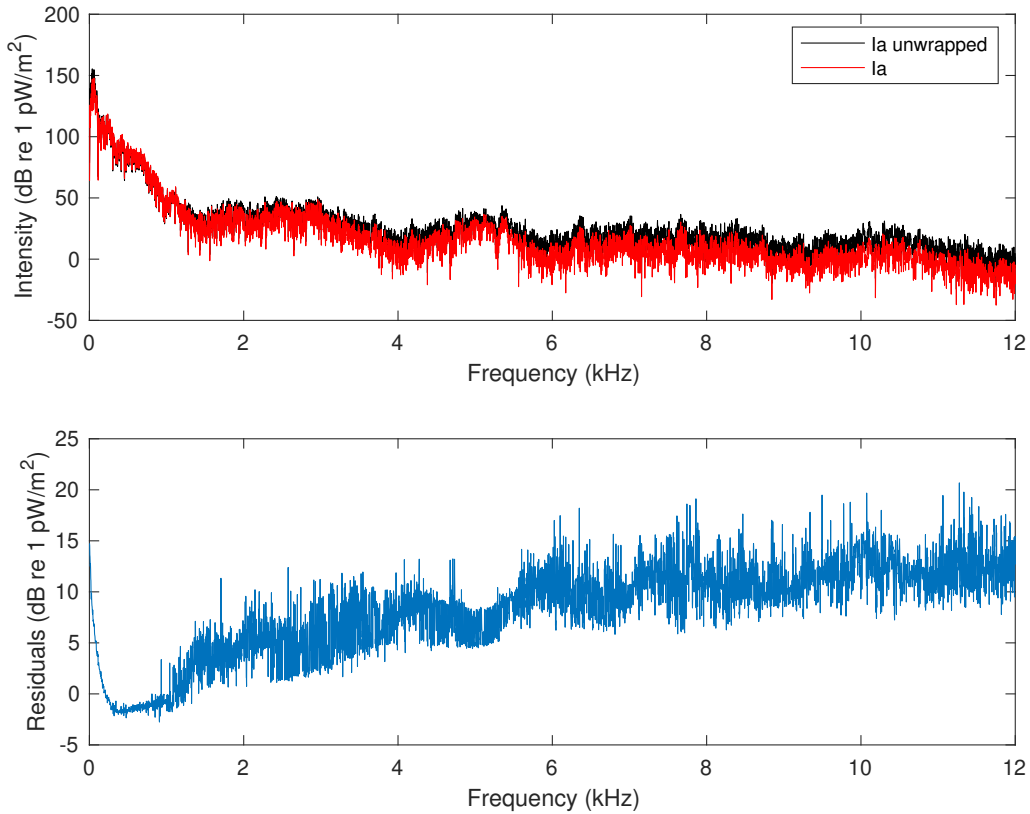
Figure A.10: Active intensity calculated using wrapped and unwrapped phases shown in black and red, respectively. Residuals of the values shown in the lower panel.

First, the direction of the source is calculated as commonly done in finite difference methods for comparison with the PAGE phase gradient method. The direction of the source is determined using the three hydrophone pairs in the x-y plane, H_{12}, H_{13} and H_{23}. The direction is estimated by equations A.15 and A.16. The resulting angles for the 30 second example data segment at 15:28 on 2019-09-12 are shown in table A.1 along with the 95% confidence interval. The angles are measured from the line between hydrophones 1 and 2 which corresponds to the y-axis.

Hydrophone pair	angle (degrees)	upper interval (degrees)	lower interval (degrees)
H_{12}	194.01	194.54	193.48
H_{13}	159.54	161.15	158.04
H_{23}	164.32	164.53	164.09

Table A.1: Angle in degrees corresponding to the intensity direction at 15:28 on 2019-09-12. The direction is estimated using the phase differences and geometry for the three hydrophone pairs in the x-y plane is shown. Upper and lower intervals correspond to 95% confidence interval.

The intensity direction, or the direction of propagation, is also determined by equation A.14 using the calculated phase gradients. The direction analysis process can be repeated with successive data segments. We have chosen 30 second time intervals and an example of dominant signal direction for the 14 hour period on 2017-09-12, during which a seismic survey was conducted. The direction is estimated every hour and is shown in figure A.11. The direction, as calculated in table A.1 is also presented in figure A.11 for the two least noisy hydrophone pairs. For comparison, the average intensity up to 12 kHz is presented for the same time interval. The average intensity reaches a maximum of approximately db re 1 pW/m^2 dB and a minimum of nearly -30 db re 1 pW/m^2. The clearest seismic shot can be heard at 15:28 and corresponds to the maximum average intensity. In the two hours prior and several hours after the maximum intensity, distant seismic shots are heard. As the accumulated time past the maximum increases, the shots become increasingly faint. The intensity direction ranges from around 20 degrees to more than 150 degrees.
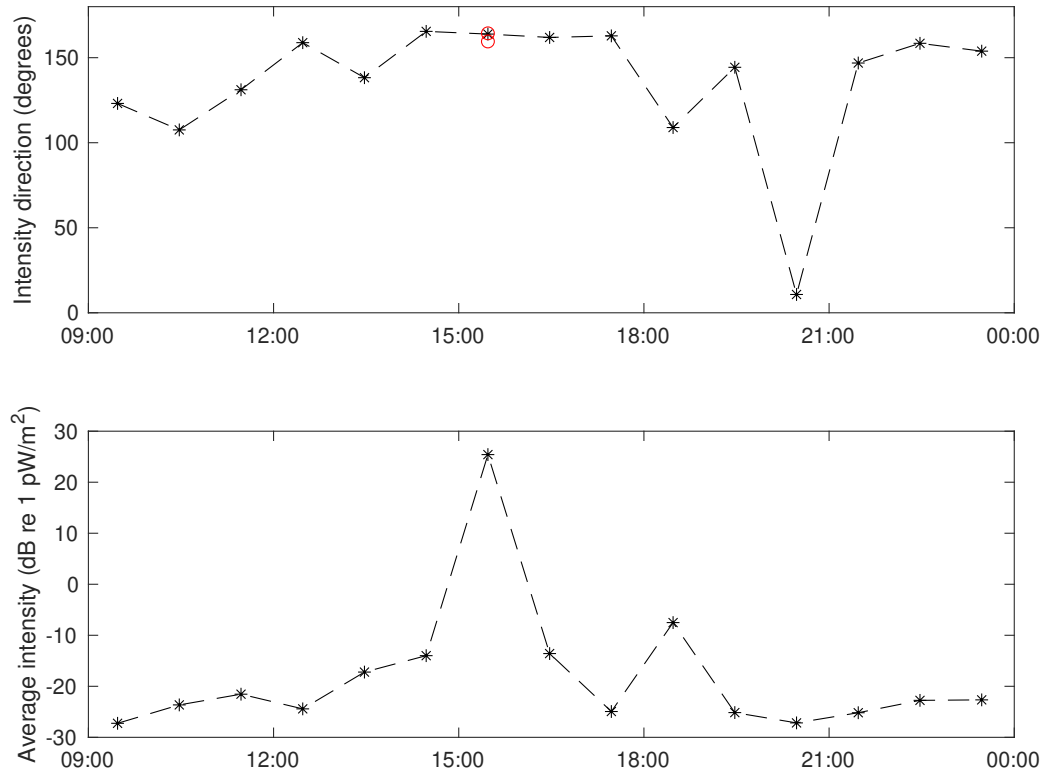
Figure A.11: Intensity direction in degrees measured every hour over a 14 hour period presented in upper panel. Average intensity magnitude shown in lower panel. Time corresponds to 2017-09-12. Red circles present direction as calculated in table A.1 for hydrophone pairs 1-3 and 2-3.

A.2.3 Discussion

The PAGE method starts by evaluating the transfer functions between the hydrophone pairs, shown in figure A.4. Ensemble averaging is used to reduce the noise in the phases where the average interval can be adapted to the source of interest. Sources of interest may include seismic shots, animal calls or other background noise. In order to observe clear phase transfer functions and phase wrapping a distinct noise source is needed. Ensemble averaging reduces the noise in the transfer functions when a dominant and directional source is present which can then allow for the phases to be unwrapped to higher frequencies. The noise will set an upper frequency limit to when the intensity can accurately be estimated. Additionally, phase unwrapping is limited to continuous phase functions and thus a broadband source is required [28]. The broadband requirement for the PAGE processing suggests that it may not be suitable for narrow band sources such as animal calls.

An advantage of the PAGE method is that phases can be unwrapped past the Nyquist limit giving an accurate estimate of the phase gradient and in turn, the acoustic intensity can be obtained at higher frequencies. In this report, phase unwrapping is based on a trend line calculated based on the phase function below $600Hz$. An example of phase unwrapping is shown in figure A.8, where RMSE values range from approximately 0.035 to less than 0.01. Once the frequency is extended past the Nyquist limit and the phases are unwrapped around the trend line, the RMSE increases. As can be expected, the noise in the phase values increases with frequency. Various methods for phase unwrapping have been presented, one of which is a coherence based approach [6]. The coherence based method may provide improved phase values at higher frequencies.

The trend line is then used to calculate the gradient of the phase and the acoustic intensity. Figure A.7 presents a comparison of the intensity calculated using the unwrapped phases as well as the initial wrapped phases. The residuals increase with frequency and are seen to be more stable at lower frequencies. When the phases are not unwrapped, the PAGE method breaks down past the Nyquist limit. Thus, more accurate intensity results are obtained when the unwrapped phases are used.

In the present study, hydrophones 1 and 2 correspond to a noisy pair which leads to the possibility that the resulting source direction from this pair will be less accurate. The results for the estimate of the source direction, presented in table A.1 agree with this expectation. The angles estimated using hydrophone pair 1 and 3 as well as 2 and 3 are within 5 degrees of each other. It is also possible to note that the 95% confidence interval is largest in hydrophone pair 1 and 3 and smallest in hydrophone pair 2 and 3. This result is consistent with the PAGE result presented in figure A.11 at 15:28. The result could be improved

by using the least noisy hydrophone pairs to estimate the direction of the source.

The intensity direction presented in figure A.11 ranges from around 20 degrees to more than 150 degrees in a 14 hour period, during which a seismic survey was conducted. The average intensity reaches a maximum of approximately 25 db re 1 pW/m^2 and a minimum of nearly -30 db re 1 pW/m^2. The clearest seismic shot can be heard at 15:28 and corresponds to the maximum average intensity. In the two hours prior and several hours after the maximum intensity, distant seismic shots are heard. The intensity direction remains fairly stable when the seismic shots are clear. As the shots become increasingly faint, the intensity direction shows larger variation, decreasing from above 150 degrees to around 100 degrees. Distant shots can be heard every hour after 15:28 except at 20:28, which may be the cause of the large direction change at that time. No distinct noise source is heard at 20:28 and may cause the observed shift in intensity direction to approximately 20 degrees.

The PAGE method was applied in an oceanographic context. Intensity estimates can be calculated past the Nyquist limit which can allow hydrophones to be spaced further apart. As a result, improved low frequency estimates can be obtained which can be important for oceanographic applications.

References

[1] K. Angadi, " Natural variations in underwater noise levels in the Eastern Grand Banks, Newfoundland," Master of Science thesis, Memorial University of Newfoundland (2019)

[2] E. M. Arase and T. Arase, "Ambient sea noise in the deep and shallow ocean," J. Acoust. Soc. Am. 42, 73 (1967)

[3] D. R. Barclay, and M. J. Buckingham, "Depth dependence of wind-driven, broadband ambient noise in the Philippine Sea," J. Acoust. Soc. Am. 133, 62 (2013)

[4] B. B. Ma, J. A. Nystuen and R. Lien, "Prediction of underwater sound levels from rain and wind," J. Acoust. Soc. Am. 117, 3555 (2005)

[5] B. B. Ma and J. A. Nystuen, "Passive acoustic detection and measurement of rainfall at sea," Journal of Atmospheric and Oceanic Technology. 22, 8 (2005)

[6] M. R. Cook, K. L. Gee, S. D. Sommerfeldt, and T. B. Neilsen, "Coherence-based phase unwrapping for broadband acoustic signals," Proc. Mtgs. Acoust. 30, 055005 (2017)

[7] D. Coté, K. Heggland, S. Roul, G. Robertson, D. Fifield, V. Wareham, E. Colbourne, G. Maillet, B. Devine, L. Pilgrim, C. Pretty, N. Le Corre, J.W. Lawson, C. Fuentes-Yaco and A. Mercier, "Overview of the biophysical and ecological components of the Labrador Sea Frontier Area," DFO Can. Sci. Advis. Sec. Res. Doc. 2018/067. v + 59 p. (2019)

[8] I. Dyer, "Acoustic Noise," Encyclopedia of Ocean Sciences (Second Edition), Academic Press, 52-61 (2001)

[9] W. J. Emery and R. E. Thomson, "Data analysis Methods in Physical Oceanography," Elsevier Science, pp. 371-567 (2001)

[10] R. E. Francois and G.R. Garrison, "Sound absorption based on ocean measurements: Part I: Pure water and magnesium sulfate contributions," J. Acoust. Soc. Am. 72, 896 (1982)

[11] K. L. Gee, T. B. Neilsen, S. D. Sommerfeldt, M. Akamine, and K. Okamoto, " Experimental validation of acoustic intensity bandwidth extension by phase unwrapping," J. Acoust. Soc. Am. 141, EL357 (2017)

[12] G. Godin, "The analysis of tides and currents," Parker, B.B (Ed.), Tidal Hydrodynamics. Wiley, New York, pp. 675–709. (1991)

[13] J. S. Lawrence, K. L. Gee, T. B. Neilsen, and S. D. Sommerfeldt, "Highly directional pressure sensing using the phase gradient," J. Acoust. Soc. Am. 144, EL346 (2018)

[14] B. Martin, E. Maxner, M. Wood, L. Horwich and K. Kowarski, "Soundscape Characterization and Marine Mammal Presence on the Eastern Grand Banks, NF: September to October 2016." Document 01305, Version 1.0. Technical report by JASCO Applied Sciences for DFO Newfoundland (2017)

[15] M. F. McKenna, D. Ross and S. M. Wiggins et al, "Underwater radiated noise from modern commercial ships," J. Acoust. Soc. Am. 131, 92 (2012)

[16] H. Medwin, C. S. Clay, "Fundamentals of acoustical oceanography", Academic Press, (1998)

[17] H. Medwin, J. A. Nystuen, P. W. Jacobus, L. H. Ostwald, and D. E. Snyder, "The anatomy of underwater rain noise," J. Acoust. Soc. Am. 92, 1613 (1992)

[18] G. B. Morris, "Depth dependence of ambient noise in the northeastern Pacific Ocean," J. Acoust. Soc. Am. 64, 581 (1978)

[19] National Research Council (U.S.), "Ocean Noise and Marine Mammals," National Academies Press (2003)

[20] J. A. Nystuen, "Validation of acoustic measurements of wind and rain using expandable ambient noise sensor (ans) drifters, an/wsq-6 (xan-2)," Technical report, Washington univ Seattle applied physics lab (1997)

[21] J. A. Nystuen and D. M. Farmer, "The influence of wind on the underwater sound generated by light rain," J. Acoust. Soc. Am. 82, 270 (1987)

[22] J. A. Nystuen, C. C. McGlothin and M. S. Cook, "The underwater sound generated by heavy rain," J. Acoust. Soc. Am. 93, 3169 (1993)

[23] R. Pawlowicz, B. Beardsley and S. Lentz, "Classical tidal harmonic analysis including error estimates in MATLAB using T TIDE," Computers Geosciences 28, 929–937 (2002)

[24] A. J. Perrone, "Ambient noise spectrum levels as a function of water depth," J. Acoust. Soc. Am. 48, 362 (1970)

[25] A. Prosperetti, "Bubble-related ambient noise in the ocean," J. Acoust. Soc. Am. 84, 1042 (1988)

[26] P. Stoica and R. Moses, "Spectral Analysis of Signals," Prentice Hall, pp. 4-52 (2005)

[27] Teledyne RD instruments, "Acoustic Doppler Current Profiler, Principles of Operation, A Practical Primer," (2011)

[28] D. C. Thomas, B. Y. Christensen, and K. L. Gee, "Phase and amplitude gradient method for the estimation of acoustic vector quantities," J. Acoust. Soc. Am. 137, 3366 (2015)

[29] D. K. Torrie, E. B. Whiting, K. L. Gee, T. B. Neilsen, and S. D. Sommerfeldt, "Initial laboratory experiments to validate a phase and amplitude gradient estimator method for the calculation of acoustic intensity," Proc. Mtgs. Acoust. 23, 030005 (2015)

[30] S. Vagle, W. G. Large and D. M. Farmer, "An evaluation of the WOTAN technique of inferring oceanic winds from underwater ambient sound," J. Atmos. Ocean. Technol. 7, 576–595 (1990)

[31] G. M. Wenz, "Acoustic ambient noise in the ocean: spectra and sources," J. Acoust. Soc. Am. 34, 12 (1962)

[32] C. P. Wiederhold, K. L. Gee, J. D. Blotter, and S. D. Sommerfeldt, "Comparison of methods for processing acoustic intensity from orthogonal multimicrophone probes," J. Acoust. Soc. Am. 131, 2841 (2012)

[33] C. P. Wiederhold, K. L. Gee, J. D. Blotter, S. D. Sommerfeldt, and J. H. Giraud, "Comparison of multimicrophone probe design and processing methods in measuring acoustic intensity," J. Acoust. Soc. Am. 135, 2797 (2014)